



HAL
open science

Adsorption on interstellar analog surfaces : from atoms to organic molecules

Mikhail Doronin

► **To cite this version:**

Mikhail Doronin. Adsorption on interstellar analog surfaces : from atoms to organic molecules. Chemical Physics [physics.chem-ph]. Université Pierre et Marie Curie - Paris VI, 2015. English. NNT : 2015PA066254 . tel-01238850

HAL Id: tel-01238850

<https://theses.hal.science/tel-01238850>

Submitted on 7 Dec 2015

HAL is a multi-disciplinary open access archive for the deposit and dissemination of scientific research documents, whether they are published or not. The documents may come from teaching and research institutions in France or abroad, or from public or private research centers.

L'archive ouverte pluridisciplinaire **HAL**, est destinée au dépôt et à la diffusion de documents scientifiques de niveau recherche, publiés ou non, émanant des établissements d'enseignement et de recherche français ou étrangers, des laboratoires publics ou privés.

**THÈSE DE DOCTORAT
DE L'UNIVERSITÉ PIERRE ET MARIE CURIE**

Spécialité : Physique

École doctorale : "Physique en Île-de-France"

réalisée

au Laboratoire d'Études du Rayonnement et de la Matière en
Astrophysique et Atmosphères
et Laboratoire de Chimie Théorique

présentée par

Mikhail V. DORONIN

pour obtenir le grade de :

DOCTEUR DE L'UNIVERSITÉ PIERRE ET MARIE CURIE

Sujet de la thèse :

**Adsorption on Interstellar Analog Surfaces: from Atoms to
Organic Molecules**

soutenue le 28 Septembre 2015

devant le jury composé de :

M.	Josep-Manel Ricart Pla	Rapporteur
M.	Patrice Theulé	Rapporteur
M.	Christophe Petit	Examineur
M.	Lionel Amiaud	Examineur
M ^{me}	Valentine Wakelam	Examineur
M.	Jean-Hugues Fillion	Directeur de thèse
M.	Alexis Markovits	Directeur de thèse

Contents

1	Introduction	1
1.1	Astrophysical Context	1
1.2	Physisorption versus Chemisorption	2
1.2.1	Physisorption	3
1.2.2	Chemisorption	4
1.3	Strategies for a reliable database	5
1.4	Case Studies	6
I	Employed Methods	13
2	Experimental approach	15
2.1	Experimental setup	15
2.1.1	General description and characteristics	15
2.1.2	Cryogenics and temperature control	17
2.1.3	Gas phase species detection - quadrupole mass spectrometer (QMS)	21
2.1.4	Ultra-High Vacuum	25
2.1.5	Sample species vapour preparation module	26
2.1.6	Adsorbate film thickness	27
2.1.7	Other experimental issues	30
2.2	Temperature Programmed Desorption	32
2.2.1	Desorption kinetics order	33
2.2.2	Surface coverage calibration	34
2.2.3	Desorption data modeling and analysis	35
2.3	Desorption data analysis: case study of CH_3OH	37
2.3.1	Coverage calibration	37
2.3.2	Adsorption energy in multilayer regime	38
2.3.3	Adsorption energy in sub-monolayer regime	39
2.3.4	Summary	45
3	Theoretical approach	49
3.1	First principles approach	49
3.1.1	General introduction on DFT	49
3.1.2	Exchange-correlation functionals	51

3.1.3	Van der Waals interactions	51
3.2	Cluster versus periodic approaches	52
3.3	Determining adsorption energetics	52
3.3.1	Periodic system	53
3.3.2	Bulk geometry optimization	53
3.3.3	Surface modelling	53
3.3.4	Adsorption sites	55
3.3.5	Example: CH_3OH adsorption on graphite	55
3.4	Topological analysis	63
3.4.1	Electronic Localization Function (ELF)	63
3.4.2	Integrated properties	64
3.4.3	Example of ELF topology: methanol	64
II	Systems studied	69
4	Adsorption and Trapping of Noble Gases by Water Ices	71
4.1	Study context	71
4.1.1	Planetology issue	71
4.1.2	Update review	72
4.1.3	Trapping by ices	72
4.2	Experimental approach	74
4.2.1	Laboratory ice samples	74
4.2.2	Adsorption on water ices	76
4.2.3	Inclusion in water ices	83
4.3	Theoretical approach	85
4.3.1	Modeling the ice surface	85
4.3.2	Adsorption sites	87
4.3.3	Convergence against cell dimensions	89
4.3.4	Adsorption	91
4.3.5	Substitution	92
4.3.6	Inclusion	94
4.4	Comparisons and conclusions	94
5	Adsorption of CH_3CN vs CH_3NC at interstellar grain surfaces	99
5.1	Study context	99
5.2	Experimental approach	100
5.2.1	Pure thick ices of CH_3CN and CH_3NC	100
5.2.2	Submonolayer of CH_3CN and CH_3NC on model surfaces	104
5.3	Theoretical approach to adsorption energies	110
5.3.1	Adsorption energies on highly oriented pyrolytic graphite	110
5.3.2	Adsorption energies on silica	112
5.3.3	Adsorption energies on crystalline water ice	113
5.4	Discussion and final remarks	114

6 Ionization and trapping of sodium in cometary ices	121
6.1 Study context	121
6.2 Paper	122
6.3 Conclusion	128
7 Conclusion and Perspectives	131
Appendices	137
Appendix A	
PID zones table	139
Appendix B	
TPD model function	140
Appendix C	
VASP parameters	142

Chapter 1

Introduction

1.1 Astrophysical Context

To date, almost 200 different molecular species have been detected in various regions of the interstellar space [1] and in various objects of the solar system. These molecules range from elementary species (H_2 , CO , N_2 , CO_2 , H_2CO) to larger organic species of up to 13 atoms including carbon chains, organic and even organometallic compounds that could eventually provide initial molecular stones for the formation of “pre-biotic” molecules. With the advent of new ground-based and space telescopes of high sensitivity in the visible, infrared and submillimeter wavelengths, the richness and diversity of molecular compounds discovered in various regions of the interstellar medium is increasing dramatically. Especially, the observations with the ALMA and, in the near future, the NOEMA radio-telescopes are beginning to revolutionize the field by providing ultra-high spatial resolution, in particular within star-forming regions, promising a tremendous forthcoming insight into this fascinating but still largely unknown interstellar chemical world. The rich organic inventory of space reflects the multitude of chemical processes involved, that on the one hand, build up complex organic molecules (COMs) from simpler entities, and on the other hand, break down large molecules, injected by stars, into smaller fragments [2].

Over the last 30 years, significant progress in the understanding of formation, evolution and destruction of molecules in molecular clouds has revealed the crucial role of dust grains which act as catalytic sites for molecule formation and explain the presence of species that pure gas phase chemical networks failed to predict [3]. Gas-surface interactions are now considered as playing a major role in the monitoring of molecular diversity in space. In the interstellar medium and in planetary bodies as well, the condensation and desorption of molecules from the surfaces play an essential role in the physics and chemistry of these objects, driving the different stages of their evolution [2].

Interstellar dust grains are submicron-sized particles made of silicates and/or carbonaceous cores. In cold regions, such as dense molecular clouds, pre-stellar cores and inner part of proto-planetary disks, grains are covered by an icy mantle, mainly composed of water, but also containing many other compounds. The main ice components (CO_2 , CO , CH_3OH , CH_4) are detected in the solid phase by infrared spec-

troscopy [4, 5]. These ices can be continuously processed by the impact of cosmic rays, UV-X photochemistry and thermal diffusion, providing a rich molecular reservoir and a source of larger species which, after being released into the gas phase, are more favorably detected by sub-millimeter rotational transitions of molecules. It should be noted here that this observation technique is blind to the molecules that remain on the grain.

From a chemical point of view, interstellar grains provide a surface on which atoms and molecules can accrete, meet and react. They also play the role of a third body in the reactions which efficiently dissipates the excess energy released in the reactions. It is the case for the formation of molecular hydrogen, the most abundant molecule in space, which can only be thermalized by interaction with the surface of dust grains. As initially suggested by Tielens and Hagen [6], it is now established that many other species (such as H_2O , CO_2 or CH_3OH) have efficient grain-surface chemical formation routes.

The mobility and the surface residence time of an adsorbate bound to a surface are related to a fundamental parameter: the binding energy or “adsorption energy”. In case of exothermic reactions, the newly formed molecules on the surface can be eventually ejected promptly into the gas phase after formation. The efficiency of this process is partly determined by the ratio between the energy released by the reaction and the adsorption energy of the molecule just formed. Other non-thermal processes as the sputtering by fast particles in shocks or the desorption induced by cosmic rays and/or by UV-X rays (the so called “photo-desorption” phenomenon), are also critically dependent of the adsorption energy. In other environments such as in hot cores or cometary nuclei, ices are heated and the molecular reservoir is released into the gas-phase by thermal desorption. Again, the adsorption energy is a central parameter to describe the phenomenon.

In summary, the adsorption energies appear to be highly crucial, because their values govern the temperature at which the molecules are condensed on the solid state surface or released into the gas phase, and also (for the smaller species) because they drive the surface mobility and impact the subsequent chemistry. Adsorption energies strongly influence the gas-phase and grain-surface reactions simultaneously. Depending on the physical conditions of the various sources (temperature and densities), the desorption energies are key parameters that can explain (or predict) both the gas phase and condensed phase compositions. In such a context, complex astrochemical networks including the coupling between gas-phase and grain-surface synthesis are under fast development [7–10]. As a consequence, the need for quantitative physical-chemical data becomes more and more important. Today, everyone has to be aware that the transition from elementary molecules towards more complex organic systems could only be solved by developing accurate chemical models supported by relevant laboratory data.

1.2 Physisorption versus Chemisorption

Adsorption energy is governed by the interaction potential between the atoms/molecules adsorbates and the solid surface to which they are bound [11–13]. In the present context, the solid, or substrate, is either the bare grain surface, valid for “warm“ (> 100 K)

environments, or the water-rich icy mantles, valid for colder regions (10-100 K).

1.2.1 Physisorption

The weakest form of adsorption to a solid surface is called physical adsorption, or physisorption. It is characterized by the lack of a strong chemical bond (covalent or ionic) between adsorbate and substrate. The adsorbed molecule is bound to the surface via weak Van der Waals interactions. The attractive forces are due to a combination of dispersion and dipolar forces. Dispersion forces originate from instantaneous fluctuations in electron density, which cause transient dipoles in the molecules. These instantaneous dipole moments interact with the polarizable nearest neighbors on the surface, presenting or not a permanent dipole moment [12]. Forces due to molecules that have permanent dipole moments are usually stronger. In some systems, an hydrogen atom, bound to an electronegative atom, (NH or OH bonds), is close enough to interact with the lone pairs of another electronegative atom (N/O), leading to the formation of what is called an "hydrogen bond". This type of bond is stronger than pure Van der Waals interaction, although weaker than covalent or ionic bonds (see "chemisorption" 1.2.2 below). Generally, adsorption on very low temperature surfaces, such as the ones encountered in the interstellar medium, is largely due to physisorption.

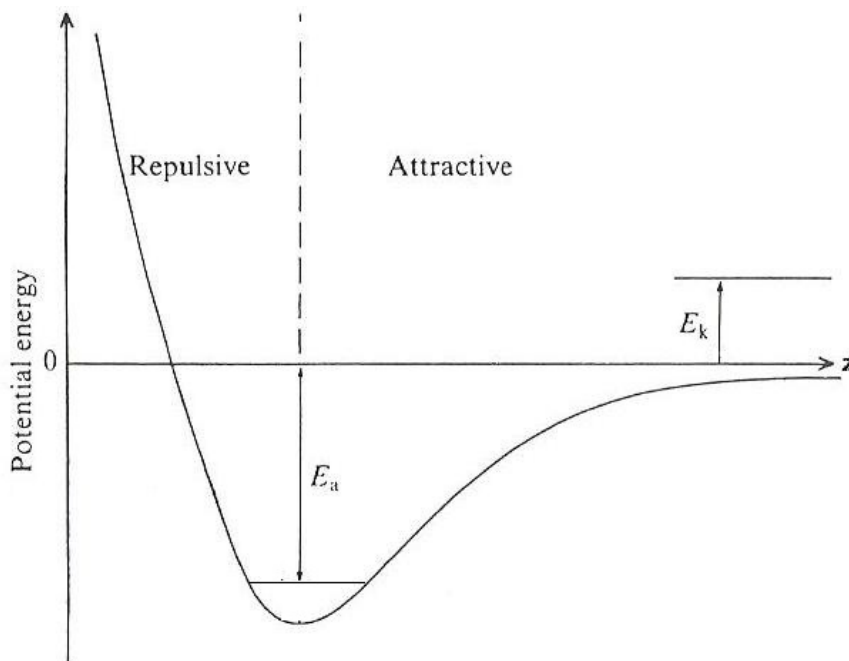


Figure 1.1 – Potential energy of an atom or molecule physisorbed on a planar surface.

As illustrated on Figure 1.1, an incoming atom/molecule, with kinetic energy E_k , that loses enough energy when impinging the surface and exciting phonons in the substrate, can equilibrate in a state in the potential well with the binding or adsorption energy E_a . The atom/molecule is said to be accommodated to the surface. Conversely, in order to leave the surface, the atom/molecule must acquire enough energy to escape

from the depth of the potential well, i.e. E_a . The desorption energy is thus equal to the adsorption energy. In the case of pure Van der Waals-type of interactions, the adsorption energies for physisorbed molecules are typically ranging between 0.01-0.4 eV. In the case of hydrogen-bonds, the adsorption energies are higher and usually found in the 0.4-0.5 eV range. This will generally correspond to adsorption of organic molecular species playing an important role in astrochemistry.

1.2.2 Chemisorption

In some cases, electron sharing occurs between the adsorbed species and the surface. A rather strong bond is thus created with the surface and the atom/molecule is said to be chemisorbed. The bond formed may be ionic or covalent, or a mixture of both. A simple example of the potential energy diagram for chemisorption is shown in Fig. 1.2. Some of the impinging molecules are accommodated by the surface and become weakly bound in a physisorbed state. Then electronic or vibrational processes can occur, which allows the physisorbed molecules to surmount the barrier E_c and be equilibrated in a much deeper well. Chemisorption resulting in the formation of a chemical bond between the adsorbing molecule and the surface is at least one order of magnitude stronger (extending from 0.5 to several eV in extreme cases) than physisorption. This process generally results in a profound modification of the local structure like an insertion in the bonds of the surface. It is termed non-dissociative chemisorption. Adsorption can, alternatively, result into the dissociation of the molecule [13], and is then referred to as dissociative chemisorption.

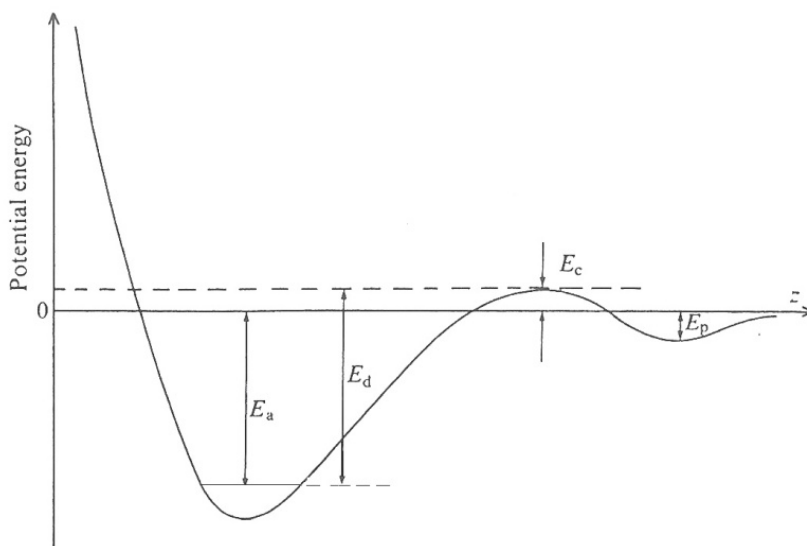


Figure 1.2 – Chemisorption on a planar surface. Adapted from ref [11]

In this work we are concerned only with van der Waals and hydrogen bonding. However, even in this case, we will see that the study of the desorption of atoms and molecules from a grain surface is not as "simple" as it may appear.

1.3 Strategies for a reliable database

The lack of basic laboratory data concerning the interaction of many of these molecules on astrophysical relevant surfaces strongly limits the possibilities of the modeling. The adsorption (desorption) energies on surfaces are eventually known for some of the smaller species but mainly assumed (or derived from non-relevant astrophysical studies) for the larger ones. Fundamental laboratory data (experimental and/or theoretical) are thus urgently needed to help improving our current understanding of this complex coupled gas-surface chemistry.

This thesis is the first step of a larger project whose main objective is to construct a coherent database that will provide fundamental parameters that can be confidently used to quantify a number of gas-surface interaction processes such as desorption, diffusion or trapping of molecules on a dust grain or more generally any kind of interstellar solid. The program is then supposed to be developed around oxygen bearing molecules, nitrogen bearing molecules, large hydrocarbons (PAHs) and finally molecules directly linked to pre-biotic compounds. Aiming at the highest reliability possible, a particular effort had to be done on the experimental side to optimize a methodology for performing and analyzing experiments based on thermal desorption. Altogether and whenever feasible, the theoretical results produced were confronted with the laboratory experiments in conditions as close as possible to the interstellar environment, using well-defined surfaces as prototypes.

Dust grains are thought to be composed of silicates or oxides, surrounded by carbonaceous materials and/or an icy mantle in some circumstances [5]. The precise composition and morphology of interstellar grains, as well as the identification of the constituents of their icy mantles is of course not fully determined and subject to debate. This study deals with different surfaces of various nature and morphology, which could be considered as reasonable interstellar surface analogs: water ice (compact and crystalline) to simulate conditions in cold regions, a graphite surface and a silica monocrystal (chiral quartz) to simulate conditions of warmer carbon/silicate rich regions. The presence and influence of some kind of defects on the surface has also been considered to mimic corrugated carbonaceous solids. Such investigations allow exploring the specificities of these potentially interstellar surfaces, by comparing the behavior of closely related molecules on different surfaces.

The main experimental technique used to study the adsorption/desorption processes were thermal desorption techniques in the 10-200 K temperature range. These techniques were coupled to Infrared spectroscopy in absorption-reflection mode, well suited to probe surface composition. Such diagnostics have been optimized on the recently developed new surface science set-up “Surface Processes and Ices” (SPICES) at LPMAA/LERMA [14, 15]. In particular the recent incorporation of a rotating surface sample holder in the ultra-high vacuum experimental main chamber is well-suited to investigate and compare multiple surfaces under strictly identical conditions. A complete description of the experimental set-up is given in part 2.1 and the principle of the data treatment is explained in parts 2.2 and 2.3 on the example of methanol.

When confronting with laboratory experiments, studying the adsorption/desorption processes can be more complex than expected. Practically, two specific situations arise. At first, one can distinguish the so-called “CO-like” species, related to species with ad-

sorption energies below 0.1 eV. In this case, a single desorption peak appearing at low temperature is observed (typically below 50 K in ultrahigh vacuum conditions) upon thermal heating. That would make the characterization of the desorption energy relatively straightforward. However, because the adsorption energy and, by correlation, the diffusion energies, are very low, these extremely weakly bound species are very mobile, even at very low temperatures (10 K). This is the case, for example, for CO, H₂, O₂ and N₂ or atoms physisorbed on water ice. Those species easily diffuse within the water ice network, being temporally trapped upon heating and giving rise to multiple desorption peaks associated to water ice crystallization and desorption. Another kind of complex situation may occur when the adsorbate-adsorbate interaction energy becomes significant, that is of the same order of magnitude as mutual interactions within the solid substrate. This is typically the case for organic molecules adsorbed on solid water ice, for which molecule-water, molecule-molecule and water-water interactions can be very similar. It leads to thermal desorption signatures that can be difficult to assign, because it becomes difficult to distinguish between the desorption of the adsorbate and the water desorption itself. These situations are encountered and discussed in this thesis. For completeness, one should mention that other classifications can be found depending on the desorption behavior of the molecules in ref. [16, 17].

On the theoretical side, the adsorption energy is usually seen as a local property arising from the electronic interaction between a solid support and the molecules deposited on its surface. The determination of the interaction energy requires the calculation of the energies of the adsorbate molecule, of the pristine surface of the substrate and of the adsorbate-substrate complex, all entities being optimized in isolation.

Two different ways of describing the solid surface can be considered, i.e. the cluster model and the periodic model. Representing a grain as a cluster seems to be a natural approach, but in such a model the surface is that of a molecular aggregate of limited dimension, constrained by the number of molecules participating to the structure. This representation presents several drawbacks. For example, the H₂O clusters, when optimized, present very different surfaces [18] so that there is a complete loss of generality. For larger clusters (over two hundreds molecules), the structure tends to crystalline ice and the calculations becomes rapidly intractable.

Here the theoretical approach has been performed using “state of the art” methods derived from Density Functional Theory (DFT) relying on a periodic description of the solid supports using plane-waves expansions. These methods often referred to as first principle simulations have proved very efficient for both water-ice and carbonaceous materials [15, 19]. The calculations in the frame of the computational chemistry approach were performed with the Vienna Ab initio Simulation Package (VASP) [20, 21]. The theoretical background of all the methods is presented in the chapter 3.

1.4 Case Studies

The research PhD program has been initiated by an important work on optimizing the method for adsorption energies determination, both experimentally and theoretically. Significant experimental hardware and protocol improvements have been realized, and a method has been proposed for extracting dependable quantitative data from thermal desorption experiments. This latter method has been benchmarked using the study of

the methanol adsorption on graphite, a case for which some experimental and theoretical values were available. A complete and critical analysis of the desorption data for different regimes is presented for this precise case in chapter 2.3. In order to ensure the coupling of the experimental/theoretical approaches, a few specific computational tests have also been performed on this example, though another set of basic tests related to theoretical modeling was carried out on atoms (noble gases) for practical reasons.

The other cases presented here can be referred to as systems of interest for the Titan, the MIS and comets, respectively.

The first issue addressed in this thesis, in which adsorption may play a crucial role, is that of the depletion of argon, krypton and xenon observed in Titan atmosphere. The biggest satellite of Saturn is the only moon of the solar system with a really significant atmosphere. A surprising characteristic of its atmosphere is that no other heavy noble gas than argon has been detected by the Gas Chromatograph Mass Spectrometer (GCMS) on board of the Huygens probe when descending towards the surface of Titan in 2005. Moreover the argon which is detected is essentially ^{40}Ar , which is produced by the radiogenic disintegration of potassium 40K, and some primordial ^{36}Ar , very under-abundant compared to the solar value (about 6 orders of magnitude) [22]. The other primordial noble gases, i.e. ^{38}Ar , krypton and xenon, have not been detected by the instrument GCMS, which implies that their molar fractions are less than 10^{-8} (detection limit of Huygens GCMS) in Titan atmosphere. This noble gases deficiency has been extensively studied and multiple scenarios proposed but none of them gives a satisfactory global explanation. These scenarios are related either to the internal properties of Titan and the specific structure of its atmosphere or to the formation conditions of Titan in the primitive nebula [23–30]. Among them, Osegovic and Max suggested that the noble gases could have been stocked in ices under clathrates allomorphs supposed to be present in Titan, and performed some successful exploratory studies with xenon [23]. The hypothesis was then reactivated by Mousis and collaborators for Xe, Kr and Ar [24, 25]. This kind of trapping seems to be possible though its efficiency is still to be proved, but in fine it has to be reminded that the existence of such mechanism relies on the mere relevance of forming clathrates in interstellar conditions, which is still highly controversial. This is why we turn towards the adsorption trapping by other more conventional forms of ices. The mechanism considered here is the adsorption/inclusion by the dominant solid surfaces available in the primitive nebula, i.e. the compact or crystalline icy grain mantles; those grains being the original constituents of Titan, this process should have had an impact on the noble gases abundances, which has yet to be investigated.

The second issue addressed, in which adsorption may also be a determining factor, is that of the relative abundances of isomers observed in the gas phase of the interstellar medium (ISM). Here we focus on the CH_3CN and CH_3NC isomers. These compounds are representatives of the nitrogen bearing molecules. They belong to the family of nitriles R-CN and iso-nitriles R-NC which, together, represent about 20% of the observed species. Not only these molecules are key molecules in the evolution chain towards complexity and emergence of species of astrobiological interest, but the abundance ratios of their isomers have also been widely used to constrain the astrochemical models. The couple HCN/HNC is well known to present gas phase abundances very sensitive to localization [31, 32], contrary to $\text{CH}_3\text{CN}/\text{CH}_3\text{NC}$ whose abundance ratio

is very steady [33, 34]. Considering that radio astronomy technique cannot detect the molecules depleted on surfaces, that is molecules whose rotation is inhibited, it seems compulsory to take into account the adsorption factor in the determination of abundances. As the environment obviously plays a decisive role, we chose to study three different surfaces likely to figure reasonable analogs of interstellar surfaces, with the purpose of covering the panel of surfaces supposedly available in the ISM: water ices, graphite and silica.

The third issue addressed, in which the interaction between an adsorbate and a solid may be critical, is that of the presence of a neutral sodium tail in some comets that are notably composed of water ice accreted onto a refractory nucleus.

Comets are thought to be among the most pristine material in the solar system. Their compositions represent the end point of processing that began in the parent molecular cloud core and continued through the collapse of that core to form the proto-sun and the solar nebula, with the final stages during the evolution of the solar nebula itself as the cometary bodies were accreting. Disentangling the effects of the various epochs on the final composition of a comet is complicated. But learning about the physical and chemical conditions under which comets formed can teach us a lot about the types of dynamical processing that shaped the solar system we see today. This is the objective of the Rosetta mission, which actually boosts all studies about comets.

The observation of comet C/199501 Hale-Bopp in spring 1997 led to the discovery of a new tail connected with the sodium D line emission [35, 36]. Later on, several observations of this phenomenon were recorded in other comets [37, 38]. It means that we are in presence of a neutral sodium gas tail totally different from the usual ion and dust tails, and whose associated source is unclear. Several suggestions have been advanced to rationalize the phenomenon, all physical reasons and unsatisfactory. The shaping of a third type of tail by radiation pressure due to resonance scattering of sodium atoms [35, 38], the photo-sputtering and/or ion sputtering of nonvolatile dust grains [37], or the collisions between the cometary dust and very small grains [39] were considered.

In this thesis, the scenario presented is completely different since it is entirely based upon chemical grounds. It is shown that the Na^+ ions washed out of the refractory material at the epoch of the hydration phase of the comet nucleus, are progressively losing their positive charge to evolve into neutral species during the re-formation of the cometary ices. The chemical path of sodium ends with a neutral atom adsorbed at the surface and finally released from the sublimating cometary ice, largely contributing to a pure neutral sodium tail.

References

- [1] Holger S.P. Müller et al. *Molecules in Space*. www.astro.uni-koeln.de/cdms/molecules, 2015.
- [2] A. G. G. M. Tielens. “The molecular universe”. In: *Reviews of Modern Physics* 85.3 (2013), pp. 1021–1081.
- [3] Daren J. Burke and Wendy A. Brown. “Ice in space: surface science investigations of the thermal desorption of model interstellar ices on dust grain analogue surfaces”. en. In: *Physical Chemistry Chemical Physics* 12.23 (June 2010), pp. 5947–5969.
- [4] Emmanuel Dartois. “The Ice Survey Opportunity of ISO”. en. In: *Space Science Reviews* 119.1-4 (Aug. 2005), pp. 293–310.
- [5] A.C. Adwin Boogert, Perry A. Gerakines, and Douglas C.B. Whittet. “Observations of the Icy Universe”. In: *Annual Review of Astronomy and Astrophysics* 53.1 (2015), null.
- [6] A. G. G. M. Tielens and W. Hagen. “Model calculations of the molecular composition of interstellar grain mantles”. In: *Astronomy and Astrophysics* 114 (1982), pp. 245–260.
- [7] R. T. Garrod and E. Herbst. “Formation of methyl formate and other organic species in the warm-up phase of hot molecular cores”. In: *Astronomy & Astrophysics* 457.3 (2006), p. 10.
- [8] H. M. Cuppen and Eric Herbst. “Simulation of the Formation and Morphology of Ice Mantles on Interstellar Grains”. en. In: *The Astrophysical Journal* 668.1 (Oct. 2007), p. 294.
- [9] George E. Hassel, Eric Herbst, and Robin T. Garrod. “Modeling the Lukewarm Corino Phase: Is L1527 Unique?” en. In: *The Astrophysical Journal* 681.2 (July 2008), p. 1385.
- [10] R. T. Garrod, V. Wakelam, and E. Herbst. “Non-thermal desorption from interstellar dust grains via exothermic surface reactions”. In: *Astronomy & Astrophysics* 467.3 (2007), p. 13.
- [11] M. Prutton. *Introduction to Surface Physics*. Oxford science publications. Clarendon Press, 1994.
- [12] A. Zangwill. *Physics at Surfaces*. Cambridge University Press, 1988.
- [13] E.M. McCash. *Surface Chemistry*. Oxford University Press, 2001.
- [14] M. Bertin et al. “Adsorption of Organic Isomers on Water Ice Surfaces: A Study of Acetic Acid and Methyl Formate”. In: *The Journal of Physical Chemistry C* 115.26 (2011), pp. 12920–12928.
- [15] M. Lattalais et al. “Differential adsorption of complex organic molecules isomers at interstellar ice surfaces”. In: *Astronomy & Astrophysics* 532 (Aug. 2011), A12.
- [16] Mark P. Collings et al. “A laboratory survey of the thermal desorption of astrophysically relevant molecules”. en. In: *Monthly Notices of the Royal Astronomical Society* 354.4 (Nov. 2004), pp. 1133–1140.

- [17] Serena Viti et al. “Evaporation of ices near massive stars: models based on laboratory temperature programmed desorption data”. en. In: *Monthly Notices of the Royal Astronomical Society* 354.4 (2004), pp. 1141–1145.
- [18] Victoria Buch * et al. “Solid water clusters in the size range of tens–thousands of H₂O: a combined computational/spectroscopic outlook”. In: *International Reviews in Physical Chemistry* 23.3 (2004), pp. 375–433.
- [19] M. Lattalais et al. “Differential adsorption of CHON isomers at interstellar grain surfaces”. In: *Astronomy & Astrophysics* 578 (June 2015), A62.
- [20] G. Kresse and J. Hafner. “\textit{Ab initio} molecular dynamics for open-shell transition metals”. In: *Physical Review B* 48.17 (1993), pp. 13115–13118.
- [21] G. Kresse and J. Hafner. “\textit{Ab initio} molecular-dynamics simulation of the liquid-metal\char21{ }amorphous-semiconductor transition in germanium”. In: *Physical Review B* 49.20 (1994), pp. 14251–14269.
- [22] H. B. Niemann et al. “The abundances of constituents of Titan’s atmosphere from the GCMS instrument on the Huygens probe”. en. In: *Nature* 438.7069 (2005), pp. 779–784.
- [23] John P. Osegovic and Michael D. Max. “Compound clathrate hydrate on Titan’s surface”. en. In: *Journal of Geophysical Research: Planets* 110.E8 (2005), E08004.
- [24] C. Thomas et al. “A theoretical investigation into the trapping of noble gases by clathrates on Titan”. In: *Planetary and Space Science. Surfaces and Atmospheres of the Outer Planets, their Satellites and Ring Systems, Part IV Meetings held in 2007: EGU: PS3.0 & PS3.1; IUGG/IAMAS:JMS12 & JMS13; AOGS: PS09 & PS11; EPSC2: AO4 or PM1* 56.12 (2008), pp. 1607–1617.
- [25] Olivier Mousis et al. “Removal of Titan’s Atmospheric Noble Gases by Their Sequestration in Surface Clathrates”. en. In: *The Astrophysical Journal Letters* 740.1 (Oct. 2011), p. L9.
- [26] D. Cordier et al. “About the Possible Role of Hydrocarbon Lakes in the Origin of Titan’s Noble Gas Atmospheric Depletion”. en. In: *The Astrophysical Journal Letters* 721.2 (Oct. 2010), p. L117.
- [27] Ronen Jacovi and Akiva Bar-Nun. “Removal of Titan’s noble gases by their trapping in its haze”. In: *Icarus* 196.1 (2008), pp. 302–304.
- [28] Antti Lignell et al. “On theoretical predictions of noble-gas hydrides”. In: *The Journal of Chemical Physics* 125.18 (Nov. 2006), p. 184514.
- [29] O. Mousis et al. “Sequestration of Noble Gases by H+3 in Protoplanetary Disks and Outer Solar System Composition”. en. In: *The Astrophysical Journal* 673.1 (Jan. 2008), p. 637.
- [30] F. Pauzat et al. “Gas-phase Sequestration of Noble Gases in the Protosolar Nebula: Possible Consequences on the Outer Solar System Composition”. en. In: *The Astrophysical Journal* 777.1 (Nov. 2013), p. 29.
- [31] P. P. Tennekes et al. “HCN and HNC mapping of the protostellar core Chamaeleon-MMS1”. In: *Astronomy & Astrophysics* 456.3 (2006), p. 7.

- [32] A. Fuente et al. “Observational study of reactive ions and radicals in PDRs”. In: *Astronomy & Astrophysics* 406.3 (2003), p. 15.
- [33] Anthony J. Remijan et al. “A Survey of Large Molecules toward the Proto-Planetary Nebula CRL 618”. en. In: *The Astrophysical Journal* 626.1 (June 2005), p. 233.
- [34] J. Cernicharo et al. “Tentative detection of CH₃NC towards SGR B2”. In: *Astronomy and Astrophysics* 189 (1988), p. L1.
- [35] G. Cremonese et al. “Neutral Sodium from Comet Hale-Bopp: A Third Type of Tail”. en. In: *The Astrophysical Journal Letters* 490.2 (Dec. 1997), p. L199.
- [36] G. Cremonese et al. “Neutral sodium tails in comets”. In: *Advances in Space Research* 29.8 (2002), pp. 1187–1197.
- [37] F. Leblanc et al. “Comet McNaught C/2006 P1: observation of the sodium emission by the solar telescope THEMIS”. In: *Astronomy & Astrophysics* 482.1 (2008), p. 6.
- [38] Anita L. Cochran et al. “Spatially Resolved Spectroscopic Observations of Na and K in the Tail of Comet C/2011 L4 (PanSTARRS)”. en. In: *AAS/Division for Planetary Sciences Meeting Abstracts*. Vol. 45. Oct. 2013.
- [39] W.-H. Ip and L. Jorda. “Can the Sodium Tail of Comet Hale-Bopp Have a Dust-Impact Origin?” en. In: *The Astrophysical Journal Letters* 496.1 (Mar. 1998), p. L47.

Part I

Employed Methods

Chapter 2

Experimental approach

This chapter describes all the aspects of experimental study of adsorption of astrophysically relevant species on models of ISM grain surfaces.

First part presents the experimental setup and gives some insights on the principals of instruments operation. Various experimental issues are discussed, including reproducibility and accuracy.

An introduction to the Temperature Programmed Desorption (TPD) technique is given in the second part.

In the last part the experimental method is described in detail. Data treatment procedure is demonstrated using the example of Methanol (CH_3OH) adsorption on graphite.

2.1 Experimental setup

SPICES, acronym for Surface Processes and ICES, is an experimental setup developed since 2010 in Laboratoire d'Études du Rayonnement et de la Matière en Astrophysique et Atmosphères (LERMA), Pierre and Marie Curie University, Paris, France. It is an ultrahigh vacuum (UHV) setup intended to study thermal and ultraviolet/VUV photodesorption of species from astrophysically relevant surfaces. Designed as a mobile experiment, it can be transported and coupled to a synchrotron radiation source to study photodesorption. When not coupled to a light source, it can be employed to study thermal desorption.

2.1.1 General description and characteristics

Conditions in the cold regions of the ISM are characterized by extreme low temperatures (below 100K) and densities of some hundreds of molecules per cm^3 , c.f. Chapter 1.1 and e.g. [1].

To study the interaction of gases and models of interstellar grains, UHV (2.1.4) and cryogenic temperature (2.1.2) conditions are necessary. Need for ultra-high vacuum comes from the fact that sample surfaces need to be kept clean. Low desorption temperatures of 10-15K for Hydrogen H_2 , 25-45K for diatomic molecules like CO and N_2 , and 100-150K for water and small organic like CH_3OH justify the need of cryogenic temperatures at such low pressures.

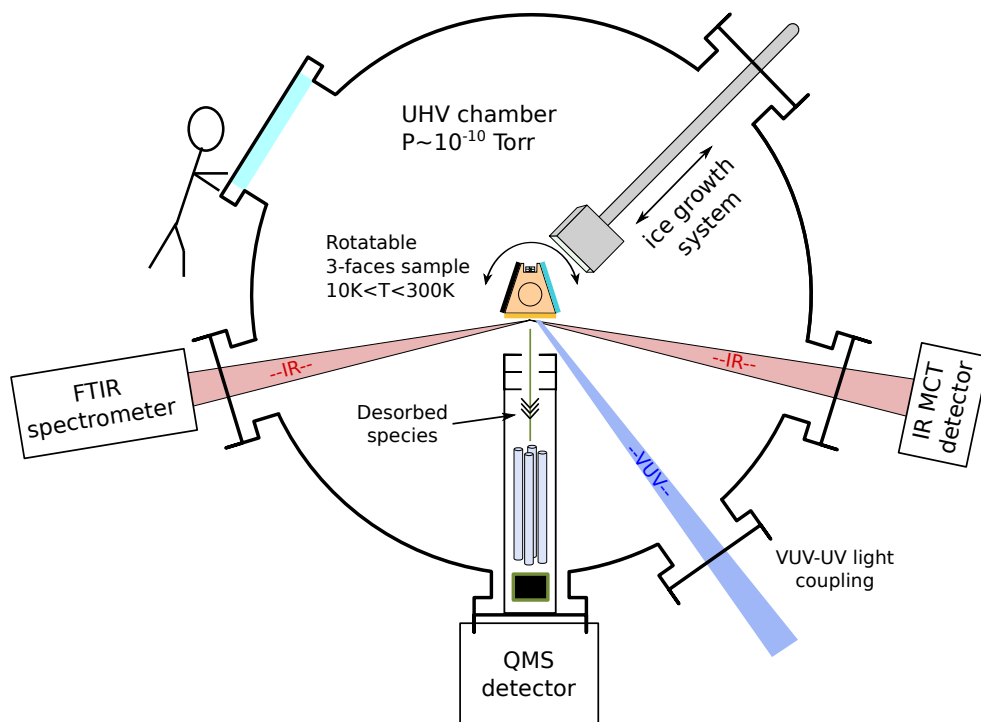


Figure 2.1 – SPICES UHV chamber instruments

A schematic diagram of SPICES UHV chamber is presented on a figure 2.1.

SPICES setup has three sample surfaces: polycrystalline gold, quartz (alpha-0001) and highly-oriented pyrolytic graphite (HOPG), mounted on a sample holder on a tip of the cryocooler cold finger (sect. 2.1.2 a). Temperature of the sample holder and surfaces is controlled within the range of 10 to 300 Kelvin, with 0.01K precision and absolute accuracy of 0.5K (sect. 2.1.2 b). Cryostat assembly is mounted on a rotatable stage, permitting to orient the surface of interest against the dosing line or facing the QMS.

Ices are grown on sample surfaces in situ using a retractable dosing line (see sections 2.1.5, 2.1.6).

To probe the adsorbate in the condensed state a Fourier-Transform Infrared (FTIR) spectrometer is used (namely Bruker Vector 22 with Mercury Cadmium Telluride (MCT) detector), working in reflection-absorption mode.

Desorbed species are detected with a QMS, Pfeiffer Vacuum Prisma 80 with channeltron detector (see section 2.1.3 for details).

Pressure in the vacuum chamber is monitored using a Bayard-Alpert gauge, in junction with Varian Multi-Gauge controller. The chamber is pumped with a high-performance turbomolecular pump (Pfeiffer Vacuum HiPace 800), backed by a dry scroll pump (Pfeiffer Vacuum XDS-10). Base pressure stays in a range of $1.5 \cdot 10^{-10}$ to $4 \cdot 10^{-10}$ mbar, depending on the experiment history.

2.1.2 Cryogenics and temperature control

To control the substrate temperature in a range of cryogenic temperatures, three elements are necessary: a heat sink (cryocooler, see 2.1.2 a), heat source (electric resistive heater) and a temperature sensor (silicone diode) located as close to the controlled point as possible.

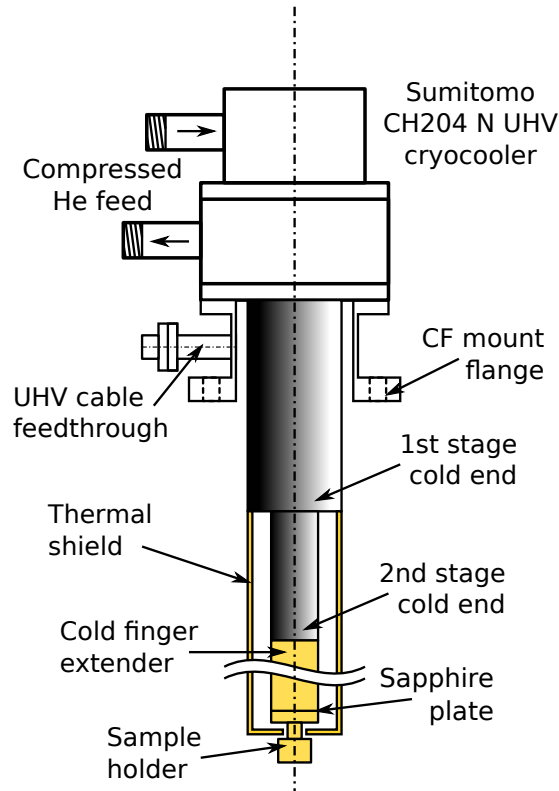


Figure 2.2 – SPICES cryostat assembly diagram.

A diagram of SPICES cryostat assembly is shown on the figure 2.2. Cryocooler is a commercial Gifford-McMahon type closed-cycle helium type, Sumitomo CH-204 model. A home-made sample holder is attached to the cryocooler cold finger through the oxygen-free high thermal conductivity (OFHC) copper extender. A sapphire (Al_2O_3) crystal plate is inserted between the cryocooler extender and the sample holder to reduce the heat transfer when operating at high temperatures (above 70-100K). Cryogenic part is isolated by a gold-plated OFHC copper thermal shield kept at temperatures around 100K to avoid heating by the infrared radiation.

Temperature sensor and heater are located on the sample holder (see the fig. 2.4a, sect. 2.1.2 b). Cryocooler operates constantly at maximum cooling power, while heater output is varied according to PID algorithm (see sect. 2.1.2 b) as a function of temperature sensor readings and target temperature.

Cool-down time from 300K to 10K is of about 90 minutes for SPICES setup.

2.1.2 a Helium closed cycle cryocooler

With considerably improved reliability and reduced dimensions and costs over last twenty years, cryocoolers became of widespread use for the applications where cryogenic temperatures are necessary.

Advantage of closed cycle He cryocoolers over open circuit system is reduced operation cost: cryocoolers operate for long periods without or with little maintenance. For example, a maintenance interval of cryocooler used in SPICES setup is 13000 hours, that is a year and a half of constant operation.

The only disadvantage of Gifford-McMahon cryocoolers is the vibration induced by moving parts of the cryostat. Although not an issue for our experiment, it renders impossible the usage of GM cryocoolers in junction with vibration-sensitive surface science methods like STM and AFM microscopy, as well as techniques that need to have the top surface layer in the focal plain (X-ray diffraction).

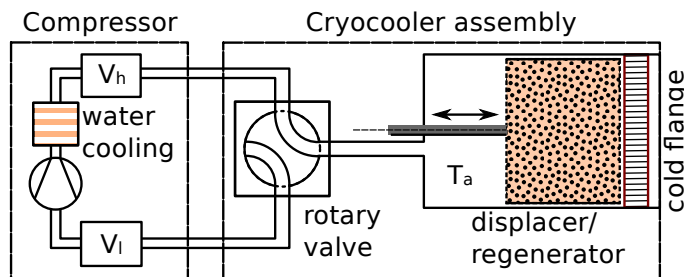


Figure 2.3 – Gifford-McMahon cryocooler schematic diagram

A schema of a Gifford-McMahon cryocooler [2] stage is shown on a figure 2.3. It uses compressed helium at room temperature. A working volume may be connected to the high or the low pressure lines of a compressor with help of a rotary valve. Displacer/regenerator piston is actuated synchronously to the valve. Refrigeration cycle consists of four steps:

- Displacer is in the extreme right position, cold volume is minimal. Working volume is connected to the high-pressure line and is filled up to the high pressure.
- Displacer moves to the extreme left position, helium is passing through the regenerator to the cold volume and is precooled to the temperature of cold space.
- The valve connects the working volume to the low-pressure line, helium is cooled down during the expansion, taking a portion of heat from cold space heat exchanger and regenerator.
- Displacer moves back to the extreme right position, reducing the volume of the cold part to a minimum. The cycle is closed, the system is back to the state where it was before the first step.

In ideal conditions an amount of heat taken from the cold space is equal $(p_h - p_l)V$ where p_h is the helium feed pressure, p_l the return pressure and V the expansion volume in the cryostat cold head.

Two or three stages may be stacked one after another to reach extreme cold temperatures down to 4K. Modern cryocoolers operate with temperatures around 30K on the first stage, 10K on the second stage and down to 4K on the third stage. The lowest attainable temperature on the third stage is limited by helium gas-liquid transition. Use of proper pre-cooled thermal shield is necessary to isolate the cryogenic stage from the infrared radiation.

Physics of cryocoolers is described in a paper of Waele [3], and a general review of current state and progress in cryocoolers development is given by Radebaugh [4].

2.1.2 b Temperature measurement and control

Temperature of the sample is measured by a silicone diode (calibrated LakeShore DT-670) mounted on a sample holder (see fig. 2.4a). Diode needs to be placed as close to the sample as possible to provide accurate readings. To compensate for cable resistance, a four-wire connection schema is used (fig. 2.4b). Current is fed through one pair, voltage drop on diode junction is measured through another. This approach allows to achieve stable and accurate temperature readings, whatever the length of the cables.

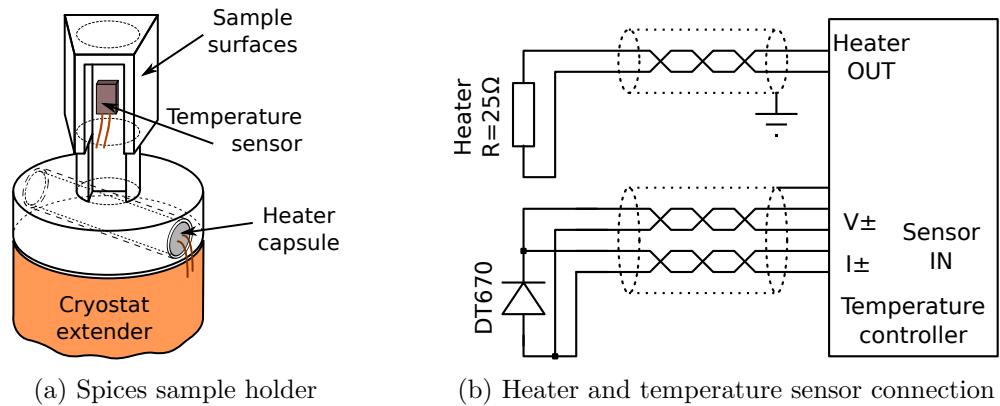


Figure 2.4 – Sample holder schema and connection diagram

For the cryogenic part, a twisted phosphor bronze wire is used to limit thermal transfer over the diode leads. Shielded double twisted pair cable is used for connection between the cryostat and the temperature controller.

A resistive cartridge is used as a source of heat. Variable power applied to the heater to maintain the sample temperature is controlled by LakeShore 336 using Proportional-Integral-Derivative (PID) algorithm.

2.1.2 c PID control

Initially developed in the beginning of 20th century for automatic guidance of transatlantic ships, PID control principle is widely used nowadays to control parameters of systems for which a complete model of disturbing factors can not be developed.

Control parameter value $U(t)$ is set as a function of feedback error signal $e(t)$ and its evolution over time (2.1).

$$U(t) = P \cdot e(t) + I \int_0^t e(t)dt + D \frac{de(t)}{dt} \quad (2.1)$$

Here P is a proportional, I an integral and D a derivative term. For the case of temperature control $e(t)$ is the difference between the setpoint temperature T_s and the actual temperature T_a : $e(t) = T_s - T_a$.

Various approaches and methods exists to determine control parameters. In our case, the temperature controller is equipped with auto-tune feature, allowing to determine optimal control parameters for a certain temperature.

System properties and thus control parameters change considerably with the sample temperature: for example OFHC copper thermal conductivity and specific heat change from $[1000; 10000] \frac{W}{mK}$ and $5 \frac{J}{kgK}$ at 18K to $500 \frac{W}{mK}$ and $100 \frac{J}{kgK}$ respectively at 80K (NIST monograph 177 [5]).

Temperature zones are used to compensate for this: control parameters are calibrated for different temperature ranges using the controller auto-tune feature. Parameter values are given in the Appendix A.

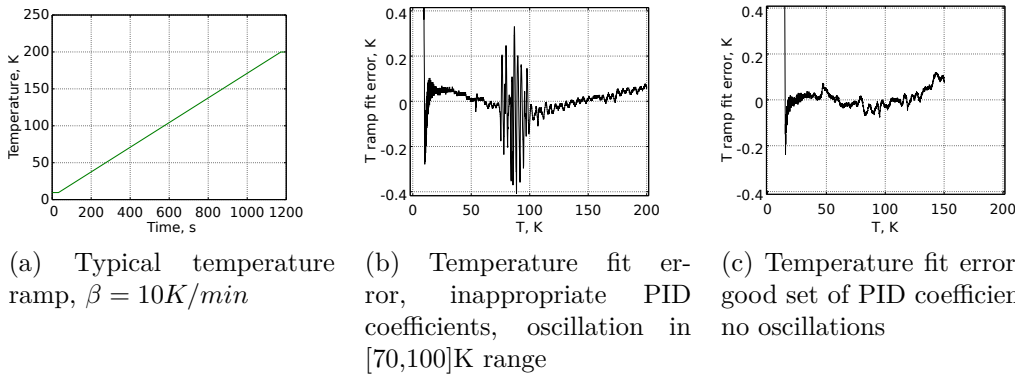


Figure 2.5 – Temperature ramp and fit errors

For the experimental technique used in this work (c.f. sect 2.2) the sample temperature is varied linearly against time: $T(t) = T_0 + \beta t$ (temperature ramp), over a wide range from 10K to 200K with heating rates $\beta = [1,15] \frac{K}{min}$. A typical heating ramp is presented on a fig. 2.5a. Thus, a criteria for a good set of PID parameters is the linearity of the ramp and the absence of oscillations in the whole temperature range. If values of P or I coefficients become too high for a certain temperature range, oscillations may occur (fig 2.5b). Reducing the coefficient values or rearranging temperature zones may considerably improve the situation (fig 2.5c).

2.1.3 Gas phase species detection - quadrupole mass spectrometer (QMS)

Quadrupole mass spectrometer (QMS) consists of three principal elements: ionization chamber, quadrupole mass filter, ions detector, schematically shown on a figure 2.6

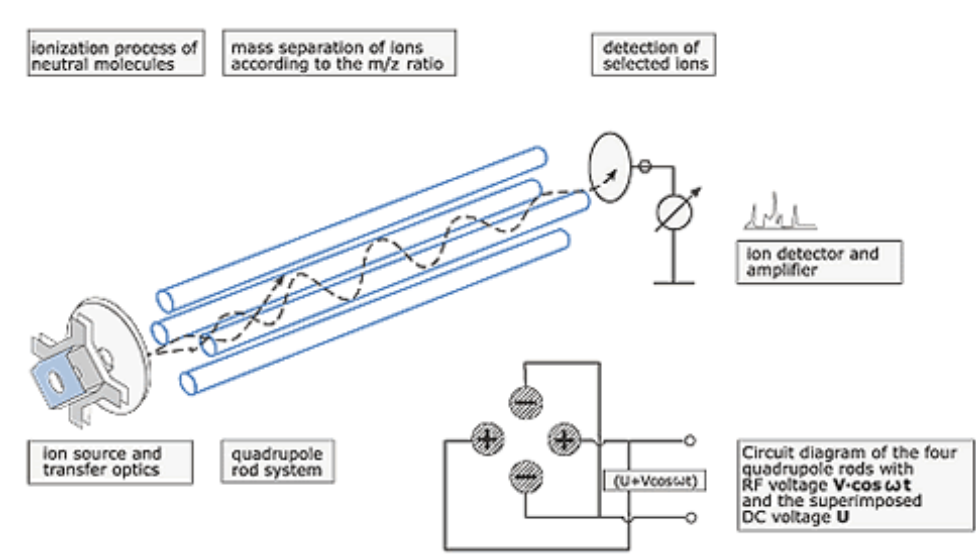


Figure 2.6 – Quadrupole mass spectrometer elements

Neutral species desorbed from the surface are first ionized by electron impact in the QMS *Ionization Chamber* producing positively-charged ions and fragments. Ions, collected and accelerated by electrostatic lenses, are then injected into *Quadrupole Mass Filter*. Filtered ions that are corresponding to the selected mass/charge ratio are then captured by an *Ion Detector*.

2.1.3 a Ionization Chamber

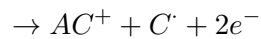
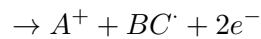
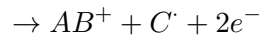
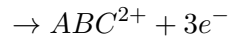
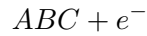
Ion source of the SPICES mass spectrometer is an open-type high sensitivity electron impact ionization source. Electron energy is chosen as 90 eV, which is close to a maximum of the ionization cross-section for most of the atoms and molecules [6].

For the case of atoms, electron impact with atom A produces mostly positively charged atoms A^+ and a small fraction of multiply-charged atoms A^{++} . Isotope peaks may be observed at neighbour mass values. As an example, mass spectra of Ar is shown on a fig. 2.7a. A peak of Ar^+ is observed at $m/z = 40$, additional peak corresponding to Ar^{2+} is observed at $m/z = 20$

Mass spectrum of molecules is much more complex. Additionally to a single-charged positive ion ABC^+ , an electron impact on molecule ABC may produce a bunch of fragments:

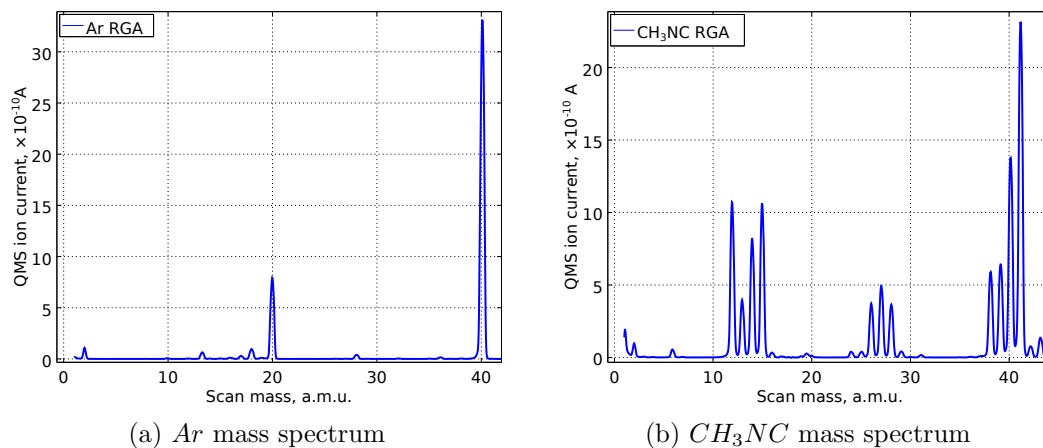
Table 2.1 – CH_3NC fragments mas spectrum attribution

m/z	1	2	6	12	13	14
ion	$H^+{}^a$; $H_2^{2+}{}^{d,e}$	$H_2^+{}^d$	$C^{2+}{}^e$	$C^+{}^a$	$CH^+{}^b$	$CH_2^+{}^b$; $N^+{}^a$
m/z	15	16	26,27,28	38,39,40	41	42,43
ion	$CH_3^+{}^b$	$^{13}CH_3^+{}^{b,c}$	$CH_xN^+{}^{b,f}$	$CH_xNC^+{}^{b,f}$	$CH_3NC^+{}^d$	$CH_3NC^+{}^{d,c}$

^a atomic ion^b fragment ion^c isotopologue^d intact ion^e multiple ionized^f x=0,1,2

Each molecule has its own unique fragments spectra. Chemical databases of fragments spectra are available and may be used to identify the species [7].

For example, on a figure 2.7b a mass spectra of methyl izocyanide (CH_3NC) is presented. One may note that along with a principal peak of intact CH_3NC^+ ($m/z = 41$) multiple peaks corresponding to fragment ions may be identified. A summary and attribution of fragments to m/z ratio for the most intense peaks is given in a Table 2.1.

Figure 2.7 – Mass spectra of Ar atom and CH_3NC molecule and its fragments

2.1.3 b Quadrupole Mass Filter

Quadrupole mass filter was first described by W. Paul, and H. Steinwedel in 1953. It revolutionized the mass spectrometry: contrary to previous designs it employs no magnets; all the filter parameters are controlled by the applied electric field. Such a design favours reproducibility and temporal stability of the mass filter characteristics.

Quadrupole mass filter is composed of four conductive rods, with a distance r_0 between them, interconnected pairwise. A sum of two potentials: a constant U and oscillating $V \cdot \cos(\omega t)$ is applied between pairs of electrodes.

Motion of ions having mass m and elementary charge e in the electric field of the filter is described by equations (2.2) (2.3). Here x and y axes are orthogonal to rods and mass filter transmission axe z .

$$\frac{d^2x}{dt^2} + \frac{e}{mr_0^2}(U - V\cos\omega t)x = 0 \quad (2.2)$$

$$\frac{d^2y}{dt^2} - \frac{e}{mr_0^2}(U - V\cos\omega t)y = 0 \quad (2.3)$$

Those are Mathieu type of equations. They can be solved numerically, giving a set of periodic trajectories. Trajectories remain finite (stable) in x and y plains for values of parameters $a = \frac{8eU}{m\omega^2r_0^2}$ and $q = \frac{4eV}{m\omega^2r_0^2}$ laying within stability region (see fig. 2.8). Stability of the trajectory depends only on parameters a and q and is not affected by the initial conditions.

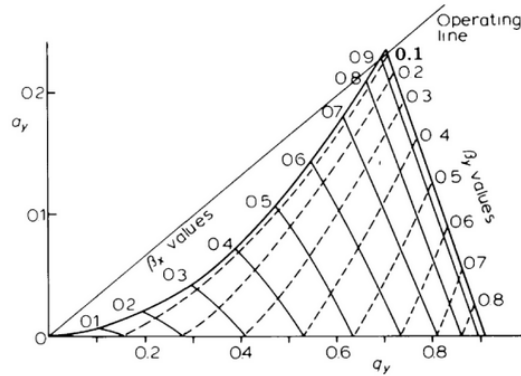


Figure 2.8 – Stability region for parameters a and q of x and y plains, ref.[8]

Practically spectrometers operate at a constant ratio of U and V (operating line on the fig. 2.8), mass resolution is determined by intersection of operating line with the borders of the stability region. Radio frequency ω is kept constant. For Prisma QMA-200 spectrometer used in SPICES setup the frequency is 2 MHz.

For more details on the quadrupole mass filter and mass spectrometry c.f. [8]

2.1.3 c Ion Detector

Ions that match stability conditions for the quadrupole filter pass it and arrive to the particle detector, either a Faraday cup or a secondary electron multiplier (SEM).

Faraday cup detector is a simple electrode. It is connected to a sensitive electrometer amplifier, converting the ion current to the output voltage.

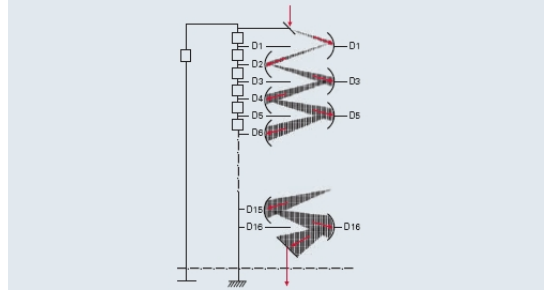


Figure 2.9 – Secondary electron multiplier detector diagram

SEM, depicted on a fig. 2.9 is a physical preamplifier. It consists of a series of electrodes covered with materials having a low electron work-function. When an ion hits the first dynode, it kicks out few (1 to 5) electrons, they are then accelerated by a positive potential difference and hit the next stage of the amplifier. Subsequently repeated, multiplication steps produce a bunch of electrons for every ion that hits the first electrode. Typical amplification factor of a secondary electron multiplier is of 10^7 .

SEM detector has much higher sensitivity than Faraday cup detector: it provides a minimal detectable partial pressure of $P_{min} \approx 10^{-14} mbar$.

Limitations for SEM detector uses are:

- it needs high vacuum to operate (below $10^{-6} mbar$)
- amplification factor is sensitive to electrodes contamination

Linearity of the QMS with SEM detector used in SPICES setup was tested with *Ar* and proved itself to be extremely linear up to the detector limit pressure of $10^{-6} mbar$.

The minimal measurable partial pressure of the QMS with SEM is limited by the noise levels of the amplifier, and is of about $P_{min}(N_2) \approx 10^{-13} mbar$ for our case.

2.1.4 Ultra-High Vacuum

In order to keep the sample surface clean during the time of the experiment, ultra-high vacuum conditions are necessary. For example, for the background pressure of $10^{-9}mbar$ it will take approximately 1000s or 17 minutes to grow a monolayer (10^{15} molecules/cm for H_2O ice) of adsorbate on the surface. For a pressure of $10^{-10}mbar$ it will become 10^4s or a bit less than 3 hours.

For a typical experiment time of 30 to 50 minutes, base pressures of $10^{-10}mbar$ range or better are needed to keep the sample surface clean before the adsorbate deposition and during the measurement.

To reach ultra-high vacuum conditions, special measures need to be taken: All-metal vacuum system should be used, with oxygen-free copper gaskets (CF standard). A list of usable materials is very limited, most of plastics (except PTFE and polyimide), greases and micro-porous materials like Aluminium may not be used.

Vacuum system needs to be constantly pumped with high-performance turbomolecular pump.

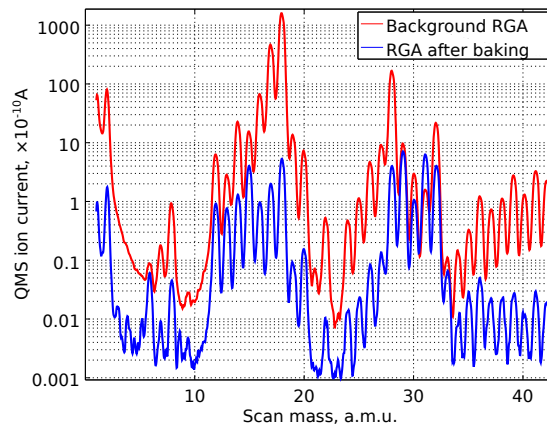


Figure 2.10 – Background pressure mass signal

A residual gas analysis (RGA) spectrum of vacuum is presented on a figure 2.10. Main pollutants of the vacuum are:

- Hydrogen (H_2), which is not effectively pumped by turbomolecular pump, and the flow of hydrogen through metal walls of the vacuum system balances the pumping speed.
- Water (H_2O , mass 18), which sticks to the walls of the vacuum chamber and takes a long time to evacuate.
- Carbon monoxide (CO , mass 28), produced inside vacuum chamber by cracking organic molecules on hot filaments.

Hydrogen contamination is not an issue for this study: working temperatures are above 20K for desorption of the majority of studied adsorbates, and in those conditions hydrogen molecules stay in gas phase and do not interfere with adsorbates. For studies

where hydrogen contamination becomes a problem, that is for those that need ultracold temperatures of around or below 10K, hydrogen may be removed from gas phase with help of ionic pumps.

Another major contaminant, water (H_2O) adsorbs at 130-150K and thus is a principal contaminant that needs to be evacuated. Turbomolecular pumps are efficient to evacuate water, however due to effective sticking of water molecules to vacuum system walls, it takes an extremely long time to evacuate the system to base pressures below 10^{-9} mbar. Typical pumping time after the experiment exposure to atmospheric pressure is about a week or two.

Pumping time to reach ultrahigh vacuum (UHV) conditions may be considerably reduced thanks to a procedure called baking: It consists of slowly heating up all the elements of the vacuum system to temperatures of 100-180°C while constantly pumping the system. After a day of heating, when the pressure inside hot vacuum system drops down to 10^{-9} mbar it can be cooled back down to operating temperature. Care should be taken to perform all the heating and cooling procedures slowly, in order to reduce mechanical stress and risk of leaks. In our case, baking-out at 100°C during a few days is sufficient to reach the base pressure of 10^{-10} mbar.

2.1.5 Sample species vapour preparation module

To grow ices an adsorbate in a gas phase is injected into the vacuum system through a doser line. Vapours and mixtures of different gases are prepared and maintained in a dedicated vacuum system module (see fig. 2.11).

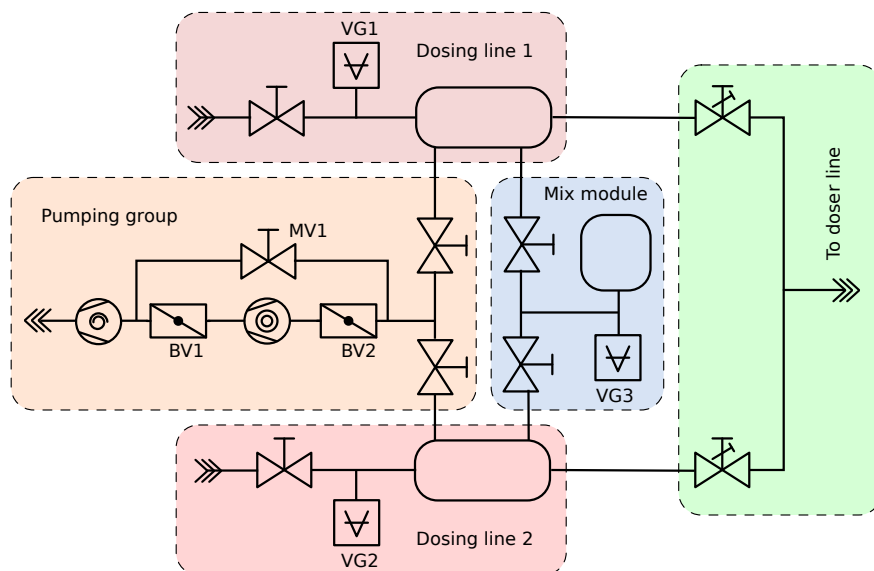


Figure 2.11 – Sample species preparation module

Vapour preparation system includes two ballast volumes (dosing lines) directly connected to the doser via leak valves. Pressure inside lines is monitored by thermal conductivity gauges VG1 and VG2 respectively.

Dosing lines are evacuated through a pumping group containing a turbomolecular

pump and a dry scroll pump. Turbomolecular pump may be isolated by valves BV1 and BV2 and bypassed by the valve MV1 to quickly evacuate near-atmospheric pressures.

Calibrated mixtures of gases are prepared in mixing volume, real partial pressures are monitored using a capacitive gauge VG3.

Pure gas adsorbates are injected into dosing lines from gas cylinders through pressure regulators (not shown on the schema).

Liquid adsorbates like water, methanol (CH_3OH) or acetonitrile (CH_3CN) are contained in glass flasks. It is the vapour pressure that is injected. As liquids are stored under atmospheric pressure before being put into flasks, they need to be purified from diluted gases before injection.

Freeze-pump-thaw cycles are used to purify liquids: a flask with liquid sample is connected to the vacuum system. Contents of the flask is frozen by submerging it into the liquid nitrogen. Flask volume is pumped while contents heats up and melts, until the moment when the flow of vaporizing molecules saturates the turbomolecular pump. Then the flask is isolated and once all the liquid is melted a freeze-pump-thaw cycle is repeated. Normally it takes 3 to 4 cycles to completely evacuate diluted atmospheric nitrogen, oxygen and CO_2 from the liquid.

Unstable liquids like methyl isonitrile are additionally kept at low temperatures by submerging the flask in the icy water bath.

2.1.6 Adsorbate film thickness

To grow a monolayer ($1ML \approx 10^{15}cm^{-2}$ for small molecules) of adsorbate molecules on a cold sample surface it needs to be exposed to a gas pressure of $1 \cdot 10^{-6}mbar$ for one second. By definition it is a unit of exposure, Langmuir (**L**).

In practice pressures around $1 \cdot 10^{-8}mbar$ and exposure times of about 100 seconds are used.

The deposition technique that consists of introducing the gas in the whole chamber is called the background deposition. A disadvantage of background deposition is that all the cold parts of the cryostat get polluted with adsorbate, therefore it becomes impossible to distinguish species desorbing from the sample surface and those desorbing from other elements of the cryostat.

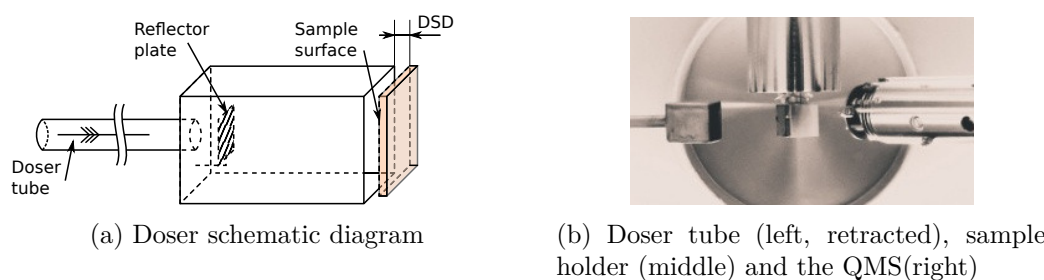


Figure 2.12 – SPICES doser and sample surfaces

A dosing tube is intended to solve the issue of the vacuum contamination. Shown on the figure 2.12a, doser enables to contain a high ($10^{-8}mbar$) pressure in the vicinity of the sample surface, while keeping the background pressure inside the main vacuum chamber below $5 \cdot 10^{-10}mbar$.

A fraction of adsorbate molecules escapes the doser volume through the doser-surface gap, permitting to detect the deposition flow by means of the QMS. Thickness of an adsorbate film is controlled by regulating the gas flow, while monitoring the background signal over the deposition time (c.f. 2.1.6 c).

2.1.6 a Reproducibility

Reproducibility of the deposited quantity was a major concern for this study. Two main uncertainty factors were identified:

- system geometry needs to be kept stable, fixing a distance between the doser and the surface
- deposition signal needs to be properly integrated over the time

2.1.6 b Doser-surface distance

The influence of the doser-surface distance (DSD) on the ratio of desorption and dose signal integrals $\frac{I_{TPD}}{I_{dos}}$ was evaluated with the adsorption of Kr atoms on the amorphous H₂O ice film. Several sets of desorption experiments were performed, with H₂O ice deposited on gold and graphite substrates.

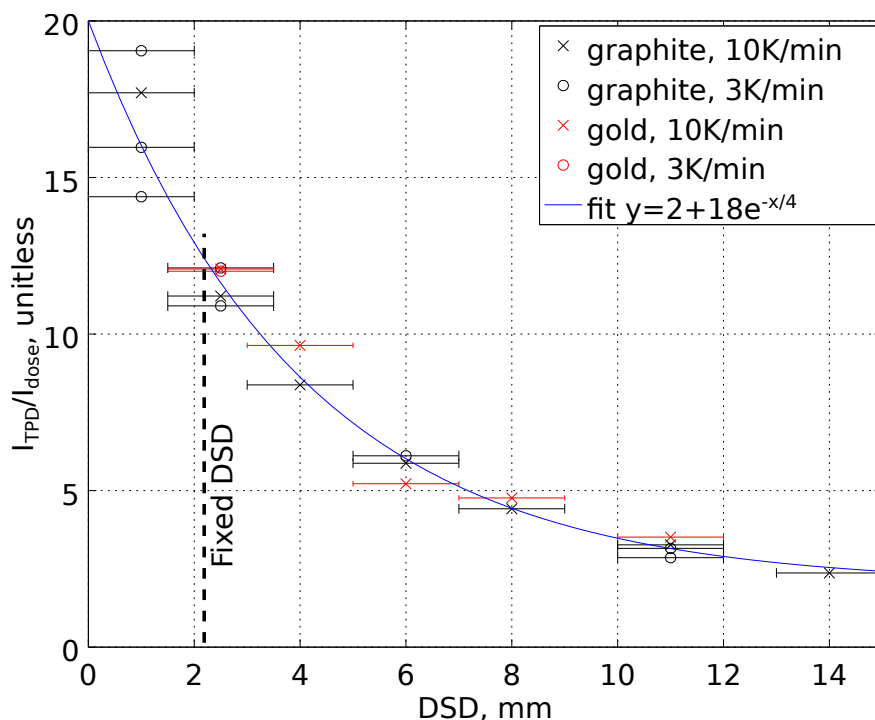


Figure 2.13 – TPD and dose signal integral ratio as a function of the doser-surface distance. Kr adsorption on the amorphous H₂O ice film.

Integral ratio is plotted on the figure 2.13. At high distances the ratio converges to a value of 2, which corresponds to a background deposition ratio for the SPICES setup geometry. When the doser is placed closely to the surface, less adsorbate molecules

escape the surface and the ratio increases. The higher is that ratio, the less is the parasite adsorption on the cryostat, but the dose uncertainty is also increasing.

Finally, the doser-surface distance was chosen as 2 mm as a compromise between the good reproducibility and decreased contamination. DSD is fixed mechanically by a stopper ring on the doser translator. Additionally that ring serves as a safety measure, prohibiting the doser to touch the surface.

2.1.6 c Signal integration and dose end detection

To precisely reproduce the adsorbate deposited quantity, it is necessary to know when to interrupt the gas flow through the doser. The moment to close the valve may be predicted by calculating the deposition signal integral during the dose.

In any moment of time t_c the total deposition signal integral may be decomposed in two parts: (2.4)

$$I_{dose} = \underbrace{\int_0^{t_c} i(t) dt}_{I_{(1)}} + \underbrace{\int_{t_c}^{\infty} i(t_c) e^{-\alpha(t-t_c)} dt}_{I_{(2)}} \quad (2.4)$$

The first part corresponds to a numerically integrated signal over time. Second part gives the prediction of the doser outgasing integral in the approximation of non-sticking adsorbate. A typical QMS signal during the dose is shown on the figure 2.14

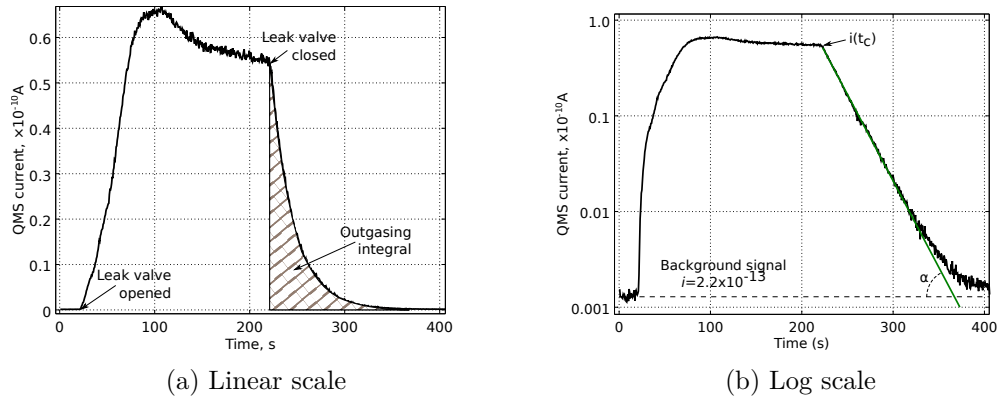


Figure 2.14 – QMS signal during deposition of 5ML thick Xe film on top of amorphous H_2O ice film.

Real-time deposition signal integration was implemented in the experiment control software. In practice first integral is calculated as a sum using trapezoid method. Analytic solution $I_{(2)} = \alpha i(t_c)$ of the second integral is added to predict the total integral. A final equation to predict the dose integral takes the form (2.5).

$$I_{dose} = \underbrace{\sum_n \phi(t) (t_i - t_{i-1})}_{I_{(1)}} + \underbrace{\alpha \phi(t_c)}_{I_{(2)}} \quad (2.5)$$

Here $\phi(t) = i(t) - \min(i)$ is the mass signal with background extracted. A sliding average over 5 points is used to reduce the effect of noise on the outgassing signal start value $\phi(t_c)$. Predicted integral I_{dose} is compared to the desired dose integral I_{set} . User is notified when the dose integral reaches 95% and 99% of the desired value in order to close the leak valve at the correct moment.

2.1.6 d Conclusion

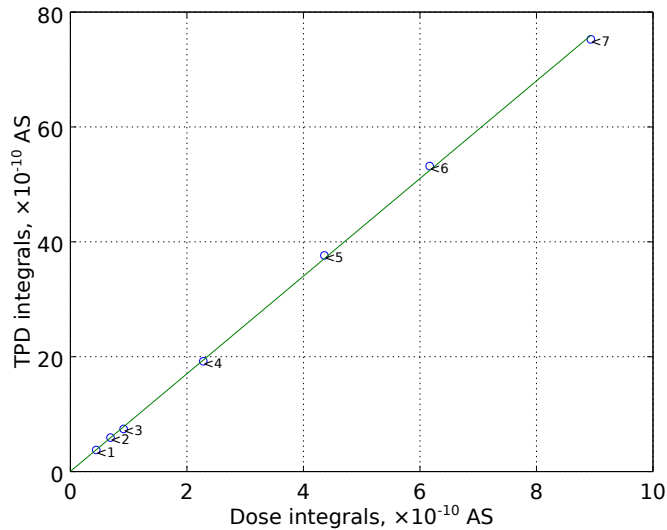


Figure 2.15 – Desorption integral as a function of deposition signal integral. Xe adsorption on 30ML crystal H_2O ice.

Taken together, fixing doser-surface distance and terminating the dose according to the integral calculation enabled to reach the accuracy and reproducibility (instantaneous and day-to-day) of the adsorbate deposition quantity of better than 5% both in multi-layer and sub-monolayer regimes. Such a (high) accuracy is necessary to enable the use of the desorption data analysis technique described later in the section 2.3.3.

Desorption signal integral is linear against deposition signal integral (fig. 2.15). That allows to calibrate the adsorbate thickness in terms of deposition signal integral and reproduce any sub-monolayer surface coverage or adsorbate film thickness.

It should be noted that even for a fixed doser-surface distance, deposition and desorption integral ratio I_{TPD}/I_{dose} stays dependant on the deposition regime (notably, deposition temperature) and the adsorbate itself, indicating that the sticking coefficient is not always equal to one.

2.1.7 Other experimental issues

Few other issues were identified and measures were developed to compensate for them.

2.1.7 a gauge-temperature interference

An interference between the Bayard-Alpert pressure gauge and the temperature readings is observed. The origin of that interference is in the fact that the gauge is using the high voltage of 2kV to measure the ion current, while the temperature controller reads the values of microvolts. Turning on the gauge while the cryostat was at the room temperature induced the error of 20K to the temperature readings.

To resolve the issue, careful connection of all the masses of the experimental setup is required. This allows to reduce the temperature reading error to less than 0.2K at room temperature and enables to perform the experiment with gauge on.

Keeping the gauge on permits to implement an additional safety measure: QMS emission and SEM voltage are cut by the experiment control software once overpressure is detected.

2.1.7 b Background and parasite desorption signal

Although the use of doser allows to amend the problem of the cryostat contamination by adsorbates, it can not be completely resolved. Light gases like Hydrogen, Argon and Carbon Monoxide are producing an important contamination of the cryostat and show a significant background desorption signal.

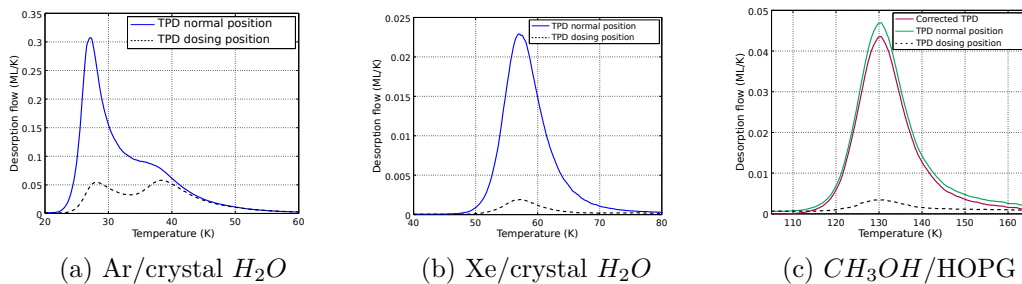


Figure 2.16 – Background and parasite desorption correction. Normal desorption (solid, sample facing the QMS) compared to desorption signal with surface in a dosing position (dashed).

It is possible to amend the background signal problem by performing a control desorption of the similar adsorbate film with sample surface facing the retracted doser. With this geometry, no desorbing molecule can directly get to the QMS ionization chamber, thus the detected signal corresponds entirely to the background signal. As seen on the figure 2.16, Argon (2.16a) shows a significant background desorption signal, thus it is necessary to systematically extract the background signal for Ar desorption study.

Xenon (2.16b) and Methanol (2.16c) on the other hand show a minimal background signal that adds only a small multiplicative factor to the entire desorption signal. There is no need for a systematic background extraction.

2.2 Temperature Programmed Desorption

On a macroscopic scale thermal desorption, as many other thermally-activated processes, is described by the Arrhenius equation (2.6). Desorption flux Φ depends on the temperature T as a function of a system-dependent prefactor A and activation energy E_a (adsorption energy).

$$\Phi(t) = Ae^{-\frac{E_a}{k_b T}} \quad (2.6)$$

Equation (2.6) may be written as Polanyi-Wigner equation to make appear the surface coverage:

$$\Phi(t) = -\frac{d\theta}{dt} = \nu\theta^n e^{-\frac{E_a}{k_b T}} \quad (2.7)$$

The desorption flux is proportional to a number of adsorbed molecules available on the surface (θ) to the power n , number of occasions per second each molecule has the chance to desorb (ν), and a temperature-dependent probability that desorption will occur for each occasion.

To determine the adsorption energy E_a a technique called Temperature Programmed Desorption (TPD) may be employed. It consists of heating up the sample with the adsorbate at a constant rate $\frac{dT}{dt} = \beta$ while registering the desorption signal as a function of the sample temperature. If we switch to a temperature as the independent variable, Polanyi-Wigner equation will take a form:

$$\Phi(T) = -\frac{d\theta}{dT} = \frac{\nu}{\beta}\theta^n e^{-\frac{E_a}{k_b T}} \quad (2.8)$$

Here θ is the surface coverage, defined as the number of adsorption site occupied divided by the total amount of sites (θ is taken equal to 1 for a complete adsorbate layer). ν is a preexponential factor, n the kinetics order, T the substrate temperature.

Flux Φ of desorbing species is detected by QMS. An integral of the desorption curve for monolayer coverage is used as a conversion factor from the QMS current to the flux Φ .

Parameter of interest, adsorption energy E_a , is difficult to access since three parameters are unknown: n , E_a and ν . Therefore, the determined value of adsorption energy is expected to depend on the choice of the two others parameters. Additionally in many cases more than one single adsorption energy should be considered, because of the presence of different adsorption sites on the same surface. Finally, diffusion effects during the sample warming-up may add complexity to the desorption description [9].

Many methods to solve the Polanyi-Wigner equation were developed by different researchers. The three quantities can be simultaneously determined by fitting them as free parameters of the model. Other methods are based on some approximations in order to reproduce with accuracy the experimental data while adding constraints on the parameters (e.g. [10–12]).

In this work a protocol similar to the one used by Koch et al. [13] is developed and implemented. This method allows to determine all the parameters of the Polanyi-Wigner equation (2.8) from a set of experiments at various initial coverages θ_0 and heating rates β . The method is described in detail later in the section 2.3.3.

2.2.1 Desorption kinetics order

Desorption order n depends on the surface morphology and coverage. Desorption of thick multi-layer ices usually follows a zero-order kinetics, while sub-monolayer coverages desorb according to first or second order.

Only integer values of the desorption orders (0,1 and 2) have a straightforward physical meaning. It is possible to choose the desorption order based on the behavior of desorption curves at different coverages.

On a figure 2.17 a model of desorption curves is presented. Here all the parameters but desorption order n are fixed, desorption spectra for two initial coverages $\theta_0 = 0.5ML$ and $\theta_0 = 1.0ML$ are plotted. Adsorption energy is $E_a = 0.130eV$, prefactor $\nu = 10^{12}s^{-1}$, heating rate $\beta = 3K/min$.

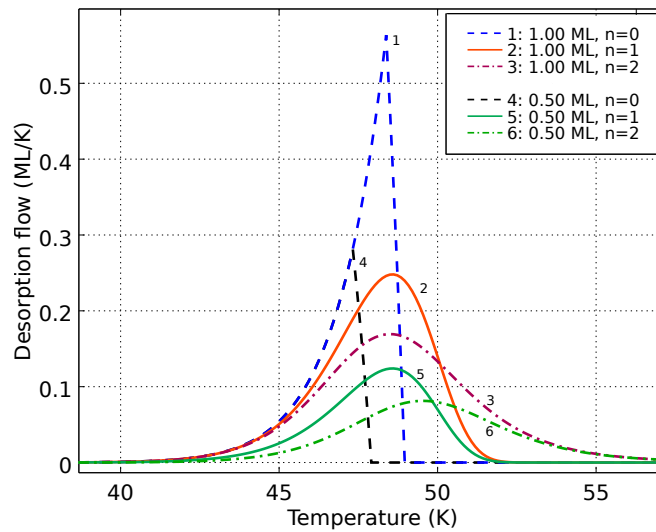


Figure 2.17 – Model of desorption curves, orders $n = 0$ (dashed), $n = 1$ (solid) and $n = 2$ (dash-dotted line) for initial coverages $\theta_0 = [0.5; 1]ML$. $E_a = 0.130eV$, $\nu = 10^{12}s^{-1}$, $\beta = 3K/min$

2.2.1 a Zero-order desorption

An indicator of the zero-th order desorption kinetics is the superposed onset of the desorption curves.

The simplest to understand and treat, zero-th order of desorption, is characteristic for the desorption of thick multi-layer adsorbate film from the surface. Indeed in a system where subsequent layers are indistinguishable from the surface layer and underlying species instantly become available to desorb, desorption flux becomes independent of the total number of adsorbed species, and is sensitive only to the surface area and adsorbate density. Desorption flux increases exponentially as a function of the surface temperature, up till the moment when there is only one layer of the adsorbate is left on the substrate. Desorption kinetics switches to higher order at this moment.

2.2.1 b First order desorption

In the case of sub-monolayer regime and in the approximation of non-interacting adsorbate, desorption flux is directly proportional to the number of adsorbate species still present on the substrate surface ($n = 1$).

First order kinetics is characterized by no overlap between desorption curves taken at different coverages. The temperature of the maximum of desorption flux stays constant. Desorption curves are similar to the multiplicative factor.

2.2.1 c Second and fractional desorption orders

Interaction between adsorbate species may lead to the second or fractional desorption kinetics orders. Pure second order corresponds to a system where formation of a dimer is necessary to trigger desorption. A typical example is the recombination-induced desorption of two radicals.

Overlapping trailing edges of desorption curves taken at different coverages serve as an indicator of the second order desorption. Another indicator is that the temperature of the maximum of desorption flux decreases with increasing coverage. However, inter-sitial diffusion and adsorption energy variation with coverage for the first order desorption, as well as desorption from porous samples may result in a similar behaviour.

Fractional orders may occur in a system where desorption takes place from the edges of adsorbate islands (adsorbate-adsorbate interaction dominates over surface-adsorbate interaction)

In practice the use of higher desorption orders may improve the curve fit accuracy, but has no or minor effect on the determined values of adsorption energy E_a and prefactor ν .

2.2.2 Surface coverage calibration

Coverage variable θ of the Polanyi-Wigner equation (2.8) is a normalized coverage expressed in monolayers (ML). Desorption flux Φ is expressed in monolayer per second (ML/s).

In case when the adsorption energy of the first layer (surface-adsorbate adsorption energy) is notably higher than the adsorbate-adsorbate multilayer adsorption energy, a distinct peak on the desorption curves may be observed. For instance, on a figure 2.18a a model of the desorption curves is presented, with multilayer adsorption energy $E_a^{multi} = 0.120eV$, sub-monolayer $E_a^{subml} = 0.130eV$, prefactor $\nu = 10^{12}s^{-1}$, heating rate $\beta = 3K/min$ different initial coverages $\theta_0 = [0.1..3]ML$. A monolayer calibration coefficient may be determined by integrating the curve for which the low-temperature peak starts to appear, that will give a monolayer desorption integral.

For weakly-bound adsorbate-substrate systems where the monolayer and multilayer peaks are not separated on the energy scale, the only way to calibrate the monolayer coverage is to observe the transition between the sub-monolayer and multilayer regime.

A set of model TPD curves with various initial coverages and equal submonolayer and multilayer adsorption energies $E_a^{multi} = E_a^{subml} = 0.130eV$ is shown on a figure 2.18b. From the curve 1 to the curve 4 the initial coverage increases from 0.1 to 1 ML, desorption follows the first order kinetics. Curves 5 to 7 correspond to initial

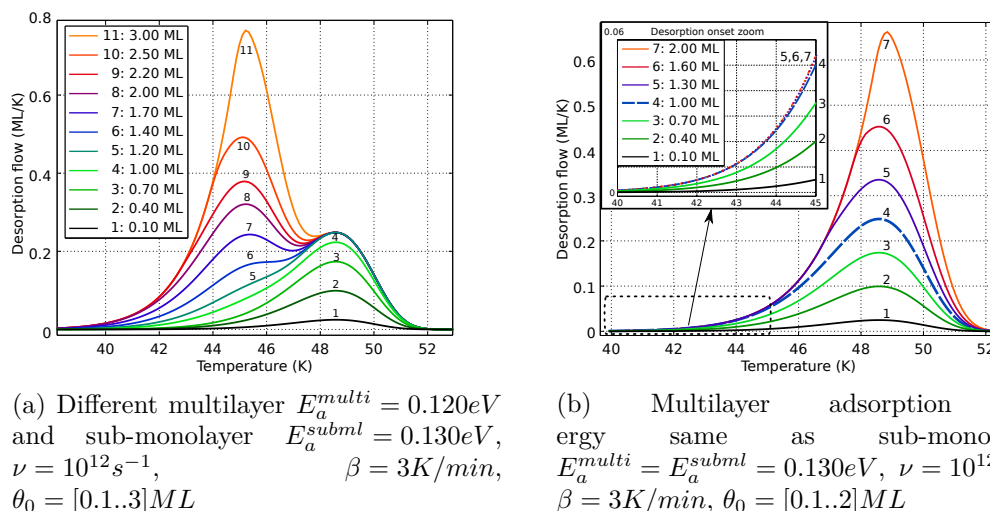


Figure 2.18 – Model TPD curves, transition from sub-monolayer to multilayer regimes

coverages from 1.3 to 2 ML, low-temperature parts are superposed and follow the zero order kinetics. From the moment when there is only a single layer of adsorbate left on the surface, desorption switches to the first order kinetics.

A monolayer calibration coefficient may be determined by integrating the curve for which the onset of desorption superposes with the curve taken at slightly higher coverage (curves 4 and 5). Although less accurate than the calibration for systems with distinct monolayer peak, this calibration is sufficient to choose the ranges used to determine the adsorption energy.

Such monolayer calibrations should be used with caution as they are sensitive to the QMS parameters, the sample surface morphology, as well as the experimental setup geometry, and are thus not directly transferable. Nevertheless, ratios and orders of magnitude of monolayer calibration coefficients may serve to give a hint for new calibration attempts or calibrations for similar molecules.

Since desorption signal integral is directly proportional to deposition(dose) signal integral (sect. 2.1.6 d), it is possible to identify the dose integral equivalent to a monolayer surface coverage. A fraction or multiplicity of that integral is used than to deposit any sub-monolayer or multilayer film of the adsorbate. Moreover, that calibration may be reused to estimate to an order of magnitude the monolayer deposition integral of similar molecules.

2.2.3 Desorption data modeling and analysis

GNU Octave software package is chosen to model and perform the analysis of the desorption curves. Octave is a powerful Matlab-compatible, open-source package for manipulating the numerical data. It contains a comprehensive set of mathematical functions and has advanced interactive plotting capabilities. Moreover, Octave package is very mature with more than 20 years of history. That guarantees that once written, the code could be used and reused without the need to be adopted to new versions of the interpreter software[14].

The implementation of LSODE [15] solver is used to solve the Polanyi-Wigner equation (2.8).

A function (see Appendix B) to model desorption spectra with constant parameters was developed, inspired by the examples from the article by X. Zhao et al [16]. That model function comprises zero-order desorption for multi-layer desorption ($n = 0$ if coverage parameter $\theta_i > 1$) and first-order desorption for sub-monolayer coverage values. It is suitable to model a distribution of adsorption energies with initial energy E_{a0} and step dE . In this case a vector of initial coverages θ_{0i} is supplied instead of a single initial coverage θ_0 .

A comprehensive TPD data analysis and modeling toolkit is developed implementing systematic data treatment procedure according to the method described later in the section 2.3.

2.3 Desorption data analysis: case study of CH_3OH

2.3.1 Coverage calibration

To identify a monolayer coverage of methanol on graphite, a series of desorption experiments was performed with decreasing deposition integrals.

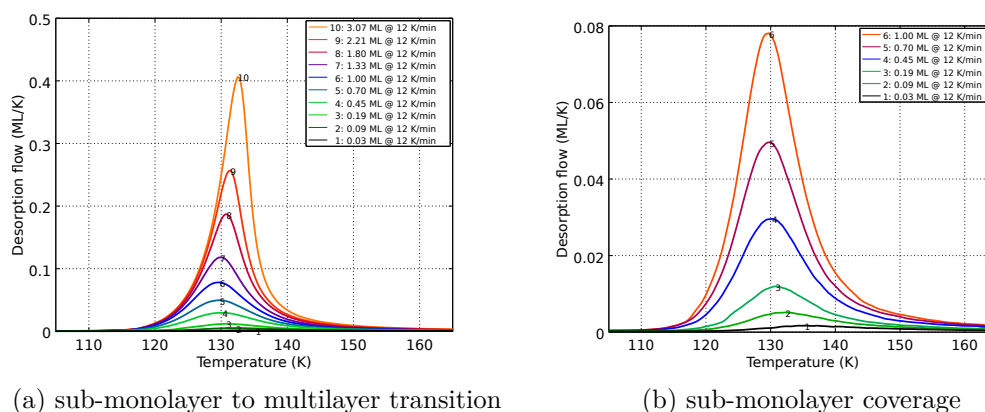


Figure 2.19 – CH_3OH on HOPG surface, deposited at 90K, heating rate 12K/min

The Fig. 2.19 shows thermal desorption curves of CH_3OH from HOPG surface, performed with a heating rate of 12K/min, for several initial methanol exposures at 90K.

Two regimes may be identified from the set of curves: For higher exposures, TPD curves are identical in the low temperature range ($\approx 110-125K$), while the maximum of the curves shifts to lower temperature with decreasing exposure. At high coverage (Fig. 2.19a), all the desorption curves share a common leading edge. This behaviour is the signature of a desorption following a zero order kinetics. For lower exposures (magnified on Fig. 2.19b), the behaviour is different: the maximum of curves is around 130K and does not shift with coverage. Low temperature parts of the curves do not overlap neither. Such behaviour is typical of higher order kinetics.

These two regimes correspond to two different kinetics of desorption, each being associated with the desorption of a multilayer of CH_3OH ($>1ML$) and with the desorption of (sub)monolayer of CH_3OH ($<1ML$) respectively. This is in contrast with the desorption kinetics of methanol on graphene consistent with zero-order desorption [17], and to the fractional-order desorption kinetics reported for desorption on HOPG [18].

The transition between the zero and the higher order desorption gives the exposure associated to a monolayer ML of CH_3OH adsorbed on HOPG. Deposition and desorption signal integrals of the monolayer are found to be $6,2 \cdot 10^{-9} A \cdot s$ and $3,4 \cdot 10^{-8} A \cdot s$ respectively. It should be noted that those calibration values are system-dependant and not directly transferable to any other experimental setup.

The precision of such monolayer coverage estimation, being hard to evaluate, is nevertheless sufficient for our purposes:

Multilayer adsorption energy is not influenced by the surface coverage for films thicker than $\approx 20ML$

For sub-monolayer regime and the case of the first-order desorption the exact initial coverage is not important neither. Indeed, monolayer calibration coefficient would stand in both left and right terms of equation (2.8) and thus may be neglected in calculations.

2.3.2 Adsorption energy in multilayer regime

In the multilayer regime, the interaction energy that drives the desorption kinetics is the one associated to CH_3OH adsorption on the subsequent layer of CH_3OH .

From the multilayer desorption curves, this energy can be derived by solving the Polanyi-Wigner equation (2.8) at the zero order($n=0$).

$$\Phi(T) = -\frac{d\theta}{dT} = \frac{\nu}{\beta}\theta^{(n=0)}e^{-\frac{E_a}{k_bT}}$$

The adsorption energy E_a together with the pre-exponential factor ν are then extracted from plotting $\ln(\Phi_{des})$ against $1/T$ (2.9).

$$\ln(\Phi(T)) = \ln\left(\frac{\nu}{\beta}\right) - \frac{E_a}{k_bT} \quad (2.9)$$

Figure 2.20a presents the TPD curve obtained from a thick (65ML) multilayer film of CH_3OH deposited onto graphite at 90 K. The corresponding plot of $\ln(\Phi(T))$ as a function of $1/T$ is shown on the figure 2.20b. The linear behaviour observed confirms that the zero order kinetics approximation fits well the obtained experimental data.

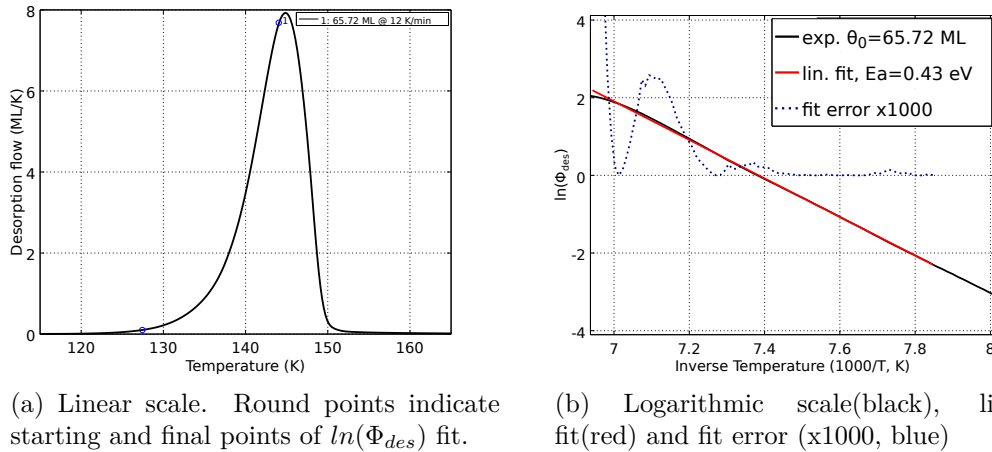


Figure 2.20 – 65 ML of CH_3OH on HOPG surface, deposited at 90K, heating rate 12K/min. Adsorption energy fit.

However, it has to be noted that other studies [18] have considered a fractional order process (between 0 and 1) in order to better reproduce the experimental data for multilayer methanol ices. At low multilayer coverage, the kinetics order has been shown to vary with the initial coverage, and tends to zero at high coverage.

The justification given by the authors is that strong hydrogen bonding in between methanol molecules impact the desorption probabilities. The reason why the order

evolves with the initial coverage may also be due to the increasing contribution of the monolayer desorption in the multilayer signal.

In our case, we did not find any strong evidence of a partial kinetics order, which may be due to the fact that we have studied thick CH_3OH ice for the multilayer adsorption energy determination.

In addition, a similar zero order kinetics has also been recently reported[17] for desorption of the multilayer film of methanol condensed on the Pt-supported graphene.

From a linear fit of the plot in fig. 2.20b, we find a value of 0.43eV for the adsorption energy and $5.0 \cdot 10^{14}\text{s}^{-1}$ for the pre-exponential factor. These values are in a good agreement with previous results [17–19] which all gave adsorption energies for the multilayer, in the high coverage regime, between 0.38 and 0.44 eV.

Bolina et al. also reported the existence of a higher temperature desorption peak, attributed by them to the desorption of a crystalline phase of condensed methanol. Although we have performed our experiments in comparable conditions (ice thickness, heating rates), we do not see any evidence of this contribution in our case. Indeed, other studies performed by Smith et al. shows that for heating rate slower than 1 K/s the whole methanol ice should already be totally crystalline at 120K, that is about 5K before the onset of the observed desorption signal.

The multilayer desorption should therefore only be associated with the crystalline methanol, and no second higher temperature peak should be observed. As this peak has been observed only for thick CH_3OH films, i.e. in conditions where the exposure was important, it may be concluded that it originated from outgasing of another cold part of the experiment during the warming up of the sample (see sect. 2.1.7 b).

2.3.3 Adsorption energy in sub-monolayer regime

Desorption in the submonolayer regime is a priori dominated by the interaction energy between the CH_3OH molecules and the graphite surface. However, determining this energy is much more complex than in the case of the multilayer ice desorption.

Indeed, a zero order kinetics cannot be used to reproduce the experimental data, since less than one layer is adsorbed on the substrate. The desorption flux becomes then dependent on the amount of adsorbed molecules at a given temperature. The Polanyi-Wigner equation becomes:

$$\Phi(T) = -\frac{d\theta}{dT} = \frac{\nu}{\beta} \theta^{(n)} e^{-\frac{E_a}{k_b T}}$$

where n is the kinetic order of the desorption, and E_a the adsorption energy between CH_3OH and the graphite surface. Three unknown parameters have thus to be determined from one given equation.

In some cases, the experimental data are fitted with n , E_a and ν taken as free parameters. Many other studies consider the first order desorption kinetics ($n=1$). As a consequence lateral interactions or inhomogeneities effects are neglected, but at the same time such an approach limits the number of free parameters of the model, making it easier to perform the fit. In this case, the prefactor ν is usually arbitrary taken as $10^{12} - 10^{13}\text{s}^{-1}$ (e.g. [11, 20]), or estimated from an important set of TPD curves with different initial coverages (e.g. [10]).

Here, a method to determine both the prefactor and the adsorption energy is proposed. The first order kinetics and constant prefactor approximation are supposed.

The technique allows to determine the prefactor ν from a series of at least three desorption curves of the same ice coverage, performed at different heating rates. However, a very good reproducibility of the grown ice coverage is required to successfully employ this method. That is usually difficult to achieve with background deposition methods, especially in the low coverage regime. That is why the deposition technique described in the section 2.1.6 plays an important role.

As an illustration this method is applied to determine the adsorption energy of a (sub)monolayer coverage of CH_3OH on highly-oriented pyrolytic graphite (HOPG).

2.3.3 a Coarse estimation of E_a and ν

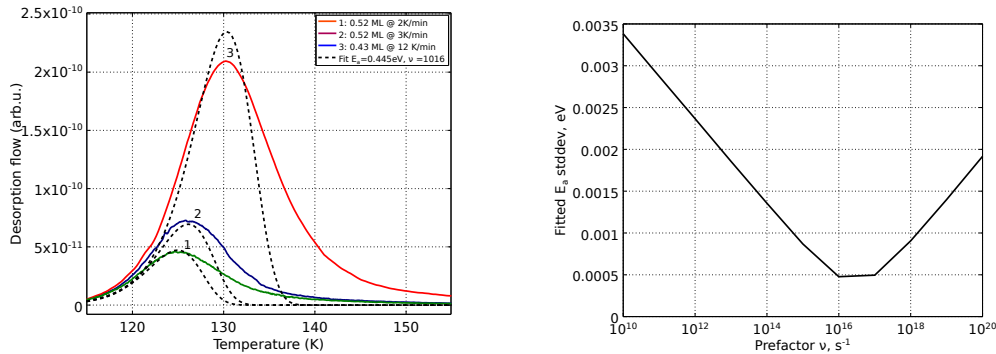
In the first order approximation, the Polanyi-Wigner equation (2.7) can be rewritten:

$$\Phi(T) = -\frac{d\theta}{dT} = \frac{\nu}{\beta}\theta(T)e^{-\frac{E_a}{k_b T}} \quad (2.10)$$

Here, the coverage at a given temperature is accessed by subtracting the integrated flux between 0 and T from the total integrated flux.

The adsorption energy can then be estimated by fitting the experimental data points by the eq. (2.10). However, an infinite number of pairs (E_a, ν) may be attributed to the same desorption curve. That means that the desorption prefactor ν should be determined independently.

In this work, ν is determined by fitting a series of TPD curves performed with the same initial coverage, but at different heating rates.



(a) Desorption curves fit with a single adsorption energy $E_0 = 0.445\text{eV}$, prefactor $\nu = 10^{16}$, heating rates $\beta=(2,3,12)$ K/min

(b) Standard deviation (2.11) of fitted adsorption energies E_a as a function of the prefactor value ν .

Figure 2.21 – 0.9 ML of CH_3OH on HOPG sample, deposited at 90K, heating rates 2, 3, 12K/min. Estimated prefactor $\nu = 10^{16}\text{s}^{-1}$.

Figure 2.21a shows three TPD curves of a submonolayer coverage (0.9ML) of CH_3OH on graphite, realized using different heating rates (2, 3 and 12 K/min). Each curve is fitted by a first order law following eq. (2.10), with different values for ν ranging in $[10^{10}, 10^{20}]\text{s}^{-1}$. Equation parameters are fitted using least-square method employing Nelder-Mead algorithm as implemented in *fminsearch* function of *Octave*.

Only the adsorption energy E_a is set as a free parameter for this fit. For each value of ν , a set of adsorption energy values is obtained, each corresponding to a different heating rate.

As the adsorption energy is not supposed to depend on the heating rate, the best value for ν is the one for which adsorption energies are found equal or their divergence is minimal. Numerically, a minimum of standard deviation σ (2.11) is determined.

$$\sigma = \sqrt{\frac{1}{(N-1)} \sum_i (E_{a(i)} - \overline{E_a})^2} \quad (2.11)$$

In our case, as shown on the figure 2.21b, for low CH_3OH coverage on HOPG we find a prefactor $\nu_{est} = 10^{16}$, that gives the adsorption energy $E_a = 0.445eV$.

This pair (E_a, ν_{est}) provides a first good estimate of the adsorption energy. However, as one can see from the fits presented in Fig. 2.21a a simple first order law still only roughly reproduces the experimental desorption curve shape. The above values are then partially correct, and need to be refined with a more accurate model. This rough estimate pair (E_a, ν_{est}) is used then as initial guess for the refined data treatment procedure, described in the following section.

2.3.3 b Fine prefactor and adsorption energies determination

The eq. (2.10) considers that all the adsorbed molecules interact with the surface with same energy E_a . This is not realistic since different adsorption sites or geometries of the adsorbed molecule are expected to result in different adsorption energies. The TPD curves experimentally obtained should then be the result of the simultaneous desorption from all the populated adsorption sites.

Introducing a distribution of the adsorption energies into the equation (2.10) allows to take this effect into account. The aim is then to derive a distribution of adsorption energies, estimate its average and width, together with an accurate value for the prefactor ν . Polanyi-Wigner equation will then take the form:

$$\Phi(T) = \sum_i \Phi_i(T) = \sum_i -\frac{d\theta_i}{dT} = \frac{1}{\beta} \sum_i \nu_i \theta_i(T) e^{-\frac{E_{ai}}{k_b T}} \quad (2.12)$$

where ν_i and E_{ai} are the prefactor and the adsorption energy associated with the adsorption site i , and θ_i the fraction of the adsorbed molecule adsorbed in the site i at the temperature T . We make here the approximation that the prefactor does not vary significantly with the adsorption site, and use the prefactor obtained in the previous step. This initial value for ν correspond to an average of the prefactors ν_i , and will be further refined. Finally, we neglect the diffusion between adsorption sites with respect to the desorption during the warming up. This has for effect that the statistic weight for the occupation of each site does only depend on the initial occupation statistic and on the desorption process. In these approximations, the eq. (2.12) can be rewritten as:

$$\Phi(T) = \sum_i \Phi_i(T) = \sum_i -\frac{d\theta_i}{dT} = \frac{\nu}{\beta} \sum_i \theta_i(T) e^{-\frac{E_{ai}}{k_b T}}$$

For this model the only free parameter is the array of initial coverages θ_{i0} . Fig. 2.22 presents the fit of the experimental TPD of 1ML of CH_3OH on HOPG with a distribution of adsorption energies. One may see that the quality of the fit is improved significantly, compared to a single adsorption energy fit (Fig. 2.21a).

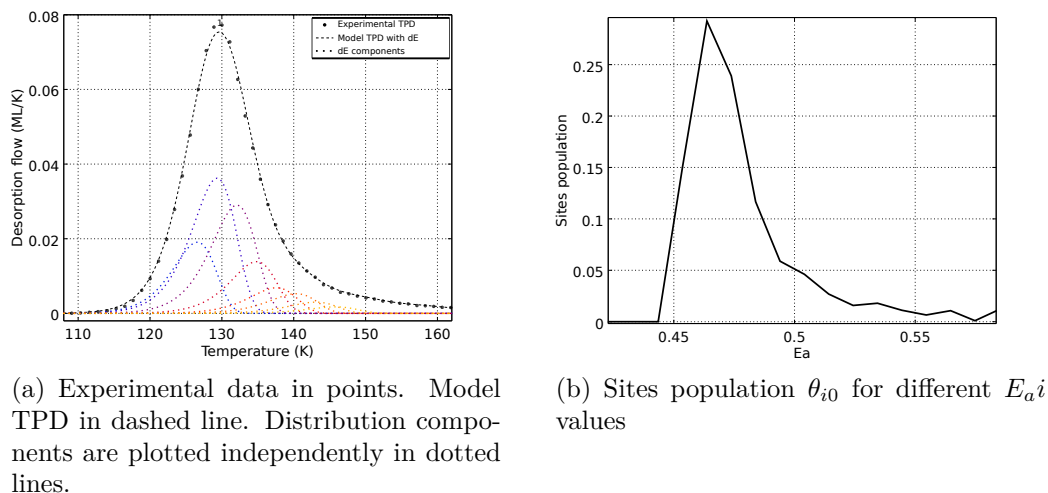


Figure 2.22 – TPD of 1ML of CH_3OH adsorbed on HOPG surface. Deposited at 90K, heating rate 12K/min. Model fit with a distribution of adsorption energies.

Energy points $E_{ai} = E_0 + i\Delta E$ are fixed such that the whole temperature range of desorption is covered. Interval ΔE between energy points is chosen such that on the desorption plot the maximum of subsequent desorption component finds itself at $0.75 \times \max(\Phi_i)$ of the amplitude of previous component. That provides a sufficiently dense array of energy points, keeping compromise between the calculations speed and the fit quality.

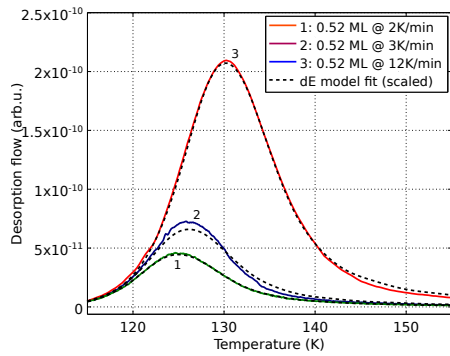
Now we have all the components to refine the prefactor value determined in the section 2.3.3 a. From the experimental desorption curve with a lowest available heating rate three energy distributions are determined using prefactor values of $0.01 \times \nu_{est}$, ν_{est} , $100 \times \nu_{est}$.

Figure 2.23a presents the same desorption curves as in Fig. 2.21a, fitted with a distribution of adsorption energies. Using a method similar to the rough prefactor estimation (sect. 2.3.3 a), initial energy point E_0 of the energy distribution is fitted as a function of prefactor value ν_i for a dense set of prefactor points over a range $[0.01\nu_{est}, \nu_{est}, 100\nu_{est}]$. Again, a minimum of standard deviations $\sigma E_0(\nu)$ (2.11) is determined, plotted on a figure 2.23b. One may note that all the minima coincide, irrespective to the energy distribution used to fit the desorption curves.

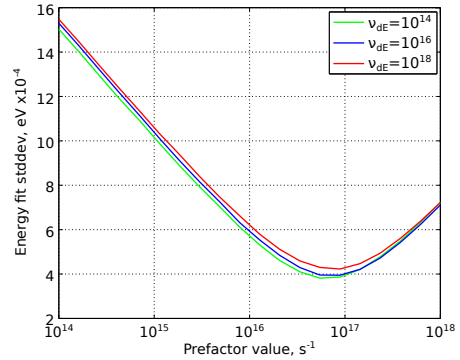
The value of the prefactor determined is $\nu_{best} = 7.7(\pm 3) \times 10^{16} s^{-1}$. The width and shape of the minima on a figure 2.23b gives the indication on the accuracy of the determined prefactor value.

2.3.3 c Adsorption energies of CH_3OH monolayer on graphite

Once the prefactor is determined, the adsorption energy distributions for sub-monolayer coverages may be accessed.

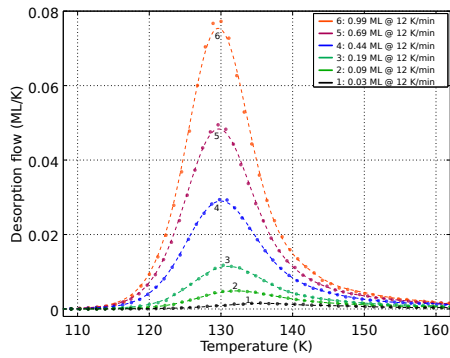


(a) Desorption curves fit with a single adsorption energy $E_0 = 0.445 eV$, prefactor $\nu = 10^{16}$, heating rates $\beta = (2, 3, 12)$ K/min

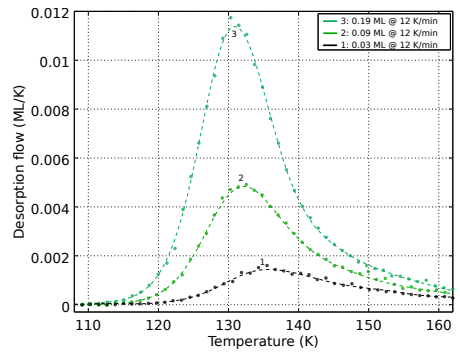


(b) Standard deviation (2.11) of fitted adsorption energies E_0 as a function of the prefactor value ν .

Figure 2.23 – 0.9 ML of CH_3OH on HOPG sample, deposited at 90K, heating rates 2, 3, 12K/min. Estimated prefactor $\nu = 10^{16} s^{-1}$.

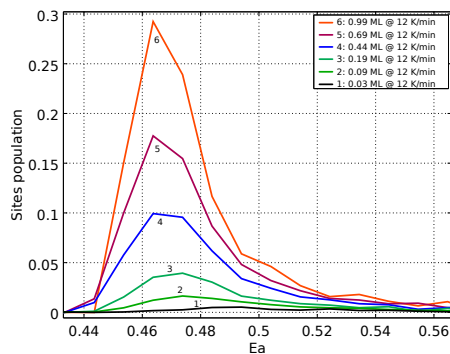


(a) Desorption curves fit with a distribution of adsorption energies

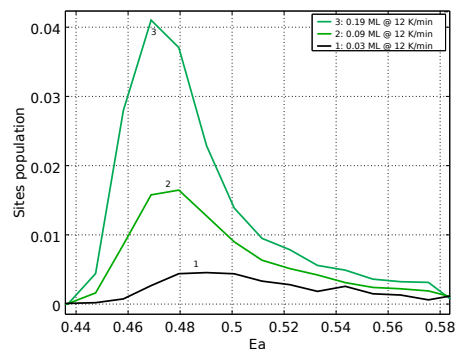


(b) Zoom on coverages below 0.2 ML

Figure 2.24 – Various coverages of CH_3OH on HOPG surface, deposited at 90K, heating rate 12K/min. Every fifth point of the experimental data is plotted in points, corresponding fitted models are plotted in dashed lines.



(a) Coverages from 0.03 to 1ML



(b) Zoom on coverages below 0.2 ML

Figure 2.25 – Fitted initial coverages θ_0 for adsorption energy distribution.

Fig. 2.24 shows the TPD curves of several submonolayer coverages, ranging from 0.03 to 1 ML, of methanol deposited at 90 K on graphite. Fitted curves, obtained following our method, are superimposed. Corresponding adsorption energy distributions are presented on the figure 2.25. It may be noted that fitting the experimental data with the energy distribution gives a very good match in a whole coverages and temperatures range. That procedure may be considered as an analogue of Fourier transform, allowing to switch from desorption signal against temperature to initial coverage against adsorption energy scales. From the adsorption energy distributions, one can extract the most probable adsorption energy value E_a together with the variation of adsorption energies ΔE_a taken as the width of the distribution.

θ_0 , ML	\overline{E}_a , eV	$\Delta E_a^{(FWHM)}$, eV
0.99	0.467	0.029
0.69	0.467	0.031
0.44	0.469	0.035
0.19	0.473	0.035
0.09	0.478	0.046
0.03	0.498	0.116

Table 2.2 – Weighted average adsorption energies and energy distribution widths (FWHM) for CH_3OH adsorption on graphite

The results are summarized in Table 2.2. Broadening of the energy distribution is observed at low coverage, due to increasing contribution of high-energy defect sites. For initial coverages from 0.2 to 1 ML the adsorption energy is found to be weakly sensitive to the initial methanol coverage, with an average value of $\approx 0.47eV$.

The uncertainty on adsorption energies caused by the limited prefactor accuracy is of $\pm 0.02eV$ for prefactor variation of an order of magnitude, that is less than the width of the distribution found for low coverages and comparable to the distribution width at the near-ML coverage.

The determined value of the adsorption energy is in a good agreement with the one extracted by Smith et al. for the monolayer CH_3OH adsorption on graphene (0.47eV), as well as by Bolina et al. for coverages close to the monolayer. In the latter study, it was found that a monolayer adsorption energy varies from 0.34 eV to almost 0.50 eV, increasing with the CH_3OH coverage. Such an important variation of the adsorption energy was explained by the ability of CH_3OH to perform strong hydrogen bonding with itself, thus increasing the adsorption energy with coverage due to the lateral interactions. A similar finding is observed theoretically: Schröder[21] has recently studied methanol adsorption on graphene planes using DFT-based calculations and found that the adsorption energy of methanol interacting with 4 neighbouring molecules is already multiplied by 1.75 as compared to the isolated molecule. In our case, we observe no evidence of such an increase of the adsorption energy with the increasing coverage. The mean value that we measure at low coverage already corresponds to the desorption of highly coordinated CH_3OH molecules. Therefore, we suggest that at 90 K the first layer of methanol organizes as hydrogen-bonded islands on the HOPG surface, even at coverages as low as 0.1 ML. Similar hydrogen-

bonded structures at low coverage have already been observed in the case of H_2O adsorption, which form hydrogen-bonded chains along step-edges on Pt surfaces at very low coverage [22, 23]. In our case, steps and defects on graphite surface may similarly explain the island-like organization of the CH_3OH at very low coverage.

Discrepancies exist in literature concerning the kinetic order to be considered for the methanol desorption from graphite. On the one hand, Smith et al. clearly showed that a zero order kinetics dominates the monolayer desorption of CH_3OH from a perfect surface of Pt-supported graphene. This is explained by the existence of a 2 dimensional condensed island-gas equilibrium on the surface during the warming-up process, constraining the desorption flux as the non-evolving partial pressure of the gaseous phase. On the other hand, Bolina et al. have used a fractional 1.23 kinetics order to extract the adsorption energies of methanol on graphite, presumably because of an aggregated structure of the methanol molecules. Such differences can be reasonably explained by the different morphology of the support surfaces, but also by different homogeneities of the CH_3OH layer on the substrate. Indeed, defects, but also the deposition method (effusive beam, background deposition, etc.), can alter the resulting ice, and result in more or less structured or aggregated molecular film on the sample. In our case, as explained above, we believe our first layer to consist in CH_3OH islands on the HOPG substrate. From the excellent agreement we obtain between the experimental data set and the simulated curves we can conclude that a first-order kinetics approximation remains valid for such strongly interacting molecular organization of the monolayer, with no need of using fractional kinetic order, whose physical meaning is less obvious. In our method, the inhomogeneities between edge and central molecules in the hydrogen-bonded islands are taken into account in the adsorption energy distribution, each configuration participating to the overall desorption signal.

2.3.4 Summary

Adsorption of the methanol (CH_3OH) on HOPG was studied. Effective monolayer calibrations for SPICES setup are found to be $6,2 \cdot 10^{-9} A \cdot s$ and $3,4 \cdot 10^{-8} A \cdot s$ for deposition and desorption signal integrals respectively (sect. 2.3.1) No separate monolayer peak is observed, that means that sub-monolayer and multilayer adsorption energies are close.

Multilayer adsorption energy is found to be $0,43 eV$ (sect. 2.3.2), sub-monolayer adsorption energy of $\approx 0,47 eV$ for close to monolayer and $0,50 eV$ for coverages below 0.1ML are found (sect. 2.3.3 c). Adsorption energy values determined here are in a good agreement with previous studies [17, 18].

The prefactor value of $\nu = 7,7(\pm 3) \times 10^{16} s^{-1}$ is found (sect. 2.3.3 b) for sub-monolayer coverages using a variable heating rate approach and a protocol similar to the one used by Koch et al. [13]. The main difference between the method developed here and the one proposed by Koch et al. is the minimized function.

A systematic experiment protocol is established. All data treatment procedures are implemented in a software toolkit developed using Octave [14] language.

References

- [1] A. G. G. M. Tielens. “The molecular universe”. In: *Reviews of Modern Physics* 85.3 (2013), pp. 1021–1081.
- [2] Howard O. McMahon and William E. Gifford. “Closed-cycle helium refrigeration”. In: *Solid-State Electronics* 1.4 (1960), pp. 273–278.
- [3] A. T. A. M. de Waele. “Basic Operation of Cryocoolers and Related Thermal Machines”. en. In: *Journal of Low Temperature Physics* 164.5-6 (June 2011), pp. 179–236.
- [4] Ray Radebaugh. “Cryocoolers: the state of the art and recent developments”. en. In: *Journal of Physics: Condensed Matter* 21.16 (Apr. 2009), p. 164219.
- [5] E.S. Drexler N.J. Simon and R.P. Reed. *Properties of Copper and Copper Alloys at Cryogenic Temperatures*. NIST Monograph no. 177. U.S. Dept. of Commerce, National Institute of Standards and Technology, 1992.
- [6] W. Hwang, Y.-K. Kim, and M. E. Rudd. “New model for electron-impact ionization cross sections of molecules”. In: *The Journal of Chemical Physics* 104.8 (Feb. 1996), pp. 2956–2966.
- [7] P. J. Linstrom and W. G. Mallard, eds. *NIST Chemistry WebBook, NIST Standard Reference Database Number 69*. Gaithersburg MD, 20899: National Institute of Standards and Technology, June 2005.
- [8] P.H. Dawson. *Quadrupole Mass Spectrometry and Its Applications*. Elsevier Science, 2013.
- [9] Jiao He and Gianfranco Vidali. “Application of a diffusion–desorption rate equation model in astrochemistry”. en. In: *Faraday Discussions* 168.0 (Aug. 2014), pp. 517–532.
- [10] Z. Dohnálek et al. “Physisorption of CO on the MgO(100) Surface†”. In: *The Journal of Physical Chemistry B* 105.18 (2001), pp. 3747–3751.
- [11] A. M. de Jong and J. W. Niemantsverdriet. “Thermal desorption analysis: Comparative test of ten commonly applied procedures”. In: *Surface Science* 233.3 (1990), pp. 355–365.
- [12] E. Habenschaden and J. Küppers. “Evaluation of flash desorption spectra”. In: *Surface Science* 138.1 (1984), pp. L147–L150.
- [13] K. Koch et al. “A New Method of Analysing Temperature-Programmed Desorption (TPD) Profiles Using an Extended Integral Equation”. In: *Journal of Catalysis* 172.1 (1997), pp. 187–193.
- [14] John W. Eaton. “GNU Octave and reproducible research”. In: *Journal of Process Control*. Ken Muske Special Issue 22.8 (2012), pp. 1433–1438.
- [15] Krishnan Radhakrishnan and Alan C. Hindmarsh. *Description and use of LSODE, the Livermore Solver for Ordinary Differential Equations*. Tech. rep. Dec. 1993.
- [16] X. Zhao et al. “Thermal desorption of hydrogen from carbon nanosheets”. In: *The Journal of Chemical Physics* 124.19 (May 2006), p. 194704.

- [17] R. Scott Smith, Jesper Matthiesen, and Bruce D. Kay. “Desorption Kinetics of Methanol, Ethanol, and Water from Graphene”. In: *The Journal of Physical Chemistry A* 118.37 (2014), pp. 8242–8250.
- [18] A. S. Bolina, A. J. Wolff, and W. A. Brown. “Reflection absorption infrared spectroscopy and temperature programmed desorption investigations of the interaction of methanol with a graphite surface”. In: *The Journal of Chemical Physics* 122.4 (Jan. 2005), p. 044713.
- [19] R. Martín-Doménech et al. “Thermal desorption of circumstellar and cometary ice analogs”. In: *Astronomy & Astrophysics* 564 (Apr. 2014), A8.
- [20] J. A. Noble et al. “Thermal desorption characteristics of CO, O₂ and CO₂ on non-porous water, crystalline water and silicate surfaces at submonolayer and multilayer coverages”. en. In: *Monthly Notices of the Royal Astronomical Society* 421.1 (Mar. 2012), pp. 768–779.
- [21] Elsebeth Schröder. “Methanol Adsorption on Graphene”. en. In: *Journal of Nanomaterials* 2013 (Sept. 2013), e871706.
- [22] K Jacobi et al. “From monomers to ice – new vibrational characteristics of H₂O adsorbed on Pt(111)”. In: *Surface Science* 472.1–2 (2001), pp. 9–20.
- [23] Mihail L. Grecea et al. “The Interaction of Water with the Pt(533) Surface”. In: *The Journal of Physical Chemistry B* 108.33 (2004), pp. 12575–12582.

Chapter 3

Theoretical approach

Another approach permits to study the adsorption in systems of astrophysical interest: the use of computational chemistry methods. Besides the possibility to determine the adsorption energies, it allows to get some insight into the behaviour of the astrochemically relevant surface-adsorbate systems at the atomic level.

First section (3.1) presents a brief introduction of the chosen method, Density Functional Theory (DFT), and its necessary basics. Only the main concepts and ideas behind the DFT methodology are given (for more details please refer to books by Sholl et al.[1] and Koch et al.[2] that give a practical description).

Different approaches to study adsorbate-surface interactions are presented in the second part (sect. 3.2).

Some practical issues as accuracy and performance are discussed in the third part (sect. 3.3) on the example of methanol adsorption on graphite.

Methods to analyze interactions, such as charge density analysis and electron localization function analysis are shown in the last part (sect. 3.4).

3.1 First principles approach

First-principles approaches start from the fundamental physics concepts to describe the model systems and deduce its properties.

In the context of quantum chemistry, solving the time-independent Schrödinger equation (3.1) allows to determine the physical properties of a quantum system.

$$E_i \Psi_i = \hat{H} \Psi_i \quad (3.1)$$

Here, \hat{H} is the Hamiltonian describing the system, Ψ_i wavefunctions (eigenfunctions) and E_i the corresponding state energies (eigenvalues).

3.1.1 General introduction on DFT

Density Functional Theory (DFT) is one of the methods of quantum chemistry, modelling the electrons of a quantum-mechanical system with a density $\rho(\vec{r})$. It is stated that all the observable properties of the system in a ground state are determined by that density $\rho(\vec{r})$, that depends on the potential $v(\vec{r})$.

DFT bases itself on a set of approximations and methods:

3.1.1 a Born-Oppenheimer approximation

Born-Oppenheimer approximation is currently used in most of quantum mechanic and quantum chemistry calculations. It states that the motion of electrons and nuclei may be considered independently and the wavefunction of the system decoupled into nuclear and electronic wavefunction.

$$\Psi_{total} = \Psi_{nuclei} \times \Psi_{electron}$$

As a consequence the problem is reduced to the motion of electrons in a fixed potential of the nuclei.

The Hamiltonian of the system becomes

$$\hat{H} = \hat{T} + \hat{V} + \hat{V}_H + \hat{V}_{XC}$$

Where \hat{T} is the kinetic energy of electrons, \hat{V} is the interaction potential between electron and nuclei, \hat{V}_H Hartree potential of the electron-electron coulomb repulsion, \hat{V}_{XC} electron-electron exchange and correlation potential.

3.1.1 b Hohenberg-Kohn theorems

The DFT is based on two theorems of Hohenberg and Kohn [3]:

First theorem states that the properties of the system, including energy states, potentials and wave-functions are uniquely determined by the electron density $\rho(\vec{r})$.

Second theorem states that the electron density $\rho_0(\vec{r})$ for which the energy E is minimal is the true ground-state electron density.

3.1.1 c Kohn-Sham equations

A solution to determine the homogeneous electron density has been proposed by Kohn and Sham[4].

The physical system is replaced by a fictitious one consisting of the non-interacting electrons moving in effective potentials. A set of one-electron equations is solved:

$$\left[-\frac{\hbar^2}{2m} \nabla^2 + V(r) + V_H(r) + V_{XC}(r) \right] \psi_i(r) = \epsilon_i \psi_i(r) \quad (3.2)$$

here the first term is the kinetic energy of the electron, V the potential energy of interaction with nuclei, $V_H(r)$ the electron-electron repulsion potential, $V_{XC}(r)$ exchange-correlation potential.

Electron density $\rho(r)$ is determined as

$$\rho(r) = \sum_{i=1}^N \psi_i^*(r) \psi_i(r) \quad (3.3)$$

where N is the number of electrons and ψ_i are one-electron wavefunctions, solving the equation (3.2).

The potentials $V(r)$, $V_H(r)$ are known functions of the electron density, while the exact equation for $V_{XC}(r)$ as a function of density is unknown. Finding a good approximation of the exchange-correlation functional $V_{XC}(r)$ is one of the tasks currently solved by the developers of the DFT

To converge to a solution, an iterative approach is proposed by Kohn and Sham. Potentials are obtained from a trial electron density, then the equations (3.2) are solved to obtain the wavefunctions. Finally, a new electron density is constructed according to the equation (3.3), and the calculations cycle is repeated.

3.1.2 Exchange-correlation functionals

As mentioned in the previous section, one of the problems of the Density Functional Theory is the choice of the exchange-correlation functional E_{xc} . Many classes of functionals E_{xc} are available, among them

3.1.2 a Local density approximation (LDA)

For the cases where electron density $\rho(\vec{r})$ varies slowly, i.e. in bulk metals or metallic compounds, Local Density Approximation (LDA) functionals are recommended and give a good approximation of chemical properties. LDA functionals take into account only the density at the point \vec{r} to determine E_{xc} : $E_{xc}(\vec{r}) = \hat{E}_{xc}(\rho(r))$

3.1.2 b Generalized Gradient Approximation (GGA)

For systems with important density gradients, LDA functionals often fail to predict properties accurately. For example, geometries and ground-state energies of highly-polarized molecules are better determined using Generalized Gradient Approximation (GGA) functionals. In GGA the E_{xc} is a function of both density $\rho(\vec{r})$ and density gradient $\Delta\rho(\vec{r})$. $E_{xc}(\vec{r}) = \hat{E}_{xc}(\rho(r), \Delta\rho(\vec{r}))$

In this work, a GGA type functional developed by Perdew et al.[5] is used (PBE). It gives good results for geometries and atomization energies and reproduces well the hydrogen bonds

Other classes of functionals exist, but they are often tuned to solve particular problems.

3.1.3 Van der Waals interactions

In the systems studied in this thesis, adsorption energy is, to a big extent, due to the Van der Waals type of interaction, i.e. electrostatic interaction between dipoles, both permanent and induced ones.

Traditional DFT functionals fail to describe Van der Waals interactions correctly, in particular the ones between induced dipoles (London dispersion force). Different approaches including specially crafted functionals [6–8] and semi-empirical [9] corrections were proposed.

In this work a semi-empirical approach DFT-D2 proposed by Grimme[9] is employed.

This is a computationally cheap and reasonably accurate [10] method to take the Van der Waals interactions into account. A dispersion term is added to the total DFT

energy:

$$E_{disp} = -s_6 \sum_{i \neq j}^{N_{at}} \frac{C_6^{ij}}{R_{ij}^6} f_{dmp}(R_{ij})$$

Here, N_{at} is the number of atoms in the system, $C_6^{ij} = \sqrt{C_6^i C_6^j}$ denotes the dispersion coefficient for atom pair ij , s_6 is a global scaling factor that only depends on the density functional used, and R_{ij} is an inter-atomic distance. In order to avoid near-singularities for small R , a damping function f_{dmp} is used. Coefficients C_6^i are determined as an empirical function of calculated atom ionization potentials and polarizabilities.

3.2 Cluster versus periodic approaches

Two main approaches are possible to study interactions of adsorbates and grain surfaces. The first one is to represent the grain as a cluster of atoms, with adsorbate attached. The other approach is to study the adsorption on periodic slab surface.

Representing a grain as a cluster seems to be a natural approach, but it requires relatively big system size to avoid the effect of the edges on the adsorption energy. For example, for CH_4 adsorption on Polycyclic Aromatic Hydrocarbons (PAH) and graphene the experimental adsorption energy on graphene is reproduced only for Circumcoronene ($C_{54}H_{18}$) molecule [11].

Modelling the grain surface with a periodic slab is another approach. It allows to avoid the edge effects of the cluster while using a relatively small (10-100) number of atoms. The use of plane wave basis sets to describe the electron density in periodic systems allows to eliminate the main problem of cluster models, the basis set superposition error.

On the other hand the use of periodic approach has a limitation: modeling amorphous systems becomes difficult, since the periodicity and thus a long-range order is imposed by the model.

In this work the periodic slab approach to model the surface is chosen. It will be described in detail in the following chapter, along with practical details on adsorption energy calculation.

3.3 Determining adsorption energetics

In this work all calculations are performed using Vienna Ab initio Simulation Package (VASP) code. VASP is a periodic DFT code, using a plane wave basis set to represent electron wavefunctions [12].

To reduce the number of plane waves, the atoms core electrons are replaced by pseudopotentials, calculated using projector augmented wave (PAW) method [13, 14].

As mentioned earlier, all calculations are performed using PBE Generalized Gradient Approximation (GGA) functional (sect. 3.1.2 b), [5]. Van der Waals interactions are taken into account by employing the Grimme correction (sect. 3.1.3), [9].

Atoms are relaxed to the ground state using the conjugate-gradient algorithm. Minimum force per atom criteria is used to interrupt the geometry optimization, and

not the minimum total energy of the system since the potential energy surface is flat for the adsorption process.

To manipulate structures, Atomic Simulation Environment (ASE) [15, 16] Python-based software toolkit is used.

3.3.1 Periodic system

Adsorption on the surface is studied in the slab system (fig. 3.1). Since the calculations are essentially periodic in three dimensions (x,y,z), it is necessary to add a large gap of vacuum in the z direction (orthogonal to the surface plane) to model the surface.

For the case of molecular adsorption, orthogonal primitive cells were routinely used in this work. The surface is represented by 1 to 3 layers of bulk material, depending on the system under study (see e.g. sect. 3.3.5 d for benchmark) To avoid the interaction of an adsorbate with the periodic image of bottom layers in z direction, a large amount (at least 10-15Å, sect. 3.3.5 c, sect. 4.3.3) of vacuum is added. Convergence of adsorption energy against adsorbate-adsorbate distance (unit cell dimensions in x-y plane) should also be verified if one seeks to model the adsorption of an isolated atom or molecule. As an example, convergence of methanol adsorbed on graphite is tested here in the chapter 3.3.5 c.

To determine the adsorption energy, total energies of three systems need to be calculated: slab with adsorbate $E_{slab+ads}$, slab alone E_{slab} and the adsorbate E_{ads} alone in the cell. The adsorption energy E_a is then determined as

$$E_a = E_{slab+ads} - (E_{slab} + E_{ads})$$

Within this convention, negative energies E_a stand for an exothermic process.

3.3.2 Bulk geometry optimization

When choosing and preparing a surface model, one first needs to determine the bulk geometry.

For every bulk system a cohesion energy E_{coh} may be determined as a difference between the bulk system total energy and n -times the total energy of bulk element E_{elem} (atom or molecule) in the vacuum:

$$E_{coh} = E_{bulk} - nE_{elem} \quad (3.4)$$

where n is the number of atoms or molecules constituting the bulk.

Among many geometries possible, only stable ones (having energies in a (local) minimum) will form the solid systems, and natural abundance of those structures depends on the cohesion energy (3.4) strength.

Even if the stable bulk geometry is known from the experiment or previous calculations, it needs to be re-optimized since the exact equilibrium geometry strongly depends on the employed functional and calculation parameters.

3.3.3 Surface modelling

When the slab is cut from the bulk, the outermost layer of material loses the attractive interaction with what used to be the continuation of the bulk. That leads

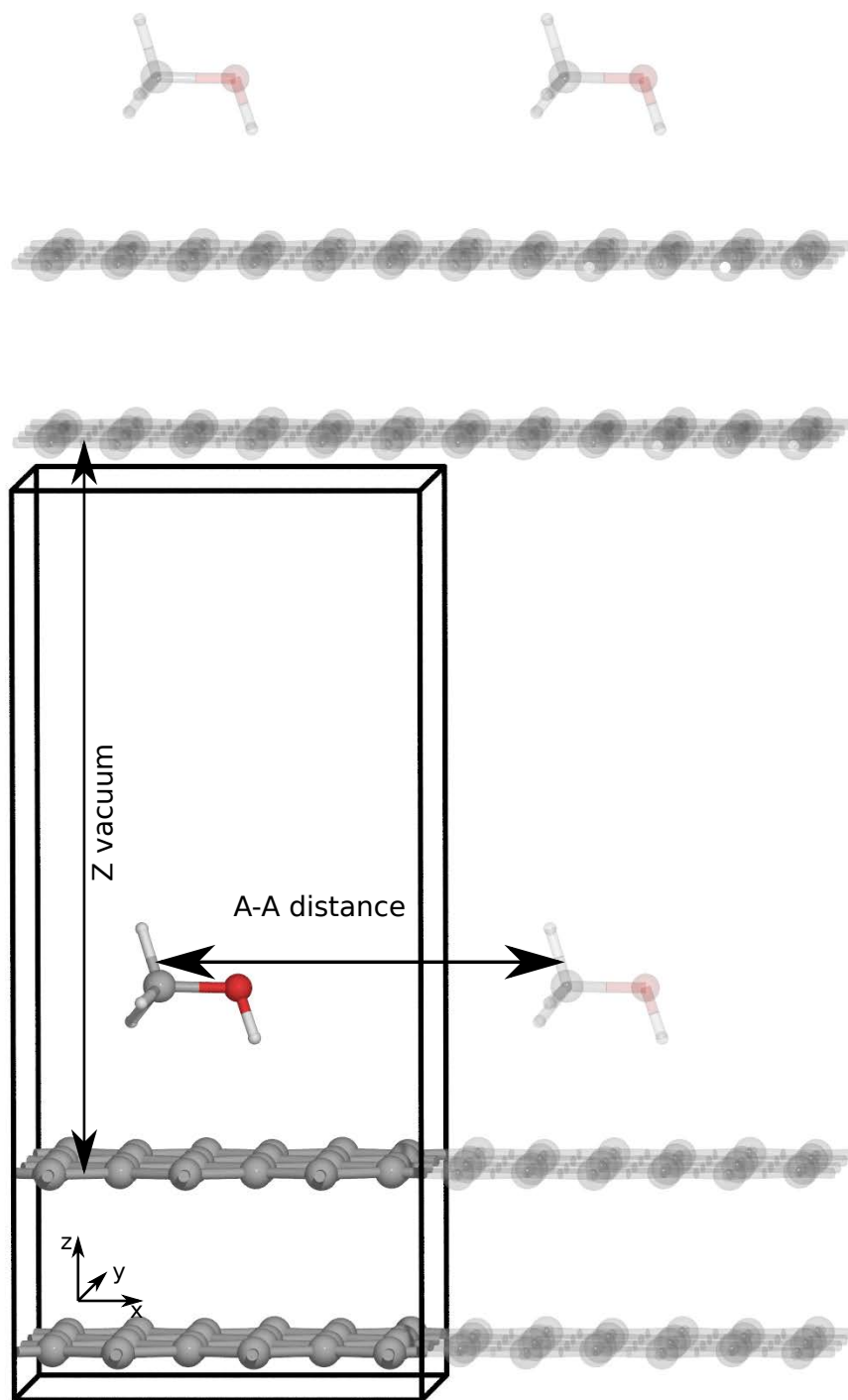


Figure 3.1 – Periodic unit cell: CH_3OH adsorption on graphite example. Unit cell in solid color, x and z direction images are transparent.

to a new equilibrium position of surface atoms, usually reducing the equilibrium interlayer distances for few topmost layers. Therefore the surface geometry needs to be re-optimized after the surface is cut from the bulk.

Essentially, for every bulk model there exists a number of ways to cut the surface according to Miller indices. But not all the possible surfaces are equivalent. Indeed, the more stable the surface is, the more it will be present in nature. On the other hand, less stable surfaces may be more active for adsorption. A measurable quantity exists to characterize the surface stability, the surface energy E_{surf} . It may be derived from calculations using the following equation:

$$E_{surf} = \frac{E_{slab} - nE_{bulk}}{2A}$$

Here, E_{slab} is the total energy of the relaxed slab system, n is the number of layers in slab, E_{bulk} is the bulk energy of a layer and A is the surface area of the slab unit cell in the surface plane. Coefficient two comes from the fact that the energy difference comprises the energies of top and bottom slab surfaces.

E_{bulk} may be derived from the bulk calculations or taken as (3.5) in the limit of a thick slab.

$$E_{bulk} = E_{slab}(n) - E_{slab}(n - 1) \quad (3.5)$$

$E_{slab}(n)$ here is the total energy of slab with n layers of material, and $E_{slab}(n - 1)$ is a slab with one layer less. Both slab energies in this case are determined with the same cell dimensions and calculation parameters. Such calculations converge quickly against the number of slab layers. For example for the case of water ices convergence at 5-6 bilayers is reported [17].

3.3.4 Adsorption sites

Quantum chemistry methods permit to identify different adsorption sites on the model surface, i.e. different local minima of adsorption energy. Various initial orientations and positions of the adsorbate should be relaxed to local energy minima to determine different classes of adsorption geometries, among them the one having lower adsorption energy is the most stable system. That means that in presence of diffusion on the surface the adsorbate is likely to occupy it.

3.3.5 Example: CH_3OH adsorption on graphite

As an example, methanol adsorption was studied on graphene and two graphite models: two-layer graphene and two-layer graphene with a defect in the topmost layer.

Apart from benchmarking the method against the known example, the interest of this study is to extend the existing study of [18] that investigates the adsorption of single methanol molecule and two-dimensional molecular clusters on the graphene surface. Hereafter, the effect of graphite substrate model and surface defects on the methanol adsorption energy is evaluated.

3.3.5 a Possible adsorption sites

For the graphene surface, three possible points of adsorption (figure 3.2a) may be considered:

- (1) on top of carbon atom
- (2) in the middle of the benzene ring
- (3) in the middle of C-C bond.

More degrees of freedom are added in case of the molecular adsorption: adsorbate orientation also plays a significant role.

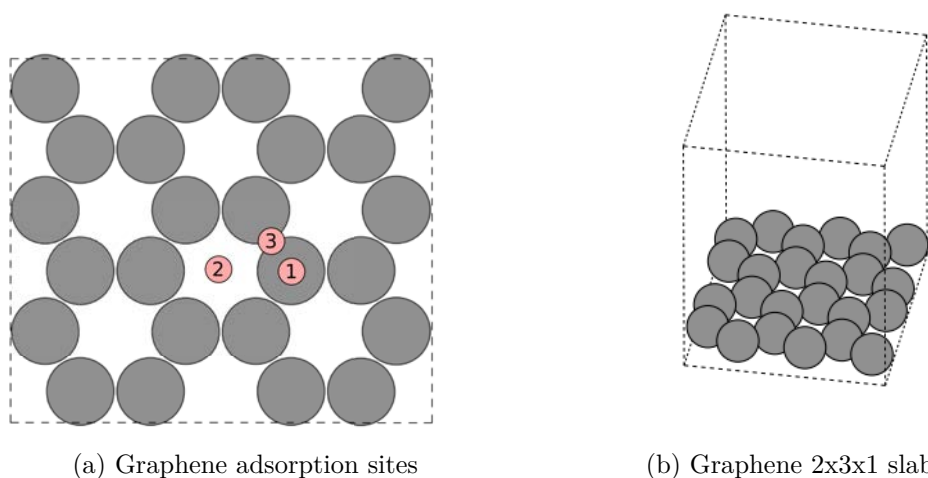


Figure 3.2 – Graphene surface model

For the case of (almost) linear molecules with CH_3 group like methanol and acetonitrile, four adsorbate orientations may be distinguished:

- vertical, CH_3 umbrella close to the surface (**L**), (e.g. fig. 3.3a)
- vertical, reversed: CH_3 umbrella away from the surface (**i**) (e.g. fig. 3.3e)
- parallel to the surface (**p**) (e.g. fig. 3.3k)

Additional degree of freedom is added due to the CH_3OH rotation around the main molecular axis.

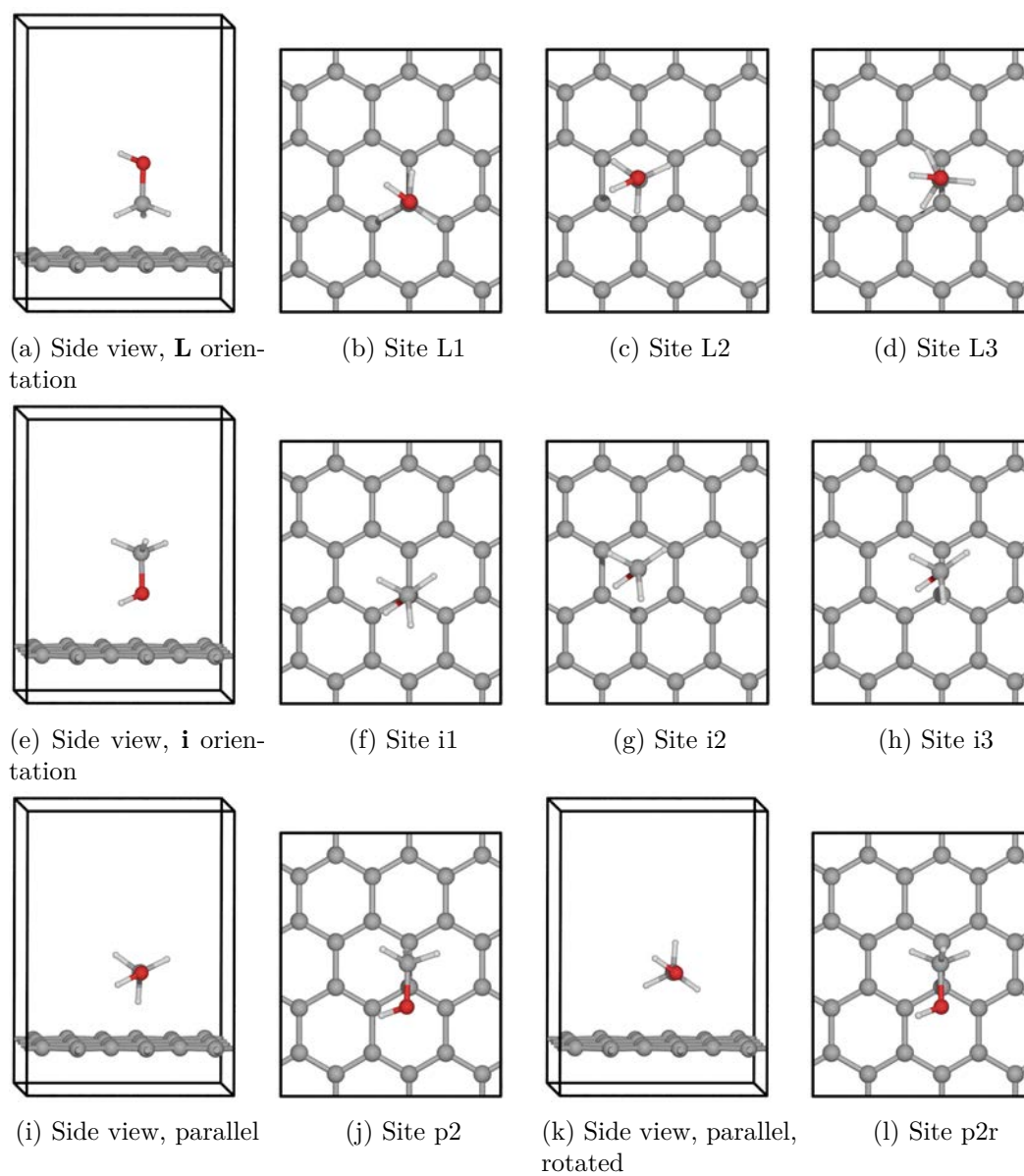


Figure 3.3 – Probing methanol adsorption sites on graphene. 2x3x1 graphene sheet, 10Å vacuum

3.3.5 b Adsorption geometry search

For the optimum geometry search, a small cell with a single graphene plane of 24 carbon atoms and 10Å of vacuum was used. Multiple initial adsorbate positions (fig. 3.3) were tested: vertical orientations with CH₃ group pointing upwards or downwards against the surface plane, with C atom above carbon, above benzene ring or above c-c bond. Several orientations parallel to the surface were also tested.

Geometry optimization of the adsorbate atoms was performed, while the graphene atoms were frozen. Adsorption energies were found to be orientation-dependent, the preferred site (fig. 3.4, $E_a=0.25$ eV) corresponding to the parallel orientation, OH pointing in the direction of one of surface carbons. Vertical orientations (**L**, fig. 3.3a-3.3d) showed adsorption energies of 0.18..0.20 eV and vertical orientations (**i**, fig. 3.3e-3.3h) were found to be unstable, relaxing to the parallel orientation.

A summary of determined adsorption energies is given in Table 3.1.

Site	E_a , eV	d^{C-O} , Å	Final orient.
L1	-0,195	4.70	vertical
L1r	-0,205	4.62	vertical
p1	-0,241	3.16	parallel
p1r	-0,214	3.19	parallel
i1	-0,249	3.22	parallel
L2	-0,185	4.71	vertical
L2r	-0,185	4.73	vertical
i2	-0,235	3.18	parallel
i2r	-0,229	3.20	parallel
L3	-0,196	4.66	vertical
L3r	-0,202	4.66	vertical
i3	-0,205	3.22	inclined

Table 3.1 – CH₃OH adsorption sites and corresponding adsorption energies on graphene plane (2x3x1 slab, 8.55x7.39x10Å cell, 10Å vacuum)

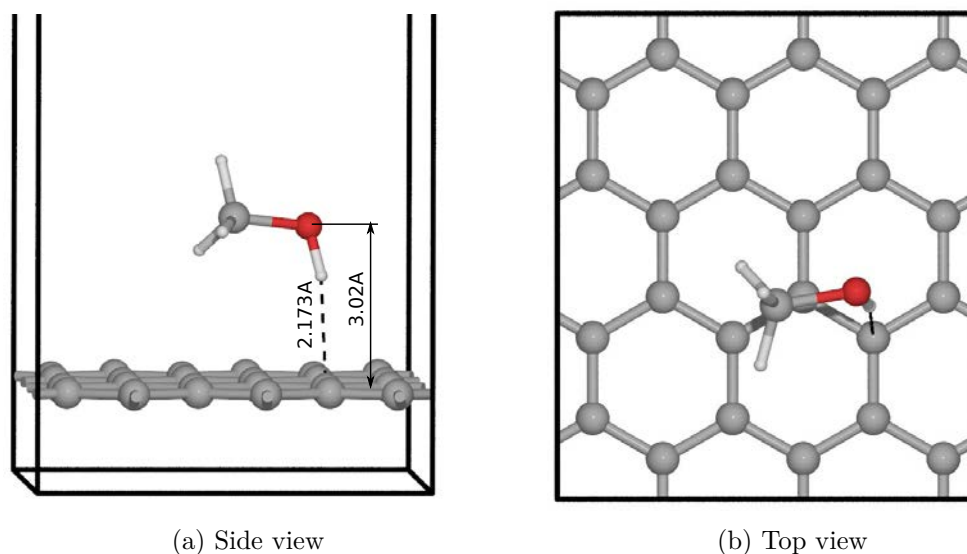


Figure 3.4 – Methanol on graphene: strongest adsorption site geometry. $2 \times 3 \times 1$ graphene sheet, $8.55 \times 7.39 \times 15 \text{ \AA}$ cell.

3.3.5 c Convergence as a function of model parameters

To determine the required cell size and model parameters for the exact adsorption energy calculation, a series of tests was carried out on the strongest CH_3OH adsorption site on graphene plane (fig. 3.4). Convergence against cell size in surface plane and vacuum size, as well as convergence against the number of slab layers was tested.

To test the convergence against the cell lateral size, a set of cells was used, each of them with different dimensions in x-y plane and 15 angstroms on vacuum size (Table 3.2).

Size, \AA	Slab index	K points*	No of carbon atoms
4,27x4,93x15	121	5x5x1	8
8,55x4,93x15	221	3x5x1	16
8,55x7,39x15	231	3x3x1	24
8,55x9,86x15	241	3x3x1	32
12,82x9,86x15	341	3x3x1	48
12,82x12,32x15	351	3x3x1	64

Table 3.2 – Cell parameters for convergence verification against the unit cell X-Y dimensions.

*enough K points is taken to ensure the convergence.

Convergence against vacuum size was tested on the 231 unit cell, with vacuum dimension varied from 10 \AA to 35 \AA .

Adsorption site and adsorbate geometry was re-optimized, and adsorbate energy was recalculated for every cell.

A summary of adsorption energies as a function of vacuum dimension, as well as

a function of minimal inter-adsorbate distance is given on a figure 3.5. One may see that the adsorption energy converges to meV accuracy for vacuum size of more than 15Å, and for X-Y dimensions equal or larger than 7Å (cell 231).

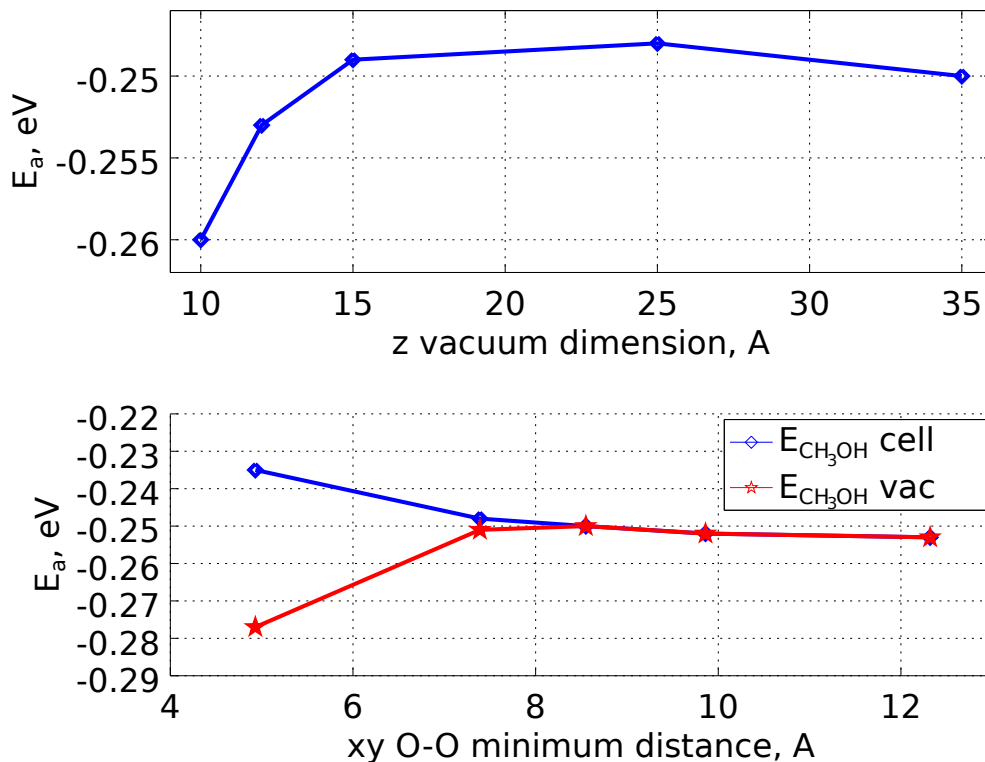


Figure 3.5 – Methanol on graphene: strongest adsorption site geometry. 2x3x1 graphene sheet. Bottom figure, blue trace (diamonds): adsorbate energy recalculated in the same cell as slab+adsorbate system, red trace (stars): adsorbate energy calculated once in a big (10x10x10Å) cell.

Finally, convergence against the slab thickness was studied: adsorption energy on graphene, two and three-layered graphite was calculated. For graphite, the second layer was shifted by intercarbon distance \mathbf{a} . All calculations were performed in the same 8.55x7.39x23Å cell, underlying slab layers of three-layer graphite were removed one after another. Vacuum size was of 16.6Å, 19.8Å and 23Å for three-, two- and single-layer slabs respectively. Calculation results are summarized in the Table 3.3. Passing from graphene to two-layer graphite increases the adsorption energy by 13 meV, that is 5%, doubling the calculation time. Employing three-layer model quadruples the calculation time, while increasing the calculated adsorption energy by 4 meV, or about 1% of the total adsorption energy value.

To conclude, using graphene as a model for graphite is feasible if calculation time is a concern and there is no need for a high accuracy. Otherwise, two-layer model is sufficient.

Slab layers	Ea, eV	dEa (+1L), eV	dEa (+1L),%	Time, s
1	-0,247			60
2	-0,260	-0,013	0,051%	145
3	-0,264	-0,004	0,016%	251

Table 3.3 – Convergence against number of slab layers, CH₃OH on graphite.

3.3.5 d Surface defects influence

Interstellar graphitic surfaces are rarely perfect and a large amount of carbonaceous dust grains are of amorphous carbon. Dominance of hydrogen in the ISM and routine detection of C-H dangling bonds suggest the presence of hydrogenated sites on the graphitic surfaces. [19, 20]

In order to evaluate the role of surface defects, adsorption on two model defects: vacancy (fig. 3.6) and hydrogenated vacancy (fig. 3.7), was studied. An intact underlying layer of graphene was added, shifted by intercarbon distance \mathbf{a} , to stabilize the surface. Positions of atoms of this underlying layer were frozen during all geometry optimizations. The cell of 8.55x7.39x16.5Å was used, with the vacuum size of 13.2Å.

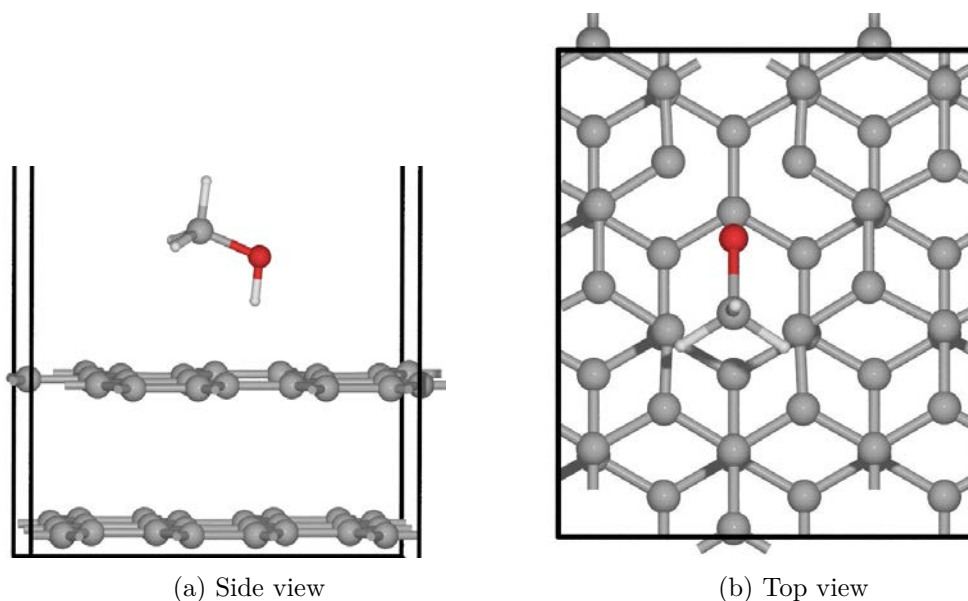


Figure 3.6 – Methanol on graphite with two-carbon vacancy: strongest adsorption site geometry. 2x3x2 graphite sheet, 13.2Å vacuum.

For both defects, the strongest site search was performed from scratch. Few initial adsorbate positions were tested, with adsorbate placed parallel to the surface, in the vicinity of the defect. Strongest adsorption geometries are presented on fig. 3.6 and fig. 3.7. The summary of adsorption energies is given in the Table 3.4. One may find that the adsorption energy increases significantly with introduction of defect sites into the surface model.

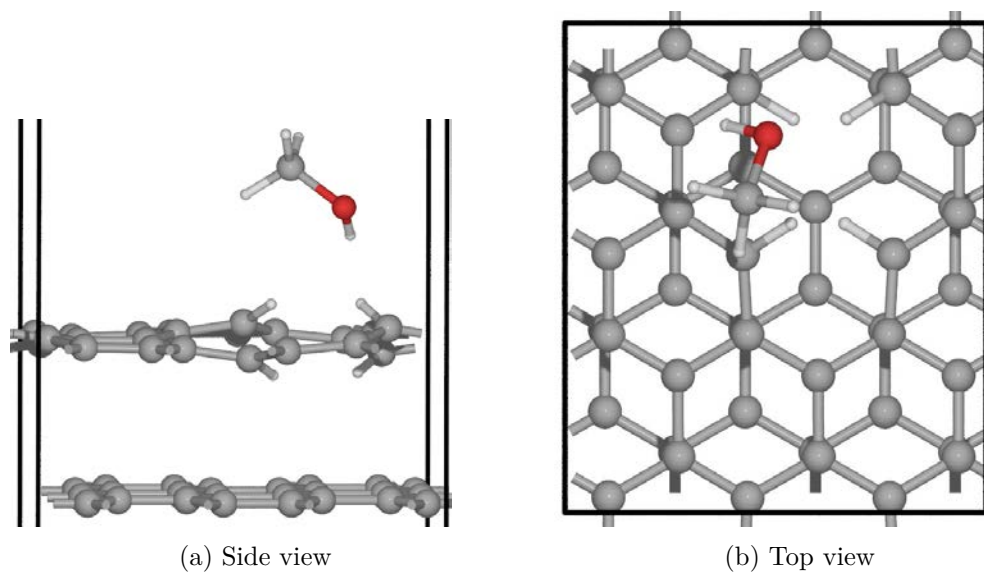


Figure 3.7 – Methanol on graphite with hydrogenated vacancy: strongest adsorption site geometry. 2x3x2 graphite sheet, 13.2Å vacuum.

Surface	E_a , eV	d^{C-O} , Å
Graphite	-0.260	3.104
2C Vacancy	-0.315	2.70
2C vac.+4H	-0.340	2.77

Table 3.4 – Strongest CH_3OH adsorption sites on graphite, graphite with defects. 8.55x7.39x16.5Å cell, 13.5Å vacuum size.

3.3.5 e Conclusion

It was found that methanol adsorbs preferentially in the orientation parallel to the surface.

A model of graphite with two-layer graphene or single layer graphene planes gives inferior adsorption energies, compared to the adsorption on the surface with defects or experimental data obtained in this work using HOPG surface with uncontrolled defects (2.3.3).

Energies of methanol adsorption on graphene determined here are consistent with the values obtained by Schröder[18].

3.4 Topological analysis

Based on the theory of gradient dynamical systems, the topological analysis of scalar functions was proposed as a bridge between the traditional pictures of the chemical bond derived from the Lewis theory [21, 22], and first principles quantum-mechanical methodologies. This analysis gives non-overlapping regions of the molecular space, providing an interesting alternative to overcome the complexity of molecular orbital analysis due to their delocalized character. These regions are termed basins (noted Ω) and are stable manifolds of the attractors (maxima) of a scalar function.

3.4.1 Electronic Localization Function (ELF)

While the topology of the electron density is only atomic (Atoms in Molecules Theory) [21], the topological properties of the Electron Localization Function (ELF) proposed by Becke et al.[23] makes possible a partitioning of the physical space into non-atomic basins. Since the last twenty years, the ELF topological analysis has been intensively used for the study of bonding schemes in molecules and solids, or for rationalizing chemical reactivity [24]. The function relies on the Laplacian of the conditional same spin pair probability scaled by the homogeneous electron gas kinetic energy density. Thus, ELF is generally interpreted as a signature of the electron-pair distribution. This formulation has been generalized to the Density Functional theory by Savin et al. [25], and rationalized in terms of the local excess kinetic energy due to the Pauli repulsion. The ELF analysis is achieved by applying the theory of dynamical systems.

The basins are localized around attractors and are separated by zero-flux surfaces. Thus, in addition to core basins surrounding nuclei with atomic number $Z > 2$, non-atomic valence basins are found. These basins are characterized by the number of core basins with which they share a common boundary (zero-flux surface). This number is called the synaptic order [26]. Each valence basin is presented with a chemical meaning in agreement with the Lewis theory (see Table 3.5).

Overall, the spatial distribution of the valence basins closely matches the non-bonding and bonding domains of the Valence shell electron pair repulsion (VSEPR) model [27].

Synaptic order	Type	Symbol	bond
1	monosynaptic	V(X)	lone pair
2	disynaptic	V(X,Y)	bicentral bond
≥ 3	polycentric	V(X,Y,Z,...)	polycentric bond

Table 3.5 – ELF Valence basins

3.4.2 Integrated properties

The volumes and the populations of basins (Ω) are integrated properties. For example, the basin population is calculated by integration of the electron density over the basin volume as follows:

$$pop(\Omega) = \int_{\Omega} \rho(\mathbf{r}) d^3\mathbf{r}$$

Most commonly, basin volumes and populations are used in order to rationalize the bonding schemes in molecules or in solids. The atomic AIM charge $q(\Omega)$ of any topological atom is calculated by subtracting the atomic population from the atomic number of each atom, Z . Overall, the integrated properties of basins have a chemical meaning inherited from the partition and thus, the integration of the density over an ELF V(A, B) or V(D) basin can be understood as the bond population of the two-centre A-B bond or of the one-centre D lone pair.

3.4.3 Example of ELF topology: methanol

Nine ELF basins may be distinguished for CH₃OH molecule (fig. 3.8):

- two core basins associated with carbon and oxygen atoms (blue);
- two monosynaptic basins on oxygen, representing the oxygen lone pairs (red);
- four protonated disynaptic basins, V(O,H) and 3 V(C,H) corresponding to O-H and C-H bonds respectively (purple);
- one disynaptic bicentral basin V(C,O) corresponding to C-O bond (violet).

It may be notified that positions of lone pairs and bonds conform to the VSEPR domains. Carbon atom is situated in the centre of a tetrahedron corresponding to AX₄ configuration. Molecule is bent on the oxygen atom, forming a configuration AX₂E₂.

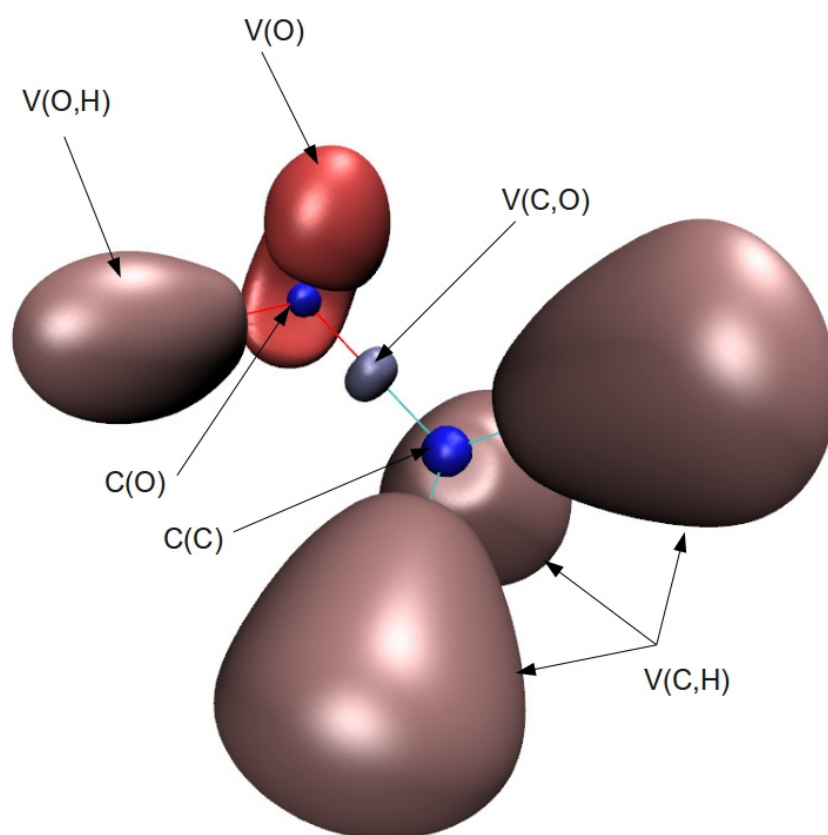


Figure 3.8 – Localization domains of CH_3OH molecule ($\eta = 0.84$)

References

- [1] David Sholl and Janice A. Steckel. *Density Functional Theory: A Practical Introduction*. en. John Wiley & Sons, Sept. 2011.
- [2] Wolfram Koch, Max C Holthausen, and Max C Holthausen. *A chemist's guide to density functional theory*. Vol. 2. Wiley-Vch Weinheim, 2001.
- [3] P. Hohenberg and W. Kohn. "Inhomogeneous Electron Gas". In: *Physical Review* 136.3B (1964), B864–B871.
- [4] W. Kohn and L. J. Sham. "Self-Consistent Equations Including Exchange and Correlation Effects". In: *Physical Review* 140.4A (1965), A1133–A1138.
- [5] John P. Perdew, Kieron Burke, and Matthias Ernzerhof. "Generalized Gradient Approximation Made Simple". In: *Physical Review Letters* 77.18 (1996), pp. 3865–3868.
- [6] Kyuho Lee et al. "Higher-accuracy van der Waals density functional". In: *Physical Review B* 82.8 (2010), p. 081101.
- [7] Oleg A. Vydrov and Troy Van Voorhis. "Nonlocal van der Waals density functional: The simpler the better". In: *The Journal of Chemical Physics* 133.24 (Dec. 2010), p. 244103.
- [8] M. Dion et al. "Van der Waals Density Functional for General Geometries". In: *Physical Review Letters* 92.24 (2004), p. 246401.
- [9] Stefan Grimme. "Semiempirical GGA-type density functional constructed with a long-range dispersion correction". en. In: *Journal of Computational Chemistry* 27.15 (2006), pp. 1787–1799.
- [10] T. Björkman et al. "Are we van der Waals ready?" In: *Journal of Physics: Condensed Matter* 24.42 (Oct. 2012). arXiv:1206.3542 [cond-mat, physics:physics], p. 424218.
- [11] Daniel G. A. Smith and Konrad Patkowski. "Interactions between Methane and Polycyclic Aromatic Hydrocarbons: A High Accuracy Benchmark Study". In: *Journal of Chemical Theory and Computation* 9.1 (2013), pp. 370–389.
- [12] G. Kresse and J. Furthmüller. "Efficient iterative schemes for $\textit{ab initio}$ total-energy calculations using a plane-wave basis set". In: *Physical Review B* 54.16 (1996), pp. 11169–11186.
- [13] P. E. Blöchl. "Projector augmented-wave method". In: *Physical Review B* 50.24 (1994), pp. 17953–17979.
- [14] G. Kresse and D. Joubert. "From ultrasoft pseudopotentials to the projector augmented-wave method". In: *Physical Review B* 59.3 (1999), pp. 1758–1775.
- [15] Sune R. Bahn and Karsten W. Jacobsen. "An Object-Oriented Scripting Interface to a Legacy Electronic Structure Code". In: *Computing in Science & Engineering* 4.3 (May 2002), pp. 56–66.
- [16] *Atomic Simulation Environment*. <https://wiki.fysik.dtu.dk/ase/>, 2015.

- [17] Ding Pan et al. "Surface energy and surface proton order of the ice Ih basal and prism surfaces". en. In: *Journal of Physics: Condensed Matter* 22.7 (Feb. 2010), p. 074209.
- [18] Elsebeth Schröder. "Methanol Adsorption on Graphene". en. In: *Journal of Nanomaterials* 2013 (Sept. 2013), e871706.
- [19] Th. Henning and F. Salama. "Carbon in the Universe". In: *Science. New Series* 282.5397 (1998), pp. 2204–2210.
- [20] B. GRUN. *Interplanetary Dust*. Astronomy and Astrophysics Library. Springer, 2001.
- [21] Richard F. W. Bader. "A quantum theory of molecular structure and its applications". In: *Chemical Reviews* 91.5 (1991), pp. 893–928.
- [22] B. Silvi and A. Savin. "Classification of chemical bonds based on topological analysis of electron localization functions". en. In: *Nature* 371.6499 (1994), pp. 683–686.
- [23] A. D. Becke and K. E. Edgecombe. "A simple measure of electron localization in atomic and molecular systems". In: *The Journal of Chemical Physics* 92.9 (May 1990), pp. 5397–5403.
- [24] B. Silvi, R. J. Gillespie, and C. Gatti. "9.07 - Electron Density Analysis". In: *Comprehensive Inorganic Chemistry II (Second Edition)*. Ed. by Jan Reedijk and Kenneth Poeppelmeier. Amsterdam: Elsevier, 2013, pp. 187–226.
- [25] Andreas Savin et al. "Electron Localization in Solid-State Structures of the Elements: the Diamond Structure". en. In: *Angewandte Chemie International Edition in English* 31.2 (1992), pp. 187–188.
- [26] Bernard Silvi. "The synaptic order: a key concept to understand multicenter bonding". In: *Journal of Molecular Structure* 614.1–3 (2002), pp. 3–10.
- [27] R. J. Gillespie. "Fifty years of the VSEPR model". In: *Coordination Chemistry Reviews* 252.12–14 (2008), pp. 1315–1327.

Part II

Systems studied

Chapter 4

Adsorption and Trapping of Noble Gases by Water Ices

4.1 Study context

4.1.1 Planetology issue

Titan is the biggest satellite of Saturn and the only moon of the solar system with a significant atmosphere. It is also one of the most studied, in particular because it is often considered as a possible analog of the primitive Earth, hence its major importance in the quest for understanding our own origins and evolution. Titan has most probably been formed, 4.6 millions of years ago, at the same epoch as Saturn and Jupiter which belong to the giant planets family; in which case, it should be issued from the same building blocks present in the feeding zone of Saturn during the accretion phase of the primitive nebula [1].

In 2005 the Cassini-Huygens mission was able to give precious information on the structure and composition of Titan. While descending towards the surface of Titan, the Huygens probe aimed at detecting different chemical species with the Gas Chromatograph Mass Spectrometer (GCMS) on board.

An unexpected result was that the Titan atmosphere contains no other heavy noble gas than argon and that the argon which is detected is mainly ^{40}Ar , isotope which is produced by the radiogenic decay of potassium ^{40}K . Some primordial ^{36}Ar is seen but very under-abundant compared to the solar value (about 6 orders of magnitude) [2].

The other primordial noble gases, i.e. ^{38}Ar , krypton and xenon, have not been detected at all by the instrument GCMS, which implies that their molar fractions with respect to hydrogen are under the detection limit of Huygens GCMS (10^{-8}) in Titan atmosphere. By comparison, Jupiter presents an atmosphere enriched (by a factor of 2 to 3) in noble gases with respect to the solar value [3].



Credit NASA/JPL-Caltech/SSI Titan/Saturn by Cassini probe (2012)

4.1.2 Update review

This noble gases deficiency has been extensively studied and multiple scenarios have been proposed, based either on physical [4–8] or on chemical [9–15] trapping processes. None of them, however, gave a global satisfactory interpretation. Till now, among all these scenarios, the two most promising implied a chemical trapping by H_3^+ (sect. 4.1.2 a) and a physical trapping into clathrates structures (sect. 4.1.2 b).

4.1.2 a Chemical trapping

A chemical trapping process was proposed by Mousis et al. [12] based on an exhaustive theoretical study of the interaction of molecular ion H_3^+ with noble gases Ar, Kr and Xe [13, 14]. This mechanism is assumed to occur during the formation of the satellite's constructive planetesimals and it depends mostly on the abundance of H_3^+ molecules in that medium. Therefore modeling the H_3^+ abundance profile is crucial [15] and the values proposed for its abundance are still rather disputed.

4.1.2 b Clathrates trapping

Osegovic and Max [6] proposed that the noble gases could have been stocked in a specific allomorphism of water ices, i.e. clathrates, supposed to be present on Titan's surface and they showed that xenon could be efficiently trapped in this way. However the code used was not adapted to the physical conditions of the primitive nebula and Titan and consequently their results even if promising were not reliable. Later on, Thomas et al. [7] demonstrated that krypton and xenon could be efficiently trapped by clathrates supposing their abundance to be large enough, and Mousis et al. [8] showed that argon could also be trapped by this mechanism. But in fine it has to be reminded that the existence of this mechanism relies on the presence of clathrates in Titan and the possibility of clathrates to be formed in interstellar conditions, which is still highly controversial.

There are other possible trapping mechanisms at work in the nebula, among which the mechanism of adsorption on the solid surfaces available in the primitive nebula. The icy coating of the primitive grains can capture the noble gases without having disputed structures as clathrates intervening. The impact of this physical mechanism on the noble gases abundances has yet to be investigated.

4.1.3 Trapping by ices

The giant molecular clouds of molecular hydrogen are star-forming regions: once the gas clouds become dense enough, they start to collapse by the effect of gravity, resulting in the formation of a star and a gaseous proto-planetary disk around the young star. According to the current scenarios, most ices falling onto the proto-planetary disk vaporized when entering the solar nebula around 30 AU from the newly formed star (1AU is the mean distance between the Earth and the Sun, used as a unit of length in astronomy). As the temperature decreased with time, the water molecules started to condense at about 150 K, in the form of microscopic crystalline ice [16]. It is then considered that the volatiles present in the medium within 30 AU from the star could be trapped by those ices (eventually as clathrate hydrates if these structures can exist

in such an environment), ices which subsequently accumulated with refractory dust to form planetesimals, former bodies of planets and comets [1].

Therefore, here is presented an exhaustive study of the behavior of noble gases atoms, argon, krypton and xenon in the presence of water ice. A double approach, experimental and computational, is used to determine the energetic stability of structures able to withdraw noble gases from the native atmosphere of Titan before it was formed.

4.2 Experimental approach

4.2.1 Laboratory ice samples

In SPICES experimental setup, ices are grown in-situ from the water vapour according to the method described in the section 2.1.6. Water films are grown on either graphite or gold surfaces. Gold surface should be preferred because of better wetting [17] and higher reflectivity in the infrared wavelength range, permitting the survey of the deposited ice by means of Reflection-Absorption Infrared Spectroscopy (RAIRS).

Ice films thickness is controlled as a multiple of the monolayer water coverage (sect. 4.2.1 a). Amorphous (sect. 4.2.1 b) or (poly) crystalline (sect. 4.2.1 c) ice films are grown, depending on the substrate temperature. Ice sample morphology is verified by means of RAIRS spectroscopy by following H_2O O-H stretching modes around 3250 cm^{-1} .

4.2.1 a Water ice monolayer calibration and ice thickness

A monolayer (ML) calibration on HOPG surface was performed as described in (sect. 2.3.1, sect. 2.2.2). A series of TPD experiments at various initial coverages θ_0 were conducted, with a heating rate of 15K/min. Intact water molecule mass 18 was tracked. Resulting desorption curves are shown on a figure 4.1. Monolayer is identified as the coverage at which the TPD curve maximum starts to shift to higher temperatures with increasing initial coverage. An additional indicator of a transition to multilayer regime is the superposition of low-temperature part of the curves (4-6).

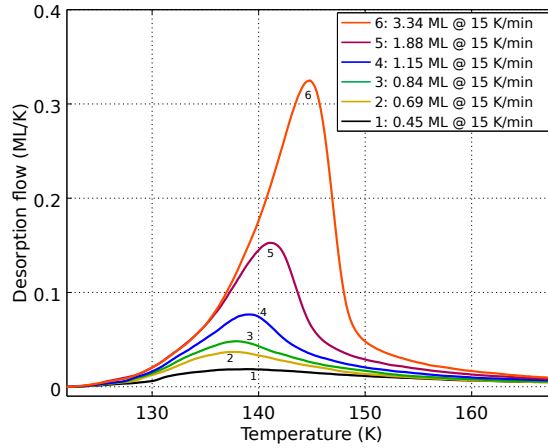


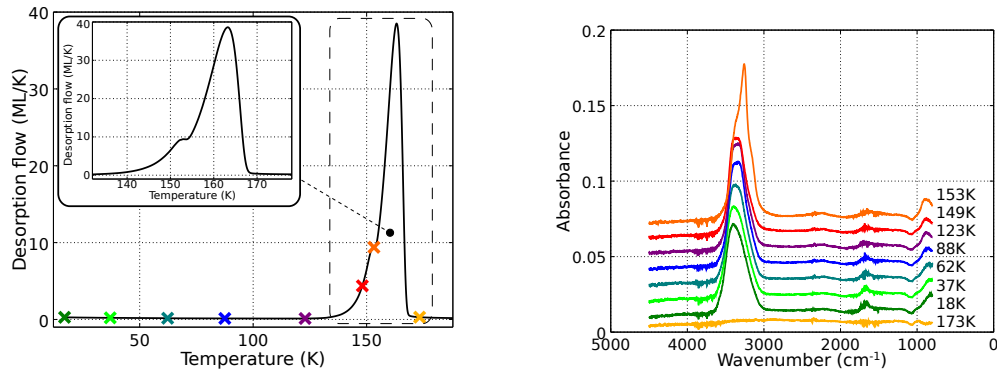
Figure 4.1 – H_2O on HOPG monolayer coverage search. Heating rate 15K/min. Desorption integral of the monolayer $I_{ML}^{TPD} \approx 2 \times 10^{-8} A \cdot s$.

Desorption signal integral of a monolayer is found to be $I_{ML}^{TPD} \approx 2 \times 10^{-8} A \cdot s$, corresponding deposition signal integral $I_{ML}^{dose} \approx 3.2 \times 10^{-9} A \cdot s$ (derived from thick ice desorption experiment).

In this work $\approx 100ML$ thick water ices were used, ice thickness was systematically been verified by following the mass 18 signal during the desorption experiments.

4.2.1 b Amorphous ice

If deposited below $\approx 120K$, water ice takes the amorphous form. A shoulder in the desorption curve is observed at temperatures around 150K, corresponding to the ice crystallization (fig. 4.2a). The origin of this step is in the fact that the vapour pressure of amorphous ice is higher than that of crystalline ice.



(a) TPD spectra. Crystallization feature is observed at 153K.

(b) Infrared spectra. Ice crystallization changes the shape of $3200cm^{-1}$ OH stretching band

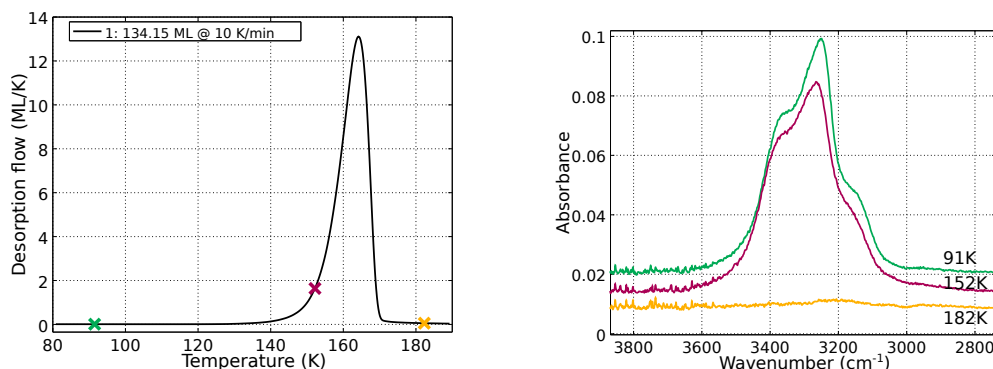
Figure 4.2 – Desorption and infrared spectra of 400ML-thick amorphous ice deposited at 10K. Heating rate 5K/min, mass 18 signal is followed. Infrared spectra recorded at $2cm^{-1}$ resolution, averaging over 50 scans.

Infrared spectra permits to verify the amorphous character of deposited ices in a non-destructive manner: OH stretching band around $3200cm^{-1}$ is unstructured for amorphous ice, while a typical crystalline ice structure emerges at temperatures above 150K (fig. 4.2b). For thick and extremely porous ices, OH dangling band may also be observed around $3700 cm^{-1}$. It is not distinguishable on the spectra presented here (fig. 4.2b).

Grade of porosity depends on the ice preparation technique [18]. In our setup, non-porous amorphous ice may be produced by deposition on a substrate having a temperature of 110K. Porosity increases considerably with lower substrate temperatures [19] during the deposition. If an extremely non-porous surface is needed, ice may be annealed at $\approx 120K$ for several hours.

4.2.1 c Crystalline ice

Crystalline ice may be directly prepared by vapour deposition at relatively high substrate temperatures of $\approx 140K$. Due to the lower sticking coefficient, the deposition signal integral needs to be multiplied by a factor 1.3 to obtain the equivalent thickness of the ice, compared to the amorphous ice deposition at 110K. Once prepared, the crystalline structure is retained even if the ice sample is cooled down to cryogenic temperatures. Ice morphology may be verified by the presence of a typical form of OH stretching band at $3200cm^{-1}$ (fig. 4.3b). The absence of crystallization step on the desorption curve (fig. 4.3a) serves as an additional a posteriori indicator of the crystalline ice structure.



(a) TPD spectra. Absence of crystallization step.

(b) Infrared spectra. The shape of 3200cm^{-1} OH stretching band corresponds to crystalline ice even at 90K.

Figure 4.3 – Desorption and infrared spectra of 100ML-thick crystal ice deposited at 140K. Heating rate 10K/min, mass 18 signal is followed. Infrared spectra recorded at 2cm^{-1} resolution, averaging over 50 scans.

It is impossible to identify the exact crystalline form of ice that is deposited neither by means of infrared spectroscopy nor by temperature programmed desorption technique. Other studies suggest that the ice deposited in similar conditions takes the form of cubic ice I_c [20], and hexagonal ice may be produced by prolonged annealing of the amorphous ice at temperatures of $\approx 140\text{K}$

4.2.2 Adsorption on water ices

Adsorption of noble gases: Ar, Kr, Xe on crystalline and amorphous water ices was studied using the approach described in the chapter 2.3. Ices of thickness of 100-500 ML were used, grown on the HOPG surface. Ices were deposited in-situ from water vapour as described in sect. 4.2.1. Crystalline ices are deposited at the sample temperature of 140K. Amorphous ices were prepared using the substrate temperature of 110K. Deposition at lower temperatures led to increased porosity and observable compactification of the ice during the experiment time.

Ices then were cooled to cryogenic temperatures and one of the gases, Argon, Krypton or Xenon was deposited on top. Deposition temperatures of 15K were used for Argon and Krypton, Xenon was deposited at 30K. Desorption curves were recorded by following the isotopes ^{40}Ar , ^{84}Kr and ^{129}Xe . Heating rates of 3 to 5 K/min were employed for all the measurements except the multi-rate prefactor search. Upper temperatures of 80K were used for TPD records, which permitted to make a series of measurements on the same ice sample without desorbing and redepositing the ice.

First, a monolayer coverage integral was identified (sect. 4.2.2 a). Then the need to correct for background signal due to parasite desorption and pumping inertia was evaluated (sect. 4.2.2 b). Multilayer adsorption energy was determined to define the lower limit of the adsorption energies (sect. 4.2.2 c) Finally, the adsorption energies and the corresponding desorption prefactor values in the sub-monolayer regime were obtained (sect. 4.2.2 d).

4.2.2 a Monolayer coverage calibration

To identify the monolayer coverage of Argon on a crystalline ice, a series of desorption curves were obtained for the same ice substrate and different deposited initial coverages of Argon (fig. 4.4).

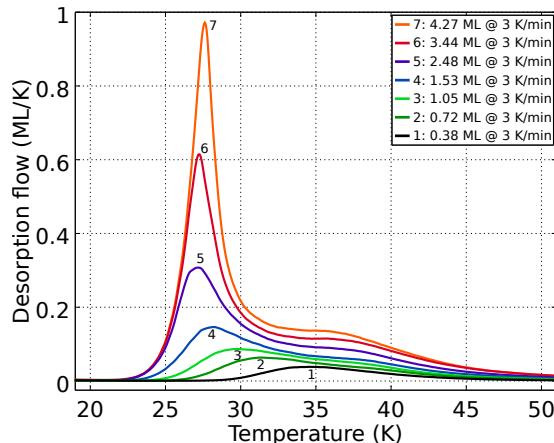


Figure 4.4 – Ar / crystalline H₂O / HOPG monolayer coverage search. Heating rates 3K/min, desorption integral of the monolayer $I_{ML}^{TPD} \approx 1 \times 10^{-7} A \cdot s$.

One may observe that with increasing initial coverage a peak at low temperatures starts to emerge, with the temperature of the maximum lowering with increasing coverage (curves 2-4). If the initial coverage is further increased, the low-temperature parts of curves start to superpose (curves 5-7), that is a clear indication of zero-th order desorption and multilayer regime. However the exact monolayer coverage is impossible to determine precisely since no saturation of the high-temperature monolayer part is observed. This situation is acceptable since knowing the absolute surface coverage is not required to determine adsorption energies. Here, the monolayer desorption integral is taken to match the integral of the curve 3, the last one without an important contribution of the multilayer desorption peak at around 27K.

4.2.2 b Parasite desorption signal

The absence of the monolayer peak saturation (sect. 4.2.2 a) is due to the background signal: pumping inertia and desorption from other cold parts of the cryostat. It may be compensated by performing a supplementary desorption experiment with the same surface coverage and the sample surface facing off QMS (see the sect. 2.1.7 b for more details).

For example, on Figure 4.5 the background signal corresponding to Ar pumping deficiency is presented. One may see that at temperatures higher than 45K both signals superimpose, i.e. the desorption signal becomes independent of the sample surface orientation. That indicates that the desorption signal detected above that temperature is entirely due to the sources other than sample surface. Detected signal is due to the desorption from cryostat cold parts and to the pumping deficiency.

Although such an approach seems to work well to compensate for the background signal detection, it has some limitations.

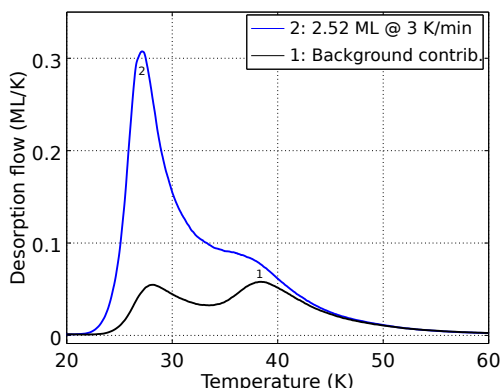
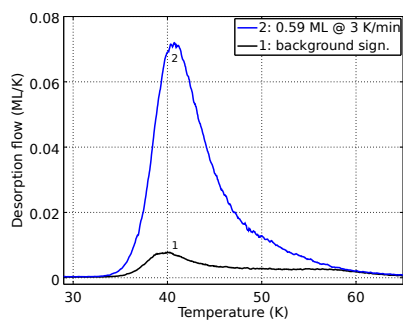


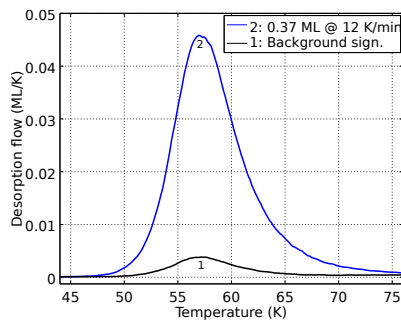
Figure 4.5 – Background signal correction: Ar / crystalline H₂O / HOPG. Initial coverage \approx 2ML, Heating rates 3K/min. Blue curve: normal TPD; black curve: TPD reproduced with same initial coverage, surface facing off QMS.

First of all, a precise reproduction of the adsorbate deposited quantity is needed to employ the method correctly. Such a requirement increases the experiment time by at least factor of two, requiring a supplementary desorption experiment for every initial coverage point.

Secondly, an additional error may be introduced since the background signal connected with desorption from the cryostat is dependent on the experiment history. That may lead to overcompensated or under-compensated background signal, if a series of Temperature Programmed Desorption (TPD) with decreasing or increasing initial coverage is performed.



(a) Kr background signal



(b) Kr background signal

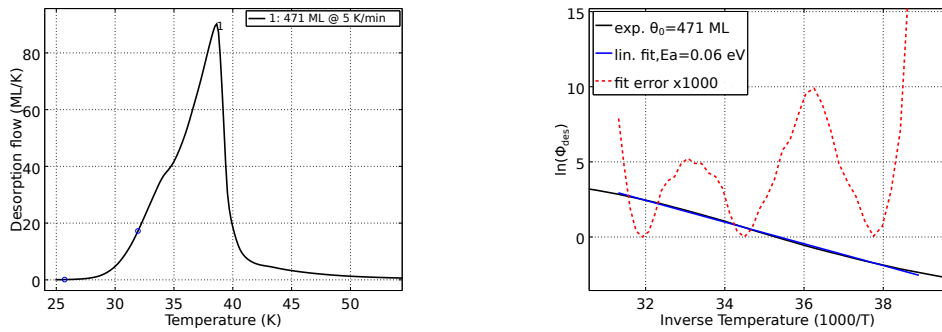
Figure 4.6 – Kr, Xe background signal contributions. Blue curves: TPD with sample surface facing QMS, normal signal. Black curves: sample surface facing off QMS, background signal is detected.

For the cases of Kr and Xe adsorption the background signal problem is much less pronounced. Background signal integral fraction for Kr and Xe is 0.16 and 0.097 respectively, no significant tail is introduced by the background signal. To compare, for the case of Argon the background signal integral fraction reaches values of 0.40, i.e. 40% of detected argon atoms are not coming directly from the surface. We believe

that the low adsorption temperature of Ar and its important pumping inertia both stand at the origin of that effect.

4.2.2 c Multilayer adsorption energy

To obtain the inferior limit on the adsorption energy, the multilayer adsorption energy is determined from the zero-th order desorption curves. The adsorption energy is derived from the slope of the desorption flow logarithm $\ln(\Phi_{des})$ against the inverse temperature T^{-1} (refer to sect. 2.3.2 for the method). As an example, Figure 4.7 presents the desorption of $\approx 500ML$ thick Argon layer deposited above the amorphous water ice.



(a) Ar multilayer desorption curve. Circles limit the part used for the linear regression (fig. 4.7b).

(b) $\ln(\Phi_{des})$ against the inverse temperature T^{-1}

Figure 4.7 – Argon adsorption energy from the zero-th order desorption of a thick ($\approx 500ML$) Ar film adsorbed on the amorphous water ice sample. Heating rate 5K/min.

The multilayer adsorption energies obtained are presented in Table 4.1.

Atom	E_a [21], K	E_a [21], meV	This work E_a , meV
Ar	873	75	60 ± 10
Kr	1296	111	98 ± 10
Xe	1824	157	135 ± 10

Table 4.1 – Multilayer adsorption energies for Ar, Kr and Xe, compared to the values obtained by Schlichting et al.[21]

The adsorption energies obtained in this work are systematically lower than those by Schlichting et al.[21]. In the case of Ar, as stated before, outgassing of other parts of the cryostat may add artefact on our desorption curves. This is especially true when dealing with high coverages of Ar on the surface, since a large quantity of the atom may have been adsorbed on other cold parts of the cryostat. This could participate to the difference with the results of Schlichting et al. However, in the case of the two other noble gas, this effect is negligible. In this case, the provenance of this difference is not identified. One possible origin of such an error is the temperature control quality. In the current work the temperature is controlled to the precision of 0.5K, compared to

$\pm 0.7\text{K}$ uncertainty announced by Schlichting et al. The lower heating rates employed in current work also favour the precision, reducing possible temperature gradients.

4.2.2 d Sub-monolayer adsorption energy and desorption prefactor

Two parameters need to be determined to describe the desorption process in the sub-monolayer regime, desorption prefactor ν and adsorption energy E_a . Here, the method described in the chapter 2.3.3 is used. Prefactor is determined based on a set of desorption curves performed with the same initial surface coverage θ_0 (around 0.5ML) and different heating rates β taken in range from 1K min^{-1} to 15K min^{-1} . Figure 4.8 gives a summary of desorption curves employed and determined prefactor values.

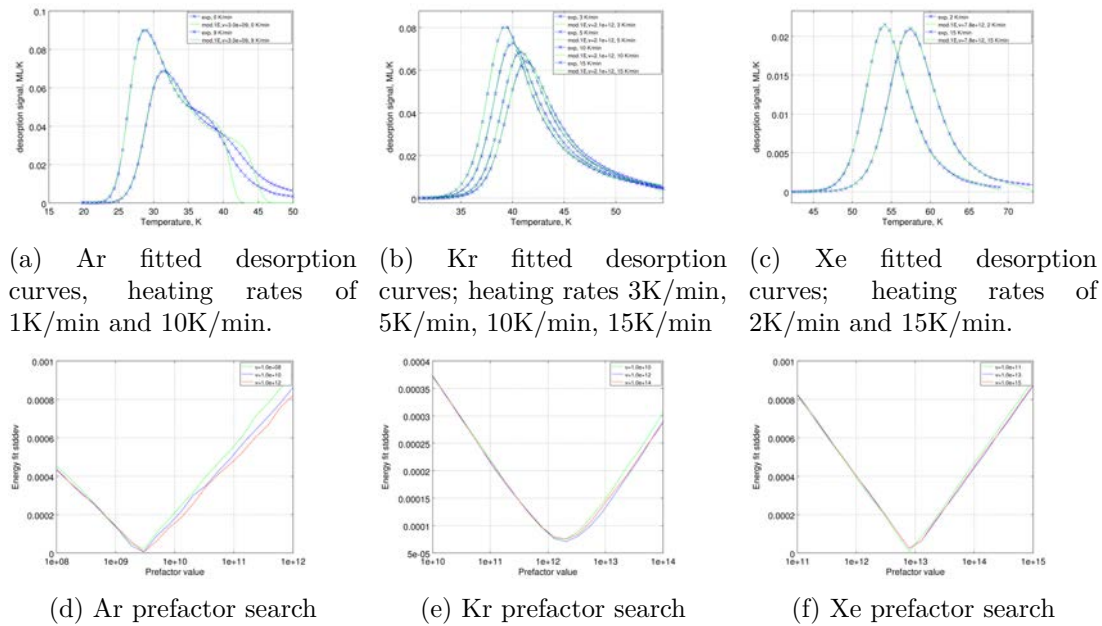


Figure 4.8 – Desorption prefactor from multi-rate experiments. Ar: $\nu = 3 \cdot 10^{9 \pm 0.5} s^{-1}$; Kr: $\nu = 2 \cdot 10^{12 \pm 0.5} s^{-1}$, Xe: $\nu = 8 \cdot 10^{12 \pm 0.5} s^{-1}$

In these cases, the experimental curves are well reproduced by the first order desorption kinetic law, if the distribution of adsorption sites is considered (fig. 4.9a-4.9c). The clear minima of the E_a deviation curves (fig. 4.8d-4.8f) allows for an unambiguous determination of the prefactor for each gas. The obtained prefactor values are of $\nu = 3 \cdot 10^{9 \pm 0.5} s^{-1}$ for Ar; $\nu = 2 \cdot 10^{12 \pm 0.5} s^{-1}$ for Kr; $\nu = 8 \cdot 10^{12 \pm 0.5} s^{-1}$ for Xe on the crystalline ice.

Once the average prefactor values are determined, a model with a distribution of adsorption energies E_i is fitted to match curves at different initial coverages. The determined distributions of adsorption sites (fig. 4.9d-4.9f) give a clear view on the noble gas adsorption on the ice surfaces. One may note that the adsorption energies found for highest coverages correspond well to the zero-order desorption energies found in the chapter 4.2.2 c.

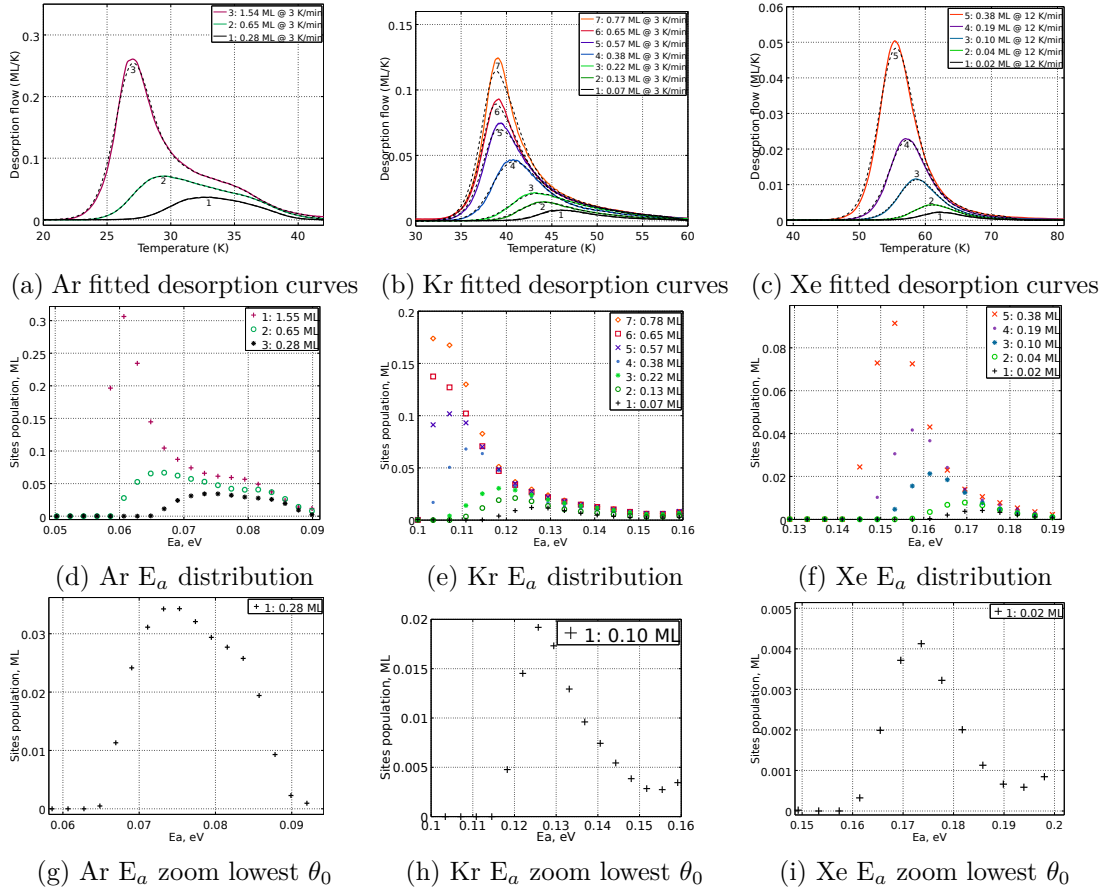


Figure 4.9 – Adsorption energy distribution fit. Three topmost figures: (solid) experimental Ar, Kr, Xe desorption curves, (dashed) first-order desorption model with the average prefactor and a distribution of adsorption sites with fractional populations θ_{0i} . Middle row figures: Ar/Kr/Xe fractional population of adsorption sites distribution, fitting the experimental curves. Bottom row figures: Zoom on the distribution corresponding to the lowest coverage curve.

4.2.2 e Adsorption on the amorphous water ice

The influence of the ice substrate morphology is evaluated by the use of the amorphous ice of comparable thickness instead of the crystalline one. The effect of the ice morphology was studied for the three noble gases. Only the results obtained for Ar are presented here.

The same monolayer calibration as in sect. 4.2.2 a is performed. On Figure 4.10 a set of desorption curves is presented corresponding to the Ar desorption from the amorphous ice at the heating rate of 3K/min. The sub-monolayer peak is broader and stronger, compared to the crystalline ice substrate (fig. 4.4). This is because the amorphous water ice has the higher surface area compared to that of the crystalline ice, presenting at the same time a slightly broader range of adsorption energies.

An additional high-temperature peak appears for curves corresponding to high initial coverage (around 34K, curves 5 to 7). It may be attributed to desorption coupled with diffusion from sites in the pores of the ice.

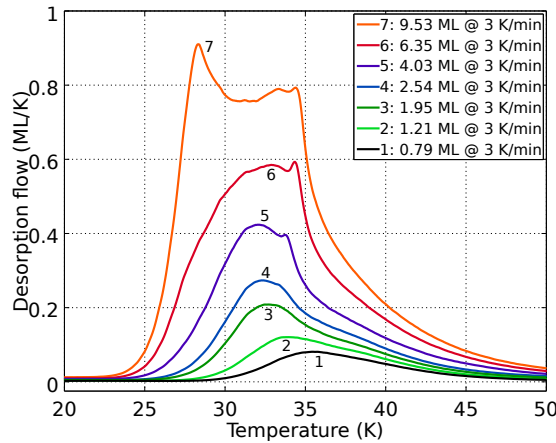


Figure 4.10 – Ar / amorphous H₂O / HOPG monolayer coverage search. Heating rates 3K/min. Coverage in terms of the monolayer on the crystalline ice.

4.2.2 f Summary

Table 4.2 presents the adsorption energy E_a corresponding to the maximum of the distribution. The precision is given by the width of the energy distribution dE_a .

Parameter	Ar	Kr	Xe
Desorption prefactor ν, s^{-1}	$\nu = 3 \cdot 10^{9 \pm 0.5}$	$\nu = 2 \cdot 10^{12 \pm 0.5}$	$\nu = 8 \cdot 10^{12 \pm 0.5}$
Crystal ice E_a , low θ_0 , meV	75	130	173
Crystal ice dE_a , meV	10	20	16
Amorphous ice E_a , low θ_0 , meV	82	125	175
Amorphous ice dE_a , meV	20	13	16

Table 4.2 – Noble gas experimental data summary

4.2.3 Inclusion in water ices

In order to evaluate if the noble gas atoms may be trapped within the ice bulk, a special series of experiment were performed. The adsorbate atoms were deposited on the previously prepared ice surface. Then, few equivalent layers of water molecules were deposited on top of the noble gas atoms, forming a sandwich with trapped noble gas atoms.

Since such experiments require a long time to perform (at least 3 hours per curve), requiring to prepare the ice for every new experiment, only a preliminary study was performed.

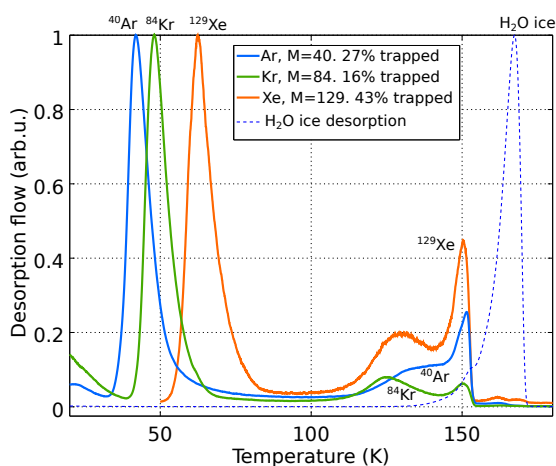


Figure 4.11 – Trapping of noble gases in the amorphous water ice, covered with 1-2 ML of ice. Heating rates 3K/min. Sub-monolayer noble gas initial coverage. Y axis normalized to TPD maximum. No comparison should be made between gases since the deposition conditions: temperature, noble gas thickness, recovering ice thickness are not the same.

As shown on Figure 4.11, all the noble gases may be trapped. The TPD curves exhibit three main desorption features for all the noble gas species. The low-temperature (below 100K) desorption peak is associated to the desorption of non-covered noble gas atoms. Smooth peak at 120-140K corresponds to the atoms diffusing through the ice along the warming-up and the onset of the ice sublimation. That is evidenced by the broad shape of the peak. High-temperature (150K) peak corresponds to atoms ejected from the ice during the ice crystallization.

The desorption signal for temperatures above 100K is associated with the desorption of the water ice itself, and therefore these features correspond to noble gas atoms trapped inside the ice. A numerical quantity may be assigned to characterize the trapping process: Integrating the total noble gas desorption flow and the desorption flow at temperatures above 100K, and taking a ratio of integrals will reflect the ratio of trapped atoms among the total deposited quantity.

The trapping data is summarized in Table 4.3. It may be seen that the trapping ratio (the last column) is dependent on the ice-gas-ice sandwich preparation conditions: the deposition temperature, the noble gas coverage, the recovering ice layer thickness. For example, Argon and Krypton may only be trapped if deposited at around 15K,

System	T_{dep}	Ice top, ML	$I_{TPD}^{20-200K}$, ML	$I_{TPD}^{100-200K}$, ML	trapped fraction
Ar	10K	6	0,132	0,073	0,554
Ar	10K	3	0,234	0,065	0,278
Ar	10K	1,5	0,216	0,047	0,215
Kr	13K	1,5	1,462	0,266	0,182
Kr	30K	0,5	2,114	0,078	0,037
Xe	50K	1,7	0,143	0,061	0,427
Xe	50K	1,7	0,247	0,082	0,333

Table 4.3 – Noble gas inclusion between water ice layers. Ice substrate is 400ML thick amorphous ice prepared at 100K. Second column gives the noble gas and covering ice layers deposition temperatures. Third column specifies the approximate covering ice thickness. Fourth column $I_{TPD}^{20-200K}$ gives the total desorbed quantity of a noble gas in the units of the effective ML on the crystalline ice. Fifth column $I_{TPD}^{100-200K}$ contains the desorption integral taken from 100 to 200K. Last column contains the ratio of the fifth and the fourth column, that is the fraction of a gas that is trapped inside the ice.

while Xenon may be deposited at 50K and still a big fraction is trapped.

To conclude, this preliminary study indicates a big potential of amorphous ice to trap noble gases. Further investigation must be performed to rigorously study the influence of the ice sandwich parameters: the ice thickness, the deposition temperature, a noble gas quantity on trapping. Diffusion through the ice bulk should also be verified using the isothermal survey at temperatures below the ice sublimation temperature.

4.3 Theoretical approach

4.3.1 Modeling the ice surface

Since many forms of ice exist and play role in the adsorption, modeling the ice structures becomes a non-trivial task. Luckily, the major part of the adsorption energy is determined by the water molecules in the direct vicinity of the adsorbate. That makes possible to stick to a limited set of model surfaces, if they represent a broad range of adsorption geometries.

An additional problem is posed by the fact that the proton order in ices is undefined, even if the oxygen grid positions are known. For crystal ice models, the only constraint is a Bernal-Fowler [22, 23] ice rule: exactly two hydrogens of neighbour water molecules form hydrogen bonds with lone pairs of the water molecule oxygen atom.

In this work an apolar hexagonal ice model with surface protons ordered as proposed by Fletcher[24] is used. Studies [25, 26] show that it is the most stable surface configuration of the hexagonal ice basal (0001) plane. For slab systems, the bulk proton ordering variation [27] has a small effect on the total energy, compared to the surface ordering [25].

To prepare the surface model, the following steps were performed: First, bulk structure was optimized to obtain the ground state geometry of ice (sect. 4.3.1 a). Then, the minimal slab was reoptimized with 15Å of vacuum in Z direction (sect. 4.3.1 b). Finally, the minimal slab was multiplied in x-y directions to accommodate the adsorbate (sect. 4.3.1 c) For further calculations, the positions of the bottom layer of water molecules were constrained to maintain the surface geometry. The topmost surface layer is always kept free to relax to the local potential energy minimum.

4.3.1 a Bulk optimization

The resulting bulk structure is shown on the figures 4.12b(basal plane view) and 4.12a(side view).

The bulk structure with protons ordered to give apolar surfaces for basal (0001) and prism (10 $\bar{1}$ 0) cuts is used. The cell volume and atoms geometry are reoptimized for minimal orthogonal unit cell containing 8 water molecules (fig. 4.12). For this optimization, an energy cut-off of 800 eV for the basis set plane waves was used and a 9x9x9 gamma-centered K-points mesh is employed. The minimum force per atom criteria is used to interrupt the geometry optimization loop, with the force threshold of 0.007 eV/Å. After the geometry optimization, the cell dimensions became (4.33x7.49x7.07)Å. A bulk ice cohesive energy of -714 meV/ H_2O or -25 meVÅ⁻³ is found, which is slightly higher than the values obtained in [25]. The difference comes from the routine use for dispersion force corrections [28](sect. 3.1.3) in the current work.

4.3.1 b Slab surface

After the bulk geometry reoptimization, two minimal slabs (basal and prism) were produced. The basal slab was produced by adding 15Å of vacuum in the Z direction of the bulk cell (cell dimensions 4.33 × 7.49 × 21.75Å). The prism slab was produced

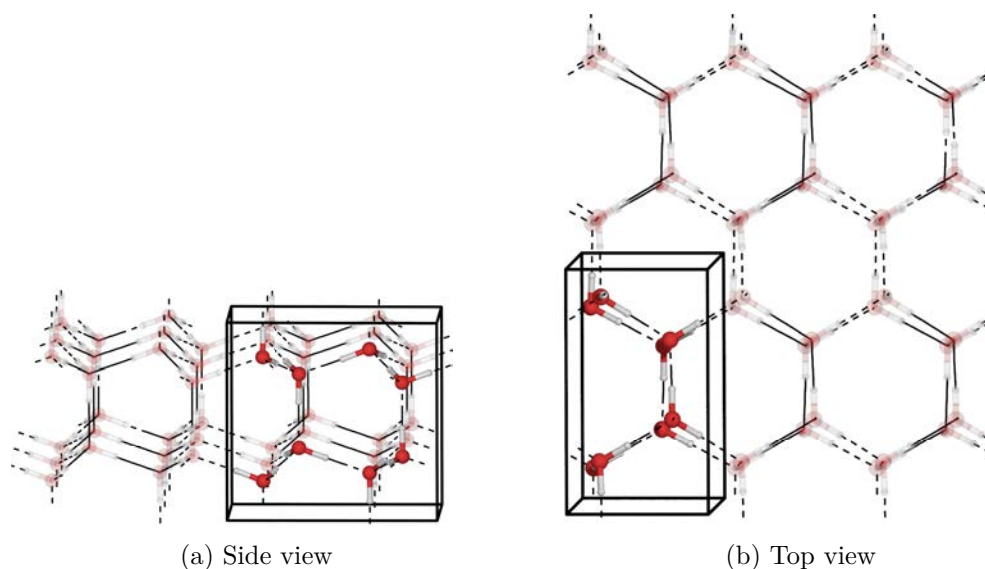


Figure 4.12 – Hexagonal ice I_h minimal orthogonal unit cell (solid color), $3 \times 2 \times 1$ image (transparent)

by rotating the bulk cell by 90° around the x axis and adding 15Å of vacuum ($4.33 \times 7.07 \times 22.49$ Å cell).

The slab molecules were relaxed to the minimum of the potential energy. The calculation was performed with a standard energy cut-off of 400eV and $5 \times 3 \times 1$ gamma-centered K-points mesh was used.

4.3.1 c Final slab geometries

Finally a $2 \times 1 \times 1$ slab (fig. 4.13) containing two ice bilayers was used for probing adsorption geometries. The positions of the bottom layer molecules of the slab were constrained and the top layer was left free to relax to the potential energy minimum for all calculations hereafter.

Inclusion and substitution calculations for rare gases (sect. 4.3.5, 4.3.6) were performed on a thick $2 \times 1 \times 2$ slab (4 BL) with the two topmost layers unconstrained.

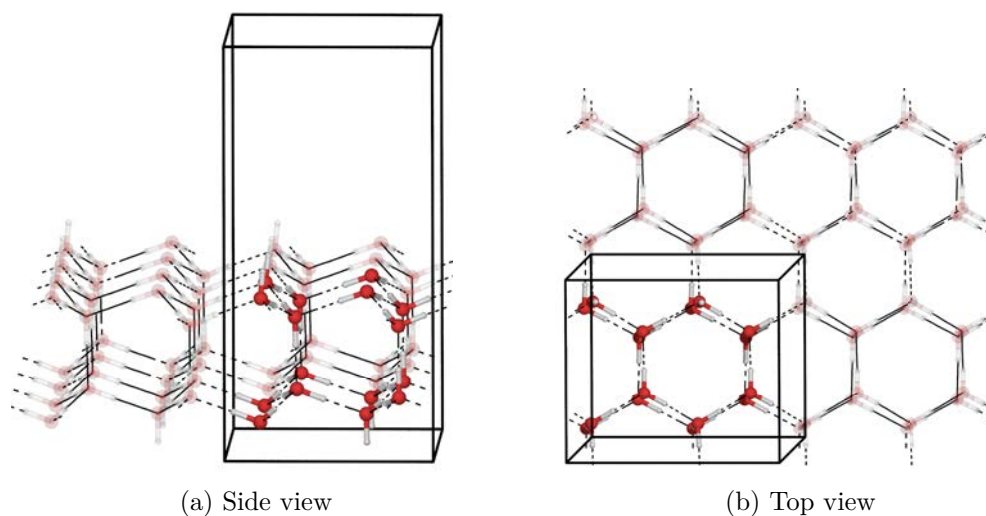


Figure 4.13 – Hexagonal ice I_h basal plane, 2x1x1 image was used to probe the adsorption sites.

4.3.2 Adsorption sites

For noble gas atoms, a number of adsorption sites were identified on the basal plane of the ice model (fig. 4.14).

Among them two sites are in the center of hexagon rings (**Site 1**, fig. 4.14a, 4.14b and **Site 6**, fig. 4.14k, 4.14l), one site above a dangling hydrogen (**Site 2**, fig. 4.14c, 4.14d) another above the surface oxygen (**Site 4**, fig. 4.14g, 4.14h) and two sites between surface oxygens and dangling hydrogens (**Site 3**, fig. 4.14e, 4.14f and **Site 5**, fig. 4.14i, 4.14j).

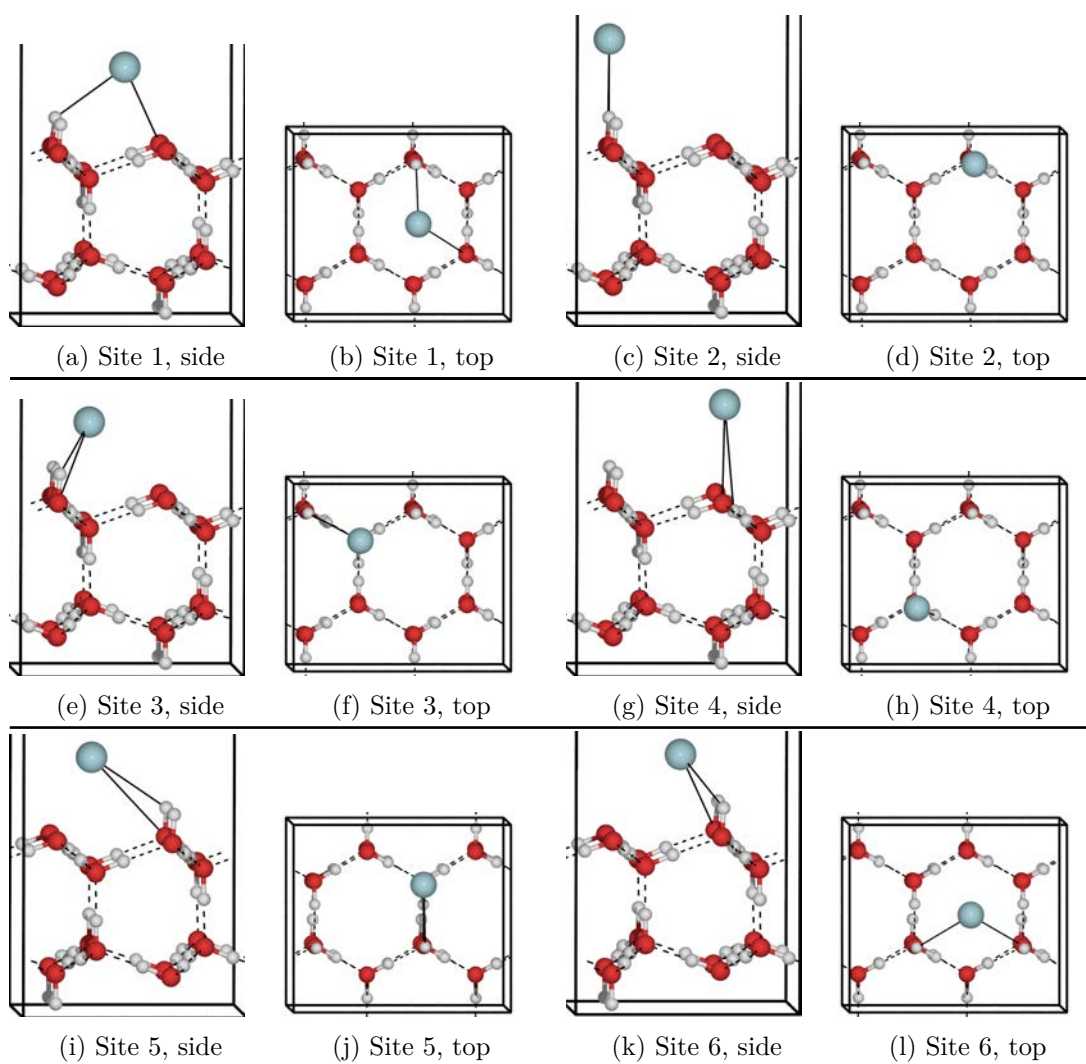


Figure 4.14 – Noble gas adsorption sites on ice I_h basal plane. Solid line indicates closest hydrogen and oxygen atoms.

4.3.3 Convergence against cell dimensions

To test the convergence of adsorption energy and identify the minimum required surface model parameters, a series of tests were performed on the cell dimensions and the number of ice bilayers with Kr adsorbed on sites 1, 3 and 5 (fig. 4.14b, 4.14f, 4.14j).

4.3.3 a Interadsorbate distance

Since the objective of this study is to derive the adsorption energies of isolated atoms on the ice, it is necessary to identify the minimum interadsorbate distance at which the adsorbate-adsorbate interaction may be neglected. To determine this distance, a series of calculations with noble gas dimers was performed. A big (10x10x20Å) unit cell was set up, containing two identical noble gas atoms, placed at fixed distances apart, with the center of mass in the middle of the cell. The interatomic distance in the dimer was varied up to 10Å, that is the maximum distance possible in the defined cell. The resulting interaction energy as a function of interatomic distance is presented on Figure 4.15. The dimer interaction energy $E_{dim}(d)$ is calculated here as a difference of interaction energies at a fixed interatomic distance d $E_{tot}(d)$ and $E_{tot}(d_{max})$ (4.1)

$$E_{dim}(d) = E_{tot}(d) - E_{tot}(d_{max}) \quad (4.1)$$

where d_{max} is the maximum possible interatomic distance in the given cell.

As one may see, the interaction energy becomes negligible at distances above 7Å, permitting to use the 2x1 ice slab with lateral dimensions of 8.66x7.50Å, with the interadsorbate distance of 7.50Å.

To ensure that the cell size taken for this test was sufficient, a supplementary calculation for the Xe dimer in a 15x15x30Å cell was performed (black circles on fig. 4.15). No difference was identified neither in energies nor in the equilibrium position.

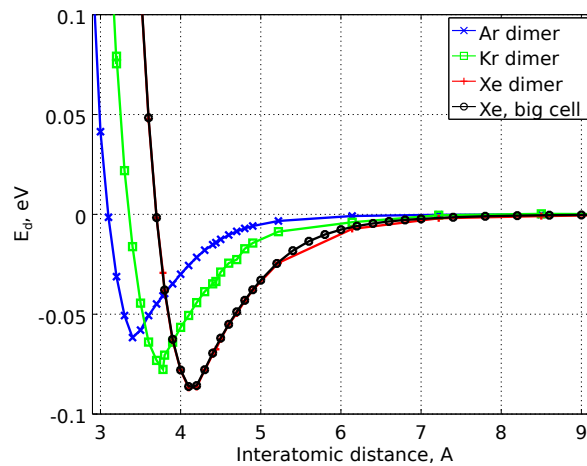


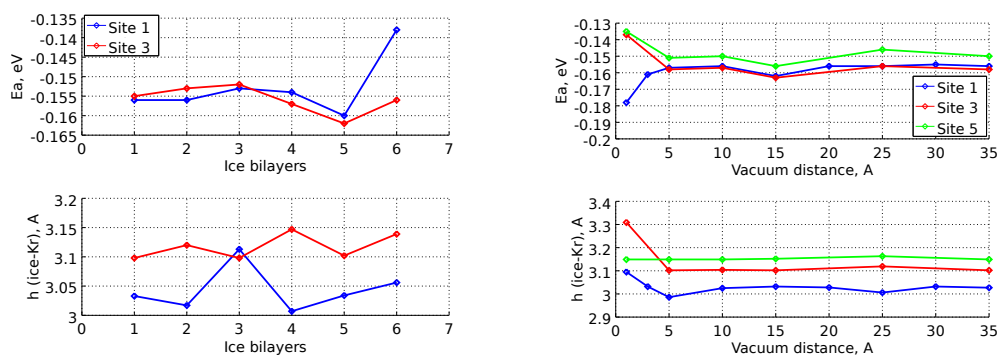
Figure 4.15 – Ar₂, Kr₂, Xe₂ dimer energy as a function of interatomic distance. Unit cell: 10x10x20Å; 3x3x3 K-points; plane wave energy cut-off 400 meV.

4.3.3 b Number of surface layers

As a next step, the required number of ice substrate bilayers was determined. The calculation was performed in a cell with a huge (40Å) vacuum size (fig. 4.16a). For that purpose, the Krypton adsorption energies were calculated for sites 1 (fig. 4.14a, 4.14b) and 3 (fig. 4.14e, 4.14f) on different slabs (1 to 6 BL of ice).

For slabs thicker than 2BL, the topmost ice layer was set free to relax to the energy minimum, all underlying layers being kept frozen to simulate the ice bulk. No visible difference in adsorption energy was observed for slabs from one to three layers thick. The calculated value of the adsorption energy diverges for thick slabs due to increasing uncertainty in the optimization procedure.

Hereafter, all calculations were performed on 2BL slab for adsorption (sect. 4.3.4) and 4BL slab for substitution/inclusion in the bulk (sect. 4.3.5, 4.3.6).



(a) Convergence against number of layers.
30Å vacuum, cell 8.66x7.49x46 Å

(b) Convergence against vacuum distance.
2BL ice, cell 8.66x7.49x(7+zVac) Å

Figure 4.16 – Kr on ice basal plane, convergence tests against slab thickness and vacuum size.

4.3.3 c Vacuum size

Finally the convergence against the vacuum size was tested. A set of cells was set up, with two bilayers of the hexagonal ice and a variable vacuum dimension.

Three different adsorption sites of Kr on ice basal plane were probed: **Site 1**, fig. 4.14a, 4.14b, **Site 3**, fig. 4.14e, 4.14f and **Site 5**, fig. 4.14i, 4.14j.

For each vacuum size three calculations, including slab, adsorbate and slab+adsorbate systems energy were performed. The resulting adsorption energies as a function of vacuum size are presented on Figure 4.16b. One may see that for atomic adsorbates even 5 Angstroms of vacuum dimension is sufficient. Nevertheless, all further calculations were performed using cells with vacuum size of at least 10Å.

4.3.4 Adsorption

Adsorption energies were calculated on the slab model of the basal plane of the hexagonal ice surface, containing two bilayers of water molecules (16 water molecules per cell, fig. 4.14).

The cell of 8.66x7.49x17Å was used, with vacuum dimension of 10.5Å. A gamma-centered mesh of 3x3x1 k-points was used. All calculations were performed with the plane wave energy cut-off of 400eV. Grimme correction [28] is routinely employed to improve the description of Van der Waals interactions.

A summary of obtained adsorption energies is presented in the Table 4.4.

Site	Ar E_a , eV	Kr E_a , eV	Xe E_a , eV
1	-0,116	-0,146	-0,176
2	-0,085	-0,101	-0,135
3	-0,116	-0,149	-0,181
4	-0,066	-0,097	-0,101
5	-0,110	-0,139	-0,168
6	-0,119	-0,153	-0,187

Table 4.4 – Noble gas adsorption energies on water ice.

All adsorption sites are found to be stable, giving a distribution of adsorption energies. Two classes of sites are observed: strongly bound, e.g. site 1, site 3 and site 6, where adsorbate atom is adjacent to several surface water molecules, and weakly-bound, where the adsorbate atom is above a surface hydrogen (site 2) or oxygen (site 4) site. One may also note that the surface-adsorbate distance (Table 4.5) is smaller for strongly-bound sites.

Site	Ar h, Å	Kr h, Å	Xe h, Å
1	3,16	3,13	3,21
2	4,09	4,12	4,24
3	3,10	3,13	3,34
4	3,67	3,81	3,87
5	3,16	3,16	3,25
6	3,15	3,11	3,20

Table 4.5 – Adsorbate height above the surface (average z(O) coordinate)

A summary of the adsorption energies and the surface-adsorbate distances is also shown on Figure 4.17 for clarity.

To conclude, a distribution of adsorption energies is found. The difference between the adsorption energies of the weakest and the strongest sites may serve as an estimate of the barrier height for noble gas diffusion on the surface.

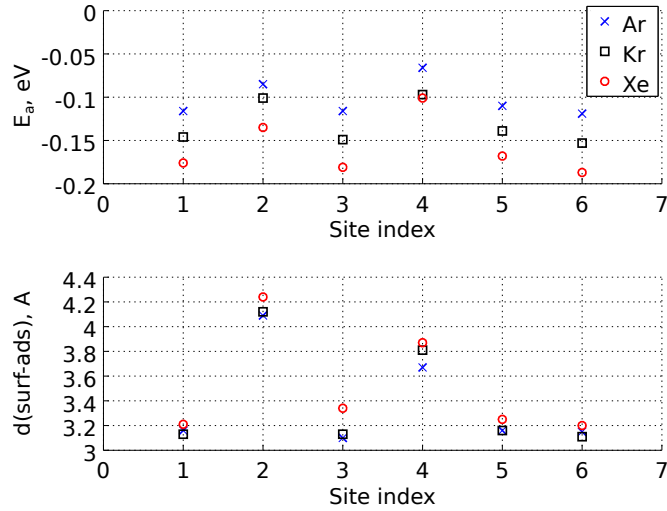


Figure 4.17 – Ar, Kr, Xe adsorption on hexagonal ice basal plane: (top) adsorption energies; (bottom) surface-adsorbate distances.

4.3.5 Substitution

Another point of interest is whether substituting the ice water molecules by noble gas atoms would lead to a stable configuration. To investigate this, a thick (4BL) basal slab model of hexagonal ice was taken. The vacuum size of 10Å was used, giving the cell dimensions of 8.66x7.49x22Å. Two bottom layers of ice were constrained and superior layers were left free to relax.

In that model one may identify four distinct surface water molecules positions (fig. 4.18), referred later Sub(1-4)

Those four water molecules were replaced one by one with noble gas atoms. The substitution energy E_s was calculated in a similar way to the adsorption energy:

$$E_s = E_{tot} - (E_{slab-H_2O} + E_{ads})$$

where E_{tot} is the total energy of the system with a water molecule replaced by a noble gas atom; E_{slab-H_2O} is the total energy of the slab with one water molecule extracted.

A summary of the substitution energies is given in the Table 4.6. The corresponding positions relative to the superior layer of water molecules are presented in Table 4.7.

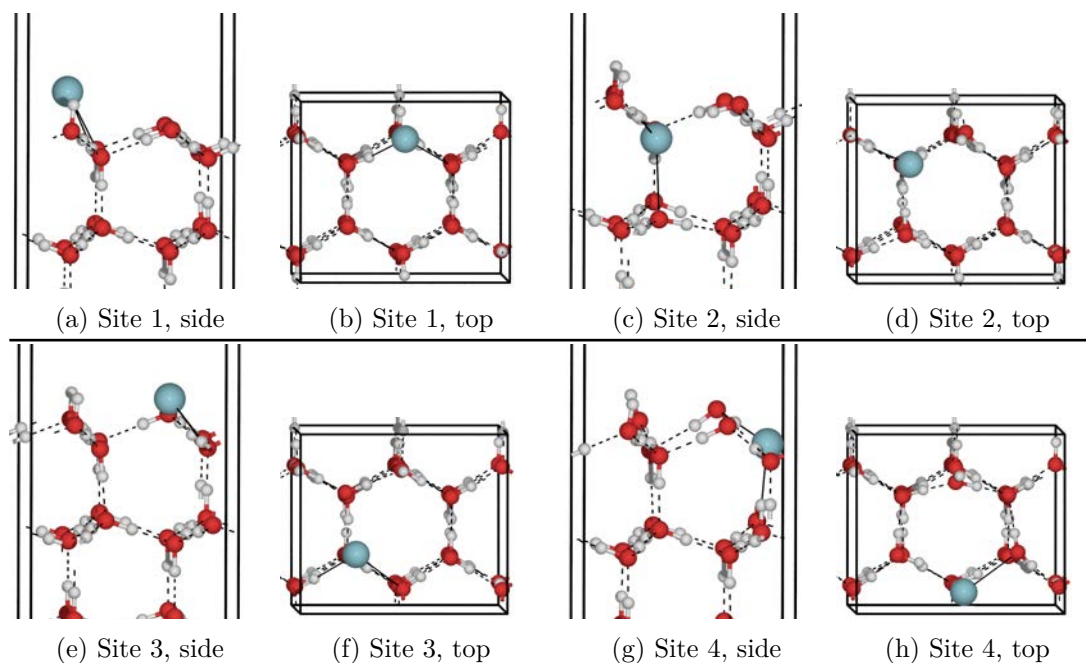
Two possible scenarios may be identified. a) the noble gas atom stays below the surface, deforming the superior ice layer. Although this configuration is stable, it is energetically unfavourable (positive values of E_s). This is the case for sub2 site for all noble gas atoms and sub4 site for Argon. b) the noble gas atom pops out from the surface. The ice surface is reconstructed in some way. Such configurations are stable and energetically favorable, being the equivalent of adsorption on the ice defect sites.

Another point to investigate was to verify if we may stabilize a noble gas atom if we remove more (e.g. two) adjacent water molecules of the ice bulk. For the case of Argon, for example, it was found that there exists at least one (Sub23) configuration where substitution (inclusion in the cavity) becomes energetically favorable. Refer to

Site	Ar E_s , eV	Kr E_s , eV	Xe E_s , eV
Sub 1	-0,093	-0,134	-0,168
Sub 2	0,538	0,245	0,196
Sub 3	-0,105	-0,144	-0,182
Sub 4	0,208	-0,094	-0,136
Sub 12	0,243		
Sub 23	-0,060		
Sub 34	0,004		

Table 4.6 – Noble gas substitution energies in water ice.

Site	Ar h, A	Kr h, A	Xe h, A
Sub 1	2,12	2,42	2,57
Sub 2	-0,89	-0,26	-0,46
Sub 3	1,95	2,25	2,37
Sub 4	-0,23	1,30	1,65

Table 4.7 – Noble gas atom height relative to the surface (average $z(\text{O})$ coordinate), substitution sitesFigure 4.18 – Noble gas substitution sites on ice I_h basal plane. Solid line indicates closest hydrogen and oxygen atoms.

the Table 4.6), sites **Sub12**, **Sub23**, **Sub34**.

It may be concluded that noble gas atoms may be contained within the ice bulk, but only if pores or crystalline structure defects are sufficiently big.

4.3.6 Inclusion

Finally, inclusion in the ice structure was studied (fig. 4.19). The ice model and cell dimensions were the same as for substitution calculations (sect. 4.3.5). Noble gas atoms were placed inside the non-modified slab structure between two hexagon centers, surrounded by 12 water molecules. A big energy penalty (see Table 4.8) was found for inclusion in the ice structure. Such energy penalty leads to the conclusion that noble gas atoms will not penetrate the ice structure, nor diffuse within. Diffusion will be possible only through sufficiently large pores, and not through the ice bulk.

Site	Ar E_i , eV	Kr E_i , eV	Xe E_i , eV
Inc12	0,284	0,543	1,115
Inc23	0,360	0,711	1,353

Table 4.8 – Noble gas inclusion energies in water ice.

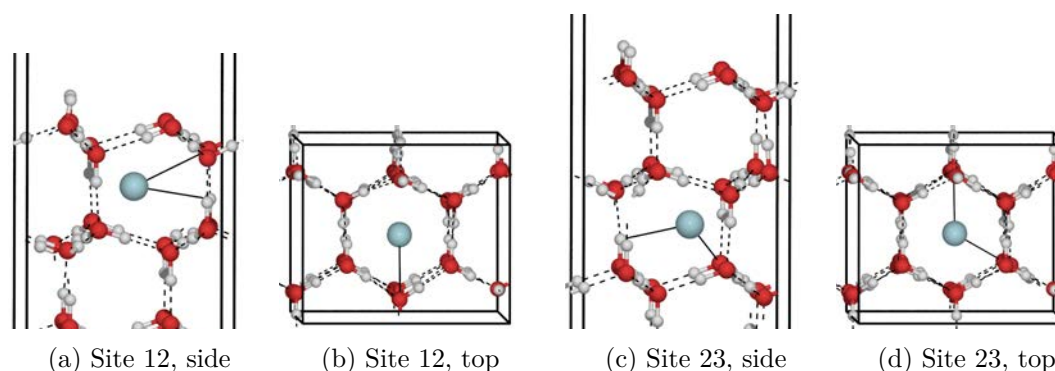


Figure 4.19 – Noble gas inclusion sites in ice I_h basal slab. Solid line indicates closest hydrogen and oxygen atoms.

4.4 Comparisons and conclusions

In this chapter, the adsorption of noble gas atoms (Ar, Kr and Xe) onto water ice surfaces has been studied, both theoretically and experimentally. Theoretical calculations have revealed the existence of 6 adsorption sites, identical for each species, on crystalline ice surface. Each site is associated with an adsorption energy value, which ranges from 66 to 120 meV for Ar, from 100 to 150 meV for Kr and from 100 to 190 meV for Xe. Experiments based on TPD could not access this exact site distribution, mainly because the small energetic difference between the adsorption energies is blurred by the width of the desorption curves. However the experiments gave access to average adsorption energies, which have been evaluated to 75 ± 10 meV for Ar, 130 ± 20

meV for Kr and 170 ± 20 meV for Xe. These values compare well with the theoretical distributions. Note that, because of the TPD technique that is used, warming-up may induce an important diffusion of the noble gas atoms on the surface, that may fall into the most tightly-bound sites prior to their desorption. Therefore the weight of the more bound sites will be enhanced in the mean values that are experimentally derived, which explains why the experimental mean values are found closer to the high energy side of the adsorption sites distribution predicted by the theory. Finally, experimental values for the adsorption energy of Ar on crystalline ice are to be taken with caution, since important diffusion and outgasing from other cold parts of the cryostat during the warming-up have brought polluting signal on the TPD curves that were difficult to estimate and correct.

The theoretical study of the trapping of the noble gas atoms into the ice bulk has revealed that the inclusion of Ar, Kr or Xe in the water ice network is very unlikely. Nevertheless, should the water ice present cavity-like defects (missing molecules in the water ice network), Ar is efficiently trapped and stabilized into these micro-pores. These “cavities” should anyway be at least bigger than a missing water molecule, otherwise the presence of the Ar atom induces a distortion of the ice network which is energetically not favourable. This finding is very interesting since trapping of noble gases in cavities of the water ices may be an alternative candidate to the water ice clathrate organization. Preliminary experimental studies have been realized, in which the trapping of the noble gas has been observed by monitoring TPD curves of the atoms recovered by an increasing thickness of amorphous water layer. Proportions of noble gas trapped into the ice have been estimated. However, the trapping being inversely dependent on the diffusion of the atoms through the ice layer, which is a dynamical effect, studies at fixed temperature (isothermal desorption), and as a function of time, is needed for a better quantification of the trapping. In addition, the presence of closed cavities when water ice is grown on top of rare gas atoms has still to be experimentally evidenced.

To conclude, the study presented here offers an overview of the noble gas adsorption and trapping by water ices. In an astrophysical context, the adsorption energies of Ar, Kr and Xe are found - not surprisingly - weaker than the adsorption energy of ice on ice itself, which makes that the trapping by surface adsorption is not likely to be an efficient process except at very low temperature. But the adsorption energies can be used to estimate the amount and residence time of rare gas atoms on the water ice at any temperature, making possible to test the scenario during which additional water molecules could accrete on top and result in noble gas enrichment within the ice bulk. Our study shows that, if the water which accretes on top presents cavity-like defects, the rare gas atom can get efficiently trapped into the water ice, up to temperature corresponding to the water sublimation. This trapping in the ice cavities is a very interesting effect, since, up to now, such trapping into ice bulks were only considered if the water would organize as clathrates structures [8, 9]. Considering that the mere presence of this water allomorphism in the primitive nebula is still controversial, the trapping in water ice cavities would be potentially a very promising alternative process. Therefore, this work opens the way to an in-depth study of this trapping effect into the water ice, both experimentally and theoretically.

References

- [1] Olivier Mousis, Daniel Gautier, and Dominique Bockelée-Morvan. “An Evolutionary Turbulent Model of Saturn’s Subnebula: Implications for the Origin of the Atmosphere of Titan”. In: *Icarus* 156.1 (2002), pp. 162–175.
- [2] H. B. Niemann et al. “The abundances of constituents of Titan’s atmosphere from the GCMS instrument on the Huygens probe”. en. In: *Nature* 438.7069 (2005), pp. 779–784.
- [3] Yann Alibert, Olivier Mousis, and Willy Benz. “On the Volatile Enrichments and Composition of Jupiter”. en. In: *The Astrophysical Journal Letters* 622.2 (Apr. 2005), p. L145.
- [4] Ronen Jacovi and Akiva Bar-Nun. “Removal of Titan’s noble gases by their trapping in its haze”. In: *Icarus* 196.1 (2008), pp. 302–304.
- [5] D. Cordier et al. “About the Possible Role of Hydrocarbon Lakes in the Origin of Titan’s Noble Gas Atmospheric Depletion”. en. In: *The Astrophysical Journal Letters* 721.2 (Oct. 2010), p. L117.
- [6] John P. Osegovic and Michael D. Max. “Compound clathrate hydrate on Titan’s surface”. en. In: *Journal of Geophysical Research: Planets* 110.E8 (2005), E08004.
- [7] C. Thomas et al. “A theoretical investigation into the trapping of noble gases by clathrates on Titan”. In: *Planetary and Space Science. Surfaces and Atmospheres of the Outer Planets, their Satellites and Ring Systems, Part IV Meetings held in 2007: EGU: PS3.0 & PS3.1; IUGG/IAMAS:JMS12 & JMS13; AOGS: PS09 & PS11; EPSC2: AO4 or PM1* 56.12 (2008), pp. 1607–1617.
- [8] Olivier Mousis et al. “Removal of Titan’s Atmospheric Noble Gases by Their Sequestration in Surface Clathrates”. en. In: *The Astrophysical Journal Letters* 740.1 (Oct. 2011), p. L9.
- [9] Jan Lundell, Arik Cohen, and R. Benny Gerber. “Quantum Chemical Calculations on Novel Molecules from Xenon Insertion into Hydrocarbons”. In: *The Journal of Physical Chemistry A* 106.49 (2002), pp. 11950–11955.
- [10] Antti Lignell et al. “On theoretical predictions of noble-gas hydrides”. In: *The Journal of Chemical Physics* 125.18 (Nov. 2006), p. 184514.
- [11] Jan Lundell et al. “Quantum chemical study of the hydrogen-bonded HXeOH–H₂O complex”. In: *Journal of Molecular Structure. Horizons in Hydrogen Bond Research 2005A Collection of Papers from the XVIth International Conference "Horizons in Hydrogen Bond Research", Roskilde, Denmark, 30 August - 04 September, 2005* 790.1–3 (2006), pp. 31–39.
- [12] O. Mousis et al. “Sequestration of Noble Gases by H₃⁺ in Protoplanetary Disks and Outer Solar System Composition”. en. In: *The Astrophysical Journal* 673.1 (Jan. 2008), p. 637.
- [13] F. Pauzat and Y. Ellinger. “H₃⁺ as a trap for noble gases - 2: structure and energetics of XH₃⁺ complexes from X=neon to xenon”. In: *The Journal of Chemical Physics* 127.1 (July 2007), p. 014308.

- [14] F. Pauzat et al. "H₃⁺ as a trap for noble gases-3: Multiple trapping of neon, argon, and krypton in XnH₃⁺(n=1–3)". In: *The Journal of Chemical Physics* 130.17 (May 2009), p. 174313.
- [15] F. Pauzat et al. "Gas-phase Sequestration of Noble Gases in the Protosolar Nebula: Possible Consequences on the Outer Solar System Composition". en. In: *The Astrophysical Journal* 777.1 (Nov. 2013), p. 29.
- [16] A. Kouchi et al. "Conditions for condensation and preservation of amorphous ice and crystallinity of astrophysical ices". In: *Astronomy and Astrophysics* 290 (1994), pp. 1009–1018.
- [17] A. Gil et al. "Adsorption of Water on Solid Surfaces Studied by Scanning Force Microscopy". In: *Langmuir* 16.11 (2000), pp. 5086–5092.
- [18] A. Givan, A. Loewenschuss, and C. J. Nielsen. "Fourier transform infrared spectrometry studies of surface and bulk porosity of water ice". In: *Vibrational Spectroscopy* 12.1 (1996), pp. 1–14.
- [19] K. Isokoski et al. "Porosity and thermal collapse measurements of H₂O, CH₃OH, CO₂, and H₂O:CO₂ ices". en. In: *Physical Chemistry Chemical Physics* 16.8 (Jan. 2014), pp. 3456–3465.
- [20] P. Jenniskens and D. F. Blake. "Structural transitions in amorphous water ice and astrophysical implications". en. In: *Science* 265.5173 (May 1994), pp. 753–756.
- [21] H. Schlichting and D. Menzel. "Techniques for attainment, control, and calibration of cryogenic temperatures at small single-crystal samples under ultrahigh vacuum". In: *Review of Scientific Instruments* 64.7 (July 1993), pp. 2013–2022.
- [22] J. D. Bernal and R. H. Fowler. "A Theory of Water and Ionic Solution, with Particular Reference to Hydrogen and Hydroxyl Ions". In: *The Journal of Chemical Physics* 1.8 (Aug. 1933), pp. 515–548.
- [23] Ernesto Cota and William G. Hoover. "Computer simulation of hexagonal ice". In: *The Journal of Chemical Physics* 67.8 (Oct. 1977), pp. 3839–3840.
- [24] N. H. Fletcher. "Reconstruction of ice crystal surfaces at low temperatures". In: *Philosophical Magazine Part B* 66.1 (1992), pp. 109–115.
- [25] Ding Pan et al. "Surface energy and surface proton order of the ice Ih basal and prism surfaces". en. In: *Journal of Physics: Condensed Matter* 22.7 (Feb. 2010), p. 074209.
- [26] V. Buch et al. "Proton order in the ice crystal surface". en. In: *Proceedings of the National Academy of Sciences* 105.16 (Apr. 2008), pp. 5969–5974.
- [27] Tomas K. Hirsch and Lars Ojamäe. "Quantum-Chemical and Force-Field Investigations of Ice Ih: Computation of Proton-Ordered Structures and Prediction of Their Lattice Energies". In: *The Journal of Physical Chemistry B* 108.40 (2004), pp. 15856–15864.
- [28] Stefan Grimme. "Semiempirical GGA-type density functional constructed with a long-range dispersion correction". en. In: *Journal of Computational Chemistry* 27.15 (2006), pp. 1787–1799.

Chapter 5

Adsorption of CH_3CN vs CH_3NC at interstellar grain surfaces

5.1 Study context

Among the ~ 200 molecules detected in the interstellar medium (ISM) gas phase [1], about one fifth consists in nitriles R-CN and isonitrile R-NC isomers. Considering purely organic species, two different families can be identified that cover the two classes of isomers: conjugated molecules in which R contains, or does not contain, a system of bonds that can be delocalized onto the CN triple bond. The first one is known as the cyanopolyne/isocyanopolyne series derived, formally, by adding carbon atoms or C_2 fragments to HCN and HNC; the second one obtained, formally, by replacing the H atom in HCN and HNC by saturated hydrocarbon fragments. The simplest common ancestor of both series is the CN radical, second species ever detected in the ISM [2–4]. About the same time, HCN [5] and CH_3CN [6] were also detected, together with the first cyanopolyne HC_3N [7]. The identification of HNC followed soon after [5, 8]. The corresponding isonitrile CH_3NC was detected 13 years later [9] towards Sgr B2 and it took twenty five more years to confirm the presence of this species in the Horsehead PDR [10].

The abundance ratios between nitrile and iso nitrile isomers have been largely used to constrain the chemical models proposed to account for their presence in the various objects in which they were observed. The HCN/HNC couple has been the most studied since, according to radioastronomy gas phase observations, its abundance ratio varies over a large range, namely, from values close to unity in cold molecular clouds [11–13] to several thousands in highly illuminated PDRs [14]. By contrast, the $\text{CH}_3\text{CN}/\text{CH}_3\text{NC}$ abundance ratio of ~ 50 appears remarkably even [9, 11, 15].

In a previous work, a systematic study was carried out devoted to determine the energetics of 32 isomeric structures identified in various types of objects. The overall result was rather unexpected in the sense that, on average, the most abundant isomer was the most stable and that the abundances of the other isomers were decreasing with the order up the energy scale. It is referred as the Minimum Energy Principle (MEP). For more details see [16] and references therein.

Although it is not clear yet why the MEP works in the interstellar medium (ISM),

which makes it a debated concept due to a number of exceptions already pointed out in the original presentation [16], it has shown a notable predictive power [17]. For example, glycine, that is not the most stable isomer in its family [18] was said difficult to be detected. Based on the MEP, it was also predicted that acetamide and formamide being the most stable isomers in their respective families [17] should be more suited to radio detection. The latter prediction has been confirmed by the recent identification of formamide in a dozen sources [19, 20].

In this context, where HCN is more stable than HNC by ~ 15 kcal/mol and CH_3CN more stable than CH_3NC by ~ 24 kcal/mol the MEP would be verified for the latter couple of isomers but only partially for the first one. However, it should not be forgotten that radio observations are blind to molecules depleted on the grains, and that gas phase chemistry alone cannot account for the abundances of complex organic molecules formed in the ISM. Solid-gas reactions, and even chemical processes involving adsorbed partners, have to be considered, making adsorption energies a key factor for the determination of real abundances and abundance ratios.

Among the various grain models originally proposed [21] such as ices and/or carbonaceous coatings on refractory minerals we selected three components, identified according to the environment by means of Mid-IR spectroscopy, namely, polycyclic aromatic hydrocarbon (PAH) molecules that are present in the spectra of almost all objects [23, 24], silicates [25] and water ices [26–29] that appear chemically relevant to the distribution of the species between the gas phase and the grains.

In the next pages is presented a research focused on the determination of the adsorption energies of the first members of the nitrile and isonitrile families on laboratory analogues of widespread grain surfaces, namely, water ice, highly oriented pyrolytic graphite (HOPG) and silica. It should be noted that we are not concerned here by the possible role of the grain surfaces in the formation of CH_3CN and CH_3NC .

5.2 Experimental approach

5.2.1 Pure thick ices of CH_3CN and CH_3NC

Before studying adsorption and desorption of CH_3CN and CH_3NC from different surfaces, it is important to study these two species as pure ices. For both isomers, the mass signal associated with the ionization of the intact molecule ($\text{C}_2\text{H}_3\text{N}^+$, $m = 41$ amu) has been chosen for both adsorbate deposition and TPD experiments. The two species present comparable mass spectra following electron-induced ionization at 90 eV [30] making mass spectrometry unable to distinguish unambiguously the two isomers. This could potentially represent an important issue, in particular for CH_3NC . This molecule, in its liquid form is much less stable than its isomer CH_3CN . It was specifically prepared by J.-C. Guillemin for this study and had to be kept at low temperature ($< 273\text{K}$) and protected from light.

It is therefore important to verify whether the product we introduce in the vacuum chamber is solely CH_3NC or if the molecule has been degraded or isomerized to CH_3CN , CH_2CNH or CH_2NCH during the deposition or the warming-up. To this purpose, Fourier Transform Reflection-Absorption InfraRed Spectroscopy (FT-RAIRS) has been systematically done on the CH_3CN and CH_3NC ices after their growth and during the

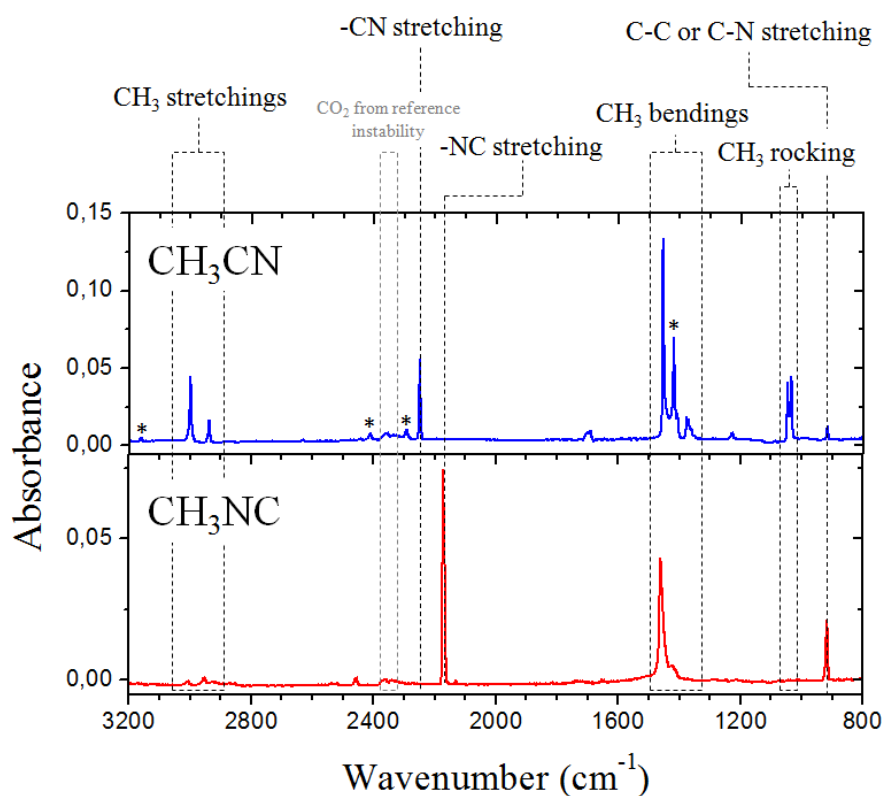


Figure 5.1 – Reflection-absorption infrared spectra of thick CH_3CN ice (850 ML - upper panel) and of thick CH_3NC ice (890 ML - lower panel), condensed at 90 K on polycrystalline gold. Indicated assignments are detailed in Figure 5.1. Peaks marked with (*) correspond to identified combination modes. Structures observed at $\sim 2350\text{ cm}^{-1}$ are associated with a modification of the reference spectra due to a change of gaseous CO_2 concentration in the spectrometer during the experiment time.

Table 5.1 – vibration wavenumbers (in cm⁻¹) and mode assignments of gas phase and physisorbed multilayers of CH₃CN and CH₃NC in the 800 - 3200 cm⁻¹ range.

Acetonitrile CH ₃ CN			Methyl isocyanide CH ₃ NC			Assignment
Gas ^a	Solid ^b	This work	Gas ^c	Solid ^d	This work	
3178	3161	3163	-	-	-	$\nu(-C\equiv N) + \nu(C-C)$
3009	3002	3000	3014	no	3008	$\nu_{as}(\text{CH}_3)$
2954	2941	2939	2966	no	2953	$\nu_s(\text{CH}_3)$
2417	2415	2411	-	-	-	$\delta_s(\text{CH}_3) + \rho(\text{CH}_3)$
2305	2289	2293	-	-	-	$\delta_s(\text{CH}_3) + \nu(C-C)$
2266	2250	2251	-	-	-	$\nu(-C\equiv N)$
-	-	-	2166	2170	2172	$\nu(-N\equiv C)$
1448	1455	1455	1467	1470	1459	$\delta_{as}(\text{CH}_3)$
1410	1422	1419	-	-	-	$\rho(\text{CH}_3) + \delta(C-C\equiv N)$
1390	1378	1378	1429	no	1426	$\delta_s(\text{CH}_3)$
1041	1038	1036	1129	no	no	$\rho(\text{CH}_3)$
-	-	-	945	no	918	$\nu(C-N)$
920	no	917	-	-	-	$\nu(C-C)$

^a, ^b, ^c and ^d are from Parker et al., Schaff et al., [30] and Murphy et al. respectively; ν stands for stretching mode, δ for bending mode, ρ for rocking mode, $_{as}$ for asymmetric mode and $_s$ for symmetric mode; “no” indicates non-observed vibrations.

warming-up.

IR spectra of thick ices (~ 800 ML) of pure CH₃CN (upper panel) and pure CH₃NC (lower panel), deposited on polycrystalline gold at 90 K are presented in Figure 5.1. Infrared spectra have been realized with a resolution of 2 cm⁻¹. In the case of condensed multilayer of acetonitrile, we obtain IR spectrum very similar to what has been found by Schaff and Roberts[32]. The more intense peaks are associated with normal vibration modes of the condensed molecules, while many less intense peaks are related to combination modes, marked in Figure 5.1. Less literature is available on infrared spectroscopy of condensed methyl isocyanide at low temperatures. Vibrational study of condensed CH₃NC in the 1000 - 2500 cm⁻¹ range [33] and gas phase spectroscopy values have been used for the assignment of CH₃NC IR peaks. The assignment we propose for the observed vibrational peaks are summarized in Table 5.1.

In the case of condensed methylisocyanide ice, all the peaks are attributed to a given CH₃NC vibration, therefore confirming the purity of the deposited ice. The clear difference in the stretching vibrations of the cyanide (2250 cm⁻¹) and isocyanide (2170 cm⁻¹) groups makes that the two isomers can be finely differentiated by infrared spectroscopy. The spectra in Figure 5.1 show no contribution of the other isomer in each pure ice. This is still true during warming-up and desorption of the ices, demonstrating that the mass signal monitored from pure isomer ices will not be polluted in-situ by any isomerization process during the TPD experiment.

Thermal desorption of the pure ices of each isomer has been realized in order to extract the relevant adsorption energy and prefactor of the Polanyi-Wigner law. Thermal

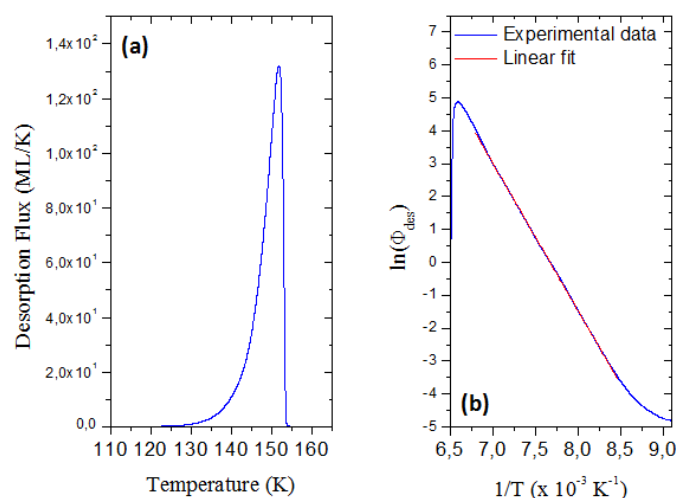


Figure 5.2 – (a) TPD curve, with a heating rate of 2 K/min, of ~ 800 ML of pure CH_3CN deposited on polycrystalline gold at 90 K. (b) Plot of the logarithm of the desorption flux as a function of the inverse temperature. Red line is a linear regression of the plot.

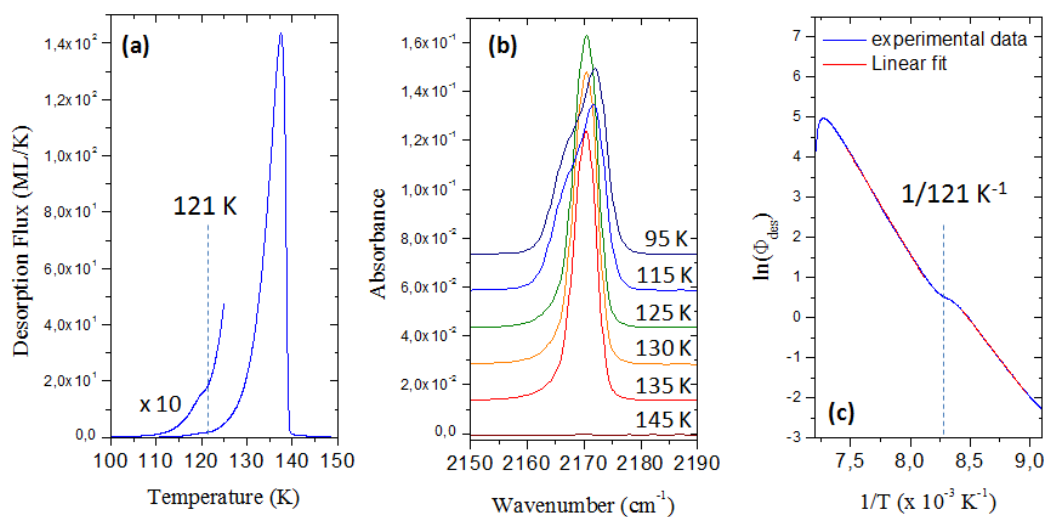


Figure 5.3 – (a) TPD curve, with a heating rate of 2 K/min, of ~ 800 ML of pure CH_3NC deposited on polycrystalline gold at 90 K. The beginning of the desorption as been magnified by a factor of 10 (b) Infrared spectra in the region of the NC stretching vibration, during the warming-up of the ice. (c) Plot of the logarithm of the desorption flux as a function of the inverse temperature. Lines are linear regressions of the plot.

desorption curves of multilayers of pure CH₃NC and pure CH₃CN on polycrystalline gold, using a heating rate of 2 K/min, are shown in Figures 5.3a and 5.2a respectively. The multilayer desorption of CH₃NC presents a small shoulder at 121 K, which we attribute to a temperature-induced phase transition of the solid. This kind of phase transition from a disordered to a more structured solid is observed in several pure ices, the most famous case being the water ice crystallization at ~ 150 K. The shoulder in the desorption curves is explained by different adsorption energies for each phase, with a higher value for the most ordered phase in which molecules are usually more coordinated. The desorption of the disordered phase competes with its crystallization during the warming-up, and the total desorption flux observed is then the superposition of the desorption of the disordered and the crystalline phases [34]. This hypothesis is supported by the infrared follow-up of the NC stretching mode during the warmup, as shown in Figure 5.3b. Between 115 and 125 K, the vibrational peak gets narrower and more intense, whereas the amount of adsorbed molecules diminishes. This suggests a change of the local environment of the adsorbate, which modifies the dipole moment associated with the NC stretching vibration together with its bond-strength. Such change is usually induced by a reorganization of the molecules in the solid, as it has already been highlighted in the case of the CO stretching modes in solid CH₃COOH and HCOOCH₃ [35, 36] or OH stretching modes in solid water [37]. Interestingly, no phase transition was observed in solid CH₃CN, neither in the TPD curves nor in the infrared spectra.

The adsorption energy of the multilayers of CH₃CN and CH₃NC can be derived from the TPD curves by considering that the desorption of the thick ices follows a zeroth order kinetic Polanyi-Wigner law. For this purpose the zero order kinetics Polanyi-Wigner equation (5.1) is used.

$$\ln(\Phi_{des}) = -\frac{E_{ads}}{k} \frac{1}{T} + \ln\left(\frac{\nu}{\beta}\right) \quad (5.1)$$

Plotting the logarithm of the flux against the inverse temperature $1/T$ results in a linear behavior, in which the adsorption energy and prefactor can be derived from the slope and intercept respectively (see chapter 2.3.2 for details). This linear trend is observed for CH₃NC and CH₃CN (Figures 5.3c and 5.2b). In the case of CH₃NC, the plot consists of two different linear regimes, each being associated with a different adsorption energy for the solid CH₃NC, which further confirms the hypothesis of a phase transition at 121 K. From linear fitting of the plots we find for CH₃CN multilayer $E_{ads} = 390 \pm 10$ meV and $\nu = 10^{13 \pm 0.5}$ s⁻¹. For CH₃NC we find $E_{ads} = 330 \pm 10$ meV and $\nu = 5 \times 10^{12 \pm 0.5}$ s⁻¹ for the disordered phase and $E_{ads} = 420 \pm 10$ meV and $\nu = 5 \times 10^{16 \pm 0.5}$ s⁻¹ for the crystalline phase.

5.2.2 Submonolayer of CH₃CN and CH₃NC on model surfaces

Desorption of monolayer and submonolayer coverages of CH₃NC and CH₃CN has been studied on Quartz- α (0001), HOPG and compact amorphous and crystalline water ices, in order to obtain the adsorption energy of these isomers on the different substrates.

The associated TPD curves, realized with a heating rate of 12 K/min for graphite and quartz substrates and 10 K/min in the case of adsorption on water ices are shown

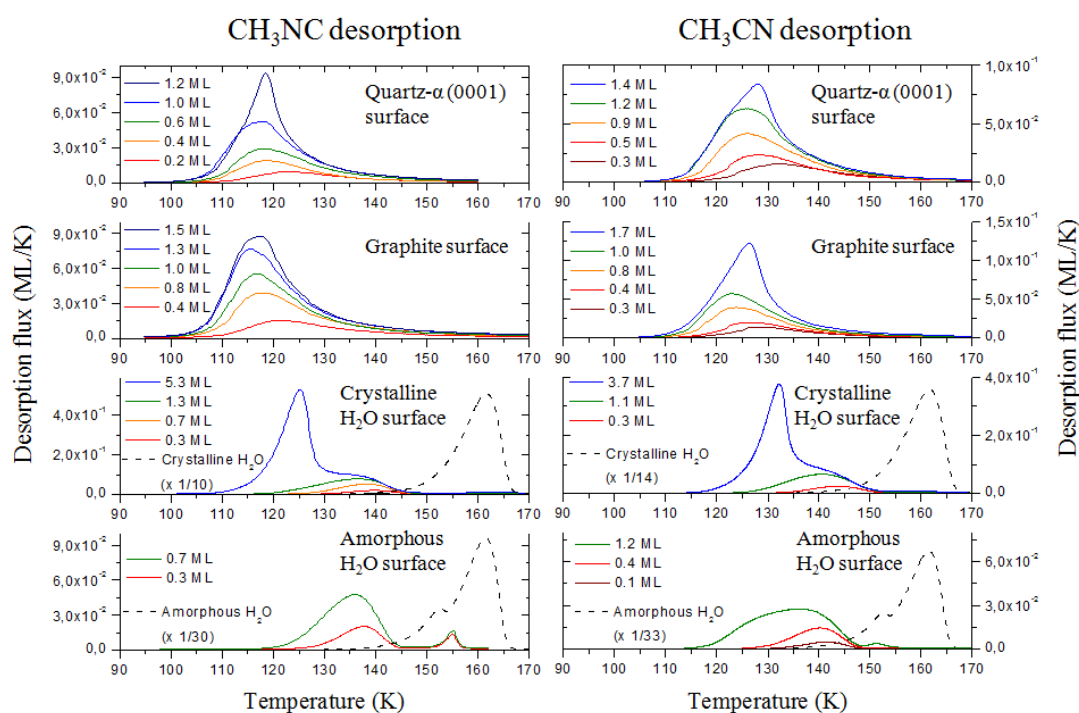


Figure 5.4 – : TPD curves of several initial coverages of CH_3NC (left) and CH_3CN (right) adsorbed on quartz- α (0001) surface, on HOPG surface, and on crystalline and compact amorphous water ice surfaces. Applied heating rates are 12 K/min on graphite and quartz, and 10 K/min on water surfaces. TPD curves of multilayers (~ 100 ML) of crystalline and amorphous water ices are shown in dashed lines to indicate the ice sublimation onset.

in Figure 5.4. The coverages indicated in the figure have been calibrated for each surface. On the water ice surfaces, two desorption peaks can be observed. One at lower temperature is observed only for high exposures, and therefore is related to the multilayer desorption. The second peak at higher temperatures is associated with the desorption of the first monolayer, for which the adsorption energy is very different from that of the multilayer. The area of this second peak, when saturated, gives the absolute calibration for 1 ML. Finally, a weak desorption feature is seen at ~ 155 K only in the case of adsorbates on compact amorphous water. This temperature corresponds to the supporting water ice crystallization, evidenced by a shoulder in the amorphous water TPD curve (dashed line). This peak is attributed to the phenomenon known as volcano desorption: some adsorbates remain trapped in corrugations of the amorphous water ice, and are suddenly released when crystallization of the water ice takes place [38, 39]. However, this contribution remains weak as the signal is dominated by the surface monolayer desorption. In the case of desorption from graphite or quartz surfaces, only one desorption feature is observed, meaning that the adsorption energy of the first layer and of the multilayer are not different enough to result in a clear separation of desorption peaks. The transition between multilayer and monolayer adsorption can anyway be determined by observing a change in the desorption kinetics order from the zero to the first order with lower exposure. This transition allows for identifying the full monolayer coverage with a relative precision of the order of 10% (see chapter 2.3.1).

In order to derive the adsorption energies of each isomer from these surfaces, we use a method described in detail in chapter 2.3.3. The desorption of the submonolayer coverage of molecules from the substrate is modeled using a first order approximation of the Polanyi-Wigner law. In order to get a more accurate description of the desorption, a distribution of adsorption energies is considered instead of a single value. Such an approach implicitly takes into account different adsorption geometries and sites, as well as the surface defects.

The experimental desorption curves are then fitted using the following equation:

$$\Phi_{des}(T) = \frac{\nu}{\beta} \sum_i \theta_i(T) \exp\left(-\frac{E_i}{kT}\right)$$

where E_i is the adsorption energy associated with site i and θ_i is the coverage of the molecules for site i . In this case, the approximation of a constant prefactor ν is made, i.e. it does not depend on the adsorption site. The TPD curves obtained experimentally are fitted with this law using a simple sampling of the adsorption energy in the 350 - 550 meV range, with the only free parameter being the initial coverage θ_{0i} of each site i . The result gives the fraction of initial molecules adsorbed with the adsorption energy E_i , which is the adsorption energy distribution on the surface for a given total initial coverage θ_0 .

The search for the prefactor is illustrated in Figure 5.5 for the case of CH_3CN desorption from the HOPG surface. The algorithm for the prefactor search is described in details in sections 2.3.3 a and 2.3.3 b.

Once the prefactor value is obtained, a distribution of adsorption energies may be derived from each of the desorption curves. Resulting adsorption energy distributions are shown in Figure 5.6 for different initial coverages of each isomer adsorbed on the four substrates.

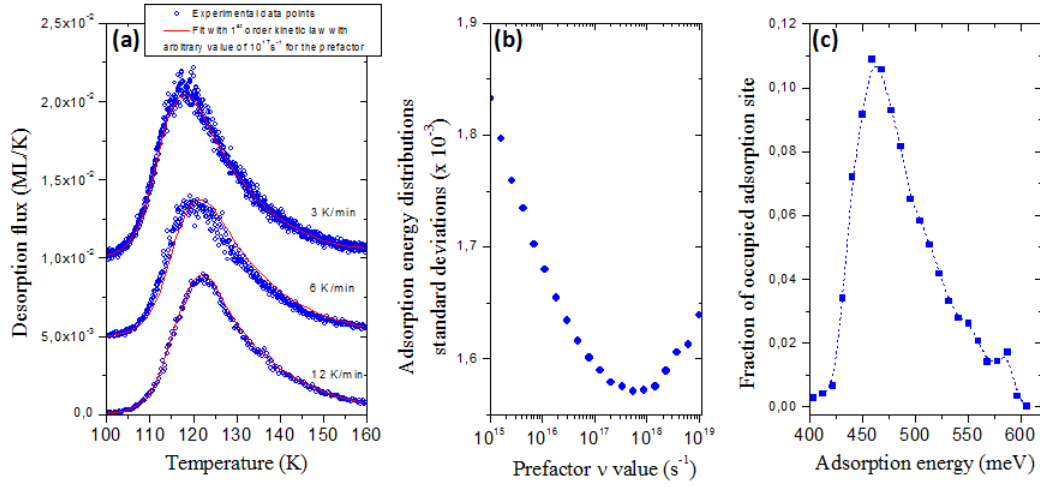


Figure 5.5 – (a) Set of TPD curves of 0.2 ML of CH₃CN adsorbed on HOPG realized at 3 K/min, 6 K/min and 12 K/min. Straight lines are the fit of these data using a first order kinetic Polanyi-Wigner law with a distribution of adsorption sites using a prefactor of 10¹⁷ s⁻¹. (b) Search for the best value for the prefactor ν : plot of the standard deviation of the three minimum occupied adsorption energy as extracted from the fits of the three TPD curves. The minimum of the curve give the best choice for ν . (c) Adsorption energy distribution corresponding to 0.2 ML of CH₃CN on HOPG using the best choice for the prefactor. Fraction of the site occupation is determined as the number of molecules with the adsorption energy E_i normalized to the total amount of initial molecules.

Table 5.2 – Desorption prefactor ν , most probable adsorption energy E_a and size of the adsorption energy distribution δE_a taken as the full width at half maximum, for CH₃CN and CH₃NC adsorbed on Quartz- α (0001), HOPG and crystalline or compact amorphous water ice surfaces. Distinction is made between adsorption energy at high coverage (0.7 - 1 ML) and low coverage (< 0.3 ML).

Substrates	Adsorbate	ν (s ⁻¹)	E_{ads} (meV)		δE_{ads} (meV)	
			~0.7ML	<0.3ML	~0.7ML	<0.3ML
Quartz- α (0001)	CH ₃ NC	$3 \times 10^{17 \pm 0.5}$	430	460	50	70
	CH ₃ CN	$1 \times 10^{17 \pm 0.5}$	460	495	60	75
HOPG	CH ₃ NC	$2 \times 10^{16 \pm 0.5}$	430	460	50	80
	CH ₃ CN	$8 \times 10^{17 \pm 0.5}$	440	460	50	65
Crystalline water ice	CH ₃ NC	$1 \times 10^{18 \pm 0.5}$	540*	550*	30	25
	CH ₃ CN	$1 \times 10^{18 \pm 0.5}$	565*	570*	50	35
Amorphous water ice	CH ₃ NC	$5 \times 10^{16 \pm 0.5}$	490*	490*	25	20
	CH ₃ CN	$2 \times 10^{17 \pm 0.5}$	-	530*	-	30

Values marked * should be considered with caution since the sublimation of the supporting water ice layer plays an important role in the observed desorption features.

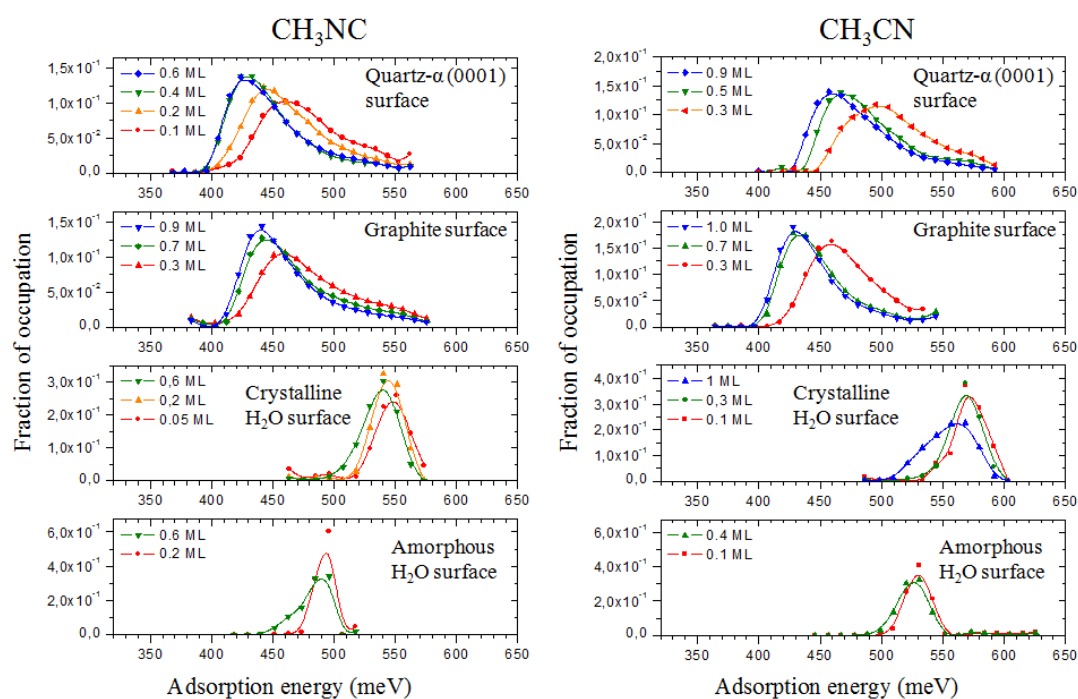


Figure 5.6 – Adsorption energy distributions for several initial submonolayer coverages of CH_3NC (left) and CH_3CN (right) adsorbed on quartz- α (0001), HOPG, crystalline water and compact amorphous water surfaces.

In Table 5.2 are summarized for each adsorbate and each substrate the value of the prefactor, the most probable adsorption energy (taken as the maximum of the corresponding distributions) and the size of the distributions defined as the width at half maximum. From these values, a first conclusion is that, whatever the substrate, the adsorption energy of acetonitrile is found higher than that of methyl isocyanide. In the case of adsorption on graphite, though, the difference is small and close to our experimental error bars. Desorption from HOPG and quartz on the one hand, and from water surfaces on the other hand, show different behaviors, that will be discussed hereafter.

In any case, adsorption on the quartz substrates is found stronger than on graphite. However, the adsorption and thermal desorption of both isomers on Graphite and Quartz exhibit similar trends. Two regimes can be distinguished in these cases. For initial coverage above 0.5 ML, the adsorption energy distribution seems weakly dependent on the initial coverage. For initial coverage below 0.3 ML, the adsorption energy distribution significantly shifts toward higher energies with decreasing coverage. Indeed, at lower coverage, the molecules may diffuse during the warming-up and fall in the tightly bounded adsorption sites. At higher coverage, all these sites being populated, less bound sites will be probed by the excess molecules. Experiments performed at very low coverage therefore enhance the role of the most bounded sites (probably, defect sites) in the adsorption energy distribution. For being properly understood, this effect needs support from theoretical calculations, and will be further discussed in the section 5.3.1.

In the case of adsorption on water ices, conclusions are not straightforward, and the results obtained should be considered with caution. First, the adsorption energy on crystalline ice is, for both isomers, found higher than in the case of adsorption on amorphous ice. At first sight this is surprising since the amorphous water surface is expected to present more different available adsorption sites than the crystalline surface. However, it can be understood as follows: the adsorption energies of $\text{CH}_3\text{CN}/\text{CH}_3\text{NC}$ determined from the data treatment are very close to the adsorption energy of the underneath water ice itself, whose desorption has already started when the monolayer desorption of $\text{CH}_3\text{CN}/\text{CH}_3\text{NC}$ is observed. The desorption energy of amorphous water is of 490 meV and that of crystalline water is found within 500-520 meV [34, 40]. Those values are very similar to the adsorption energy obtained in this study for CH_3NC adsorption on water. Thus, the desorption observed for CH_3CN and CH_3NC is, at least partly, due to the desorption of the supporting water ice. Therefore the values that are obtained here for the adsorption energies do not reflect the real interaction strength of the $\text{CH}_3\text{CN}/\text{CH}_3\text{NC}$ molecules with the water ice surface, but suggest a lower limit for it instead. However, a difference is still found between CH_3CN and CH_3NC adsorption energies, which would not be the case if their desorptions were only due to the water sublimation. In particular, the adsorption energies for CH_3CN on water is found higher than that of water on water ice itself. Thus, the interaction of the methyl cyanide and the acetonitrile with water also plays a role in the measured adsorption energies, and CH_3CN is bound with a higher energy to the amorphous or crystalline water surface than CH_3NC .

5.3 Theoretical approach to adsorption energies

To determine the adsorption energies, periodic DFT calculations approach is employed, described in chapter 3.

5.3.1 Adsorption energies on highly oriented pyrolytic graphite

The top layer of graphite on which the adsorption takes place can be identified as graphene, i.e. an infinite planar sheet formed of hexagonal carbon rings that can be seen also as a polycyclic aromatic hydrocarbon (PAH) of infinite dimensions.

The geometry of the model system was optimized starting from the minimal orthorhombic unit cell of graphite composed of 4 carbon atoms with the experimental [41] carbon-carbon distance $\mathbf{a}=1.42\text{\AA}$ and an interlayer distance of 10\AA . The optimized basal surface of the unit cell $(4.275 \times 2.46)\text{\AA}^2$, practically identical to the initial system $(4.26 \times 2.46)\text{\AA}^2$, gives an illustration of the quality of the method used for structure determinations.

A multiplied $(2 \times 3 \times 1)$ orthorhombic cell $(8.55 \times 7.38 \times 10)\text{\AA}^3$ was constructed from the optimized geometry, large enough to accommodate the adsorbate molecule and avoid biased lateral interactions. The graphite model was built from the graphene structure by adding a second carbon layer, shifted to intercarbon distance \mathbf{a} , so that carbon atoms of the added layer found themselves below the center of an hexagon of the neighboring layer. The optimized interlayer distance $\mathbf{c}=3.2\text{\AA}$ is found. The vertical dimension of the cell was increased to 25\AA to accommodate the second carbon layer and the necessary vacuum between successive slab images.

In the case of atomic adsorption on graphite, three plausible sites may be considered according to the surface topology, namely, on top of

- a carbon atom
- the center of a benzene ring
- the middle of a CC bond

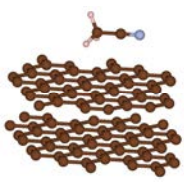
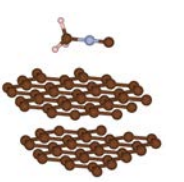
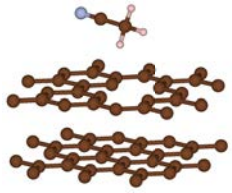
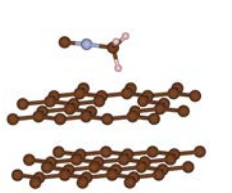
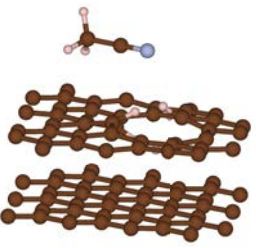
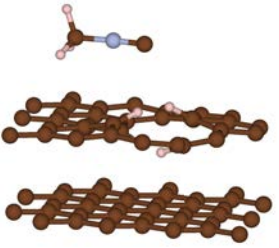
What looks simple for atoms becomes more complicated for complex molecules like CH_3CN and CH_3NC . Three different orientations can be distinguished for each adsorption site according to the orientations of the heavy atoms linear backbone and the position of the CH_3 groups whose rotation yields additional degrees of freedom. All these possibilities were systemically investigated. In particular it was verified that the CCN/CNC backbone stays linear in all situations (no deviation greater than 1 degree could be detected).

For a vertical disposition of CH_3CN and CH_3NC with the methyl umbrella away from the surface, the adsorption energy is 120 and 100 meV in average for CH_3CN and CH_3NC , respectively. The strongest adsorption occurs in both cases when the CCN/CNC backbones are on above the graphite carbon atom. However, when the verticality constrained is relaxed, the structure is no longer stable.

In the reverse position, with the methyl umbrella pointing to the surface, the adsorption energy is 160 meV in average for both CH_3CN and CH_3NC . Apart from the position above the middle of a CC bond that is less favorable for CH_3NC . No

difference can be seen neither between CH_3CN and CH_3NC nor between the various adsorption sites. The adsorption energy is stronger when the CH_3 hydrogens are close to the surface due to the polarization of the CH bonds by the CN and NC groups. This vertical orientation is energetically metastable, but in physical systems in presence of defects, diffusion and thermal interactions with adjacent molecules these vertical arrangements will switch to orientations parallel to the surface.

Table 5.3 – Views of the most stable geometries of the adsorbed CH_3CN and CH_3NC isomers on graphite. Adsorption energies E_a are given in meV and kcal/mol

CH_3CN	CH_3NC
graphite	
	
$E_a = 300 \text{ meV}$ 6.99 kcal/mol	$E_a = 290 \text{ meV}$ 6.57 kcal/mol
graphite defect: 2 carbon hole	
	
$E_a = 330 \text{ meV}$ 7.56 kcal/mol	$E_a = 320 \text{ meV}$ 7.26 kcal/mol
graphite defect: 4H-hydrogenated 2 carbon hole	
	
$E_a = 410 \text{ meV}$ 9.5 kcal/mol	$E_a = 380 \text{ meV}$ 8.6 kcal/mol

To probe different orientations parallel to the graphite surface, a manifold of ~ 24 different geometries were probed (not counting rotations of the CH_3 group). For both CH_3CN and CH_3NC isomers, all adsorption energies are grouped within a range of ~ 50 meV giving the average values of 290 and 270 meV for CH_3CN and CH_3NC , respectively.

In both isomers we found a slight preference for geometries in which the CH_3 hydrogens are closer to the CC nuclear frame (Table 5.3 - top).

The preceding study focused on the graphite ideal surface, only. Though the difference between the adsorption energies of the nitrile and isonitrile isomers is small, the same trend prevails for both isomers, namely, $E_{ads}(\text{CH}_3\text{CN}) > E_{ads}(\text{CH}_3\text{NC})$.

However, it is well understood that there is no perfect surface in space neither in the laboratory and that the range of possible defects is too wide to be modeled exhaustively.

Nonetheless, to further approach the model surface to the experimental one, a defect in the topmost layer was *a priori* introduced, with the removal of two adjacent carbon atoms, leaving a hole the size of pyrene (Table 5.3 - middle). The CH_3CN and CH_3NC isomers are no longer strictly parallel to the surface, the methyl groups being slightly tilted towards the hole to favor the interaction of the CH bonds with the electrons released on the edge of the hole. The adsorption energies are then increased by $\sim 10\%$.

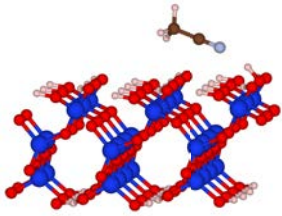
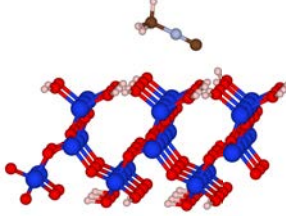
Another type of possible defect was also considered by adding supplementary hydrogen atoms to the 4 carbons on the edge of the hole (Table 5.3 - bottom) making the top layer locally resembling an hydrogenated amorphous carbon [42–44]. In this case, it is the CN/NC bonds that are over the edges of the hole, interacting with the added hydrogens. The adsorption energies are then increased by $\sim 40\%$ with respect to the pristine surface. In all cases, CH_3CN is more tightly bound to the surface than CH_3NC .

5.3.2 Adsorption energies on silica

Silicates in different forms and silica itself, whose presence in the ISM has been a long time disputed, are now clearly identified in protostellar envelopes [45] and protoplanetary disks [46, 47] using mid- and far-infrared spectra obtained by the Spitzer Space Telescope. It is now well admitted that surfaces of that type may serve as catalysts for a number of chemical syntheses such as methanol and water [48, 49]. In this work, we used quartz- α (0001) in both TPD experiments and theoretical modeling; it is the most stable crystal allotrope of silica and the most stable surface [50]. The active surface was hydroxylated by dissociative adsorption of water molecules (one per surface oxygen atom), which means that there are no free oxygen atoms left on the surface. It is consistent with the calculations by Goumans et al. [48], which showed that, once hydroxylated, the α -quartz (0001) surface was more stable than the raw surface obtained by the simple cut of a single crystal.

The α -quartz (0001) surface model was constructed from a 3 layers slab, using the experimental lattice parameters [50] and then re-optimized in the hydroxylated form. In the exploitation phase, a double minimal orthorhombic cell ($2a \times \sqrt{3}a \times 3c$, i.e. $(9.81 \times 8.49 \times 15.3)\text{\AA}^3$) was used to probe the adsorption sites. The two bottom layers

Table 5.4 – Views of the most stable geometries of the adsorbed CH₃CN and CH₃NC isomers on α -quartz (0001). Adsorption energies E_a are given in meV and kcal/mol

CH ₃ CN	CH ₃ NC
	
$E_a = 0.5$ eV 11.7 kcal/mol	$E_a = 0.5$ eV 11.7 kcal/mol

of Si and surrounding oxygen atoms were constrained to maintain the slab geometry.

The most stable adsorption sites geometries were recalculated in a bigger cell (14.59x16.85x21.18Å, vacuum 15.7Å) to verify the energy convergence. The difference observed between huge and small cell calculations was about 20 meV, that is 5% of the total adsorption energy value, suggesting the importance of the interadsorbate interaction and requiring to use model cells large enough to accommodate the adsorbate molecule and avoid biased lateral interactions.

Similar to graphite case, the CH₃CN and CH₃NC isomers have close adsorption energies on silica. Both molecules are tilted over the hydroxylated surface with two of the CH bonds pointing towards the oxygen lone pairs of the surface. The N and C extremities of the CN, respectively NC, bonds interact with the dangling OH bonds of the surface, strongly enough to induce changes in the geometries of the hydroxyl surface arrangement (Table 5.4).


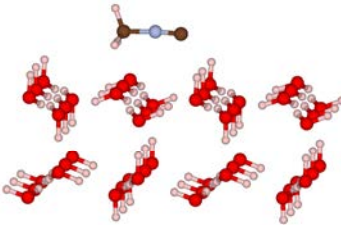
No significant difference is seen between the two isomers on the quartz surface for the strongest adsorption sites.

5.3.3 Adsorption energies on crystalline water ice

Water ices constitute a major part of the condensed matter in cold and dense regions of the ISM [51, 52]. Most of it is commonly believed to be in amorphous phase, although crystalline ice has also been detected in warmer regions such as the Kuiper belt [53–55]. On the computational side, the structure of ice has been the center of a number of studies [56–59]. Among the different structures possible, we focused on the apolar variety of crystalline ice because only apolar structures can generate slabs that are stable [60], reproduce the bulk properties, and have a balanced distribution of alternate hydrogen and oxygen sites at their surfaces (for a complete discussion, see Casassa et al.[59]).

The unit cell used to construct the slab is that of hexagonal ice *Ih* containing two bilayers, as described in chapter 4.3.1 b. After optimization, the cell volume became (4.33 × 7.49 × 7.07)Å³ and a vacuum of 15Å was introduced between neighboring slabs.

Table 5.5 – Views of the most stable geometries of the adsorbed CH_3CN and CH_3NC isomers on apolar water ice. Adsorption energies E_a are given in meV and kcal/mol

CH_3CN	CH_3NC
	
$E_a = 0.620 \text{ eV}$ 14.32 kcal/mol	$E_a = 0.570 \text{ eV}$ 13.14 kcal/mol

In the exploitation phase, the basal dimensions were doubled to avoid any lateral interactions.

It can be seen in Table 5.5 that the CH_3CN and CH_3NC isomers adsorb on the surface by two types of hydrogen bonds: one between an oxygen atom from the ice surface and the H atoms of the methyl group of the adsorbed isomer; the other between an H atom of an OH bond from the surface and the N or C atom at the other extremity of the adsorbate molecule. Both adsorption energies are practically identical, but once more the same trend is observed with $E_{ads}(\text{CH}_3\text{CN}) > E_{ads}(\text{CH}_3\text{NC})$.

5.4 Discussion and final remarks

The adsorption energies of the two isomers CH_3NC and CH_3CN on different astrophysically-relevant surfaces have been studied, both experimentally, using the TPD technique in a state-of-the-art ultrahigh vacuum system, and theoretically, by means of first principle periodic DFT calculations. This unique approach allows for determining values of adsorption energies, obtained by two independent methods, whose reliability is supported by intercomparisons between experiments and numerical simulations.

In this work, the adsorption of the two nitrile and isonitrile isomers has been studied on graphite and silica surface – as models for bare interstellar dust grain surfaces – and on water ice surface – water being the most abundant constituent of the icy mantles recovering the dust grains.

Experimentally, average adsorption energies of CH_3CN and CH_3NC onto graphite are found relatively similar, and varying in the 430 - 460 meV range, depending on the initial adsorbate coverage. Calculations performed on perfect graphene planes result in much lower adsorption energy values, of 270 and 290 meV for CH_3NC and CH_3CN , respectively. This discrepancy may be explained by important role played by structural defects on the graphite surface. As shown by the numerical simulations, adsorption energies are very sensitive to imperfections of the graphite surface. Very simple model defects, such as 2-atoms holes, hydrogenated or not, lead to a strong increase in the adsorption energies of both isomers by more than 100 meV, resulting in energies close

to what is observed experimentally. Because of the low Van der Waals interactions between the adsorbates and the graphene planes, such increase is not negligible compared to the adsorption energy found on the perfect graphite surface. Therefore, the role played by defects as stabilizer of the adsorbates has to be considered to better understand the experimental values. Earlier studies of methanol adsorption on the graphite surface used in the experiment (chapters 3.3.5 and 2.3.3 c) also suggested at that time the presence of an important amount of defects on our substrate. Thus we expect these defects to be responsible for the observed high experimental adsorption energies of CH_3CN and CH_3NC on graphite as compared to what is calculated on perfect graphene and graphite planes.

Table 5.6 – Computed adsorption energies (meV) of CH_3CN and CH_3NC in the most stable configurations in presence of graphite, 4H hydrogenated graphite, α -quartz (0001) and 2 BL- H_2O

Surface	CH_3CN E_a , eV	CH_3NC E_a , eV
graphite	0.30	0.29
2CC-hole graphite	0.33	0.32
4H-graphite	0.41	0.38
α -quartz (0001)	0.50	0.50
apolar ice <i>Ih</i>	0.62	0.57

Experiments and theoretical calculations for adsorptions on quartz and crystalline water surfaces gave very similar results for both CH_3CN and CH_3NC . On these substrates, adsorption is mainly driven by hydrogen bonding between the adsorbates and the surface O–H bonds. This kind of interaction is quite strong compared to the Van der Waals-type interaction on graphene planes, and therefore the role played by defects on adsorption energies is expected to be comparatively less important.

On the silica surface, the theoretical result shows no difference (0.50 eV both for strongest sites of CH_3NC and CH_3CN) in the limit of a single molecule adsorption on the surface. Since the calculations were performed for the most bounded sites, the theoretical values should match the highest values of the experimental energy distribution in the limit of the low surface coverage (460 and 495 meV respectively). This is the case here when considering the E_a distribution width of about 70meV. Some difference may originate from the differences in aggregation behavior of CH_3NC and CH_3CN , though. Further investigation on the effect of adsorbate aggregation, different quartz substrate models, as well as the topological analysis to investigate charge distribution and bonds should be performed to clarify the case.

In the case of crystalline water ice surface, the values are also found to be very close between the experimental and theoretical approaches. Nevertheless, the fact that the underlying water ice desorbs simultaneously with CH_3NC or CH_3CN makes that the experimental values obtained represent a lower limit for the adsorption energy of $\text{CH}_3\text{CN}/\text{CH}_3\text{NC}$ on crystalline water. Only numerical simulations allow in this case for unambiguous determination of the adsorption energies of the nitrile/isonitrile isomers

on the water ice. Interestingly, the calculated energies — 570 and 620 meV for CH_3NC and CH_3CN respectively — are found higher than the water adsorption energy on crystalline water ice (497eV, [40]). This is what was expected from the experimental results: the difference that was experimentally observed between CH_3NC and CH_3CN cannot be explained by the desorption of the underlying crystalline ice only, but instead by a contribution of the interactions between the isomers and the ice surface. If those interactions had been much stronger than the adsorption of water on water ice, then all the desorption would have been only due to the water sublimation, and no difference between isomers would have been detected.

The adsorption energies of CH_3CN are found equal or slightly higher than the one of CH_3NC by 20 to 40 meV, both experimentally and theoretically. The reason for that is not to be searched for in different values of the dipole moments since both are close to ~ 4 Debye (4.0 and 3.9 for CH_3CN and CH_3NC respectively), but in a slightly stronger ability of CH_3CN to perform H-bonds because of a local excess of positive charge on the hydrogens of the methyl group.

This comparable behavior of the two isomers might be a reason, also, why their abundance ratio is relatively constant in many different ISM regions, from the colder ones where the interaction of the species with the icy mantle — mainly composed of water — is more likely, to warmer regions where the adsorption/re-adsorption on the naked carbonaceous or silicated grain surface may begin to play an important role. Since the difference in adsorption energies do not depend on the substrates, the differential desorption effect between isomers on the gas phase $\text{CH}_3\text{CN}/\text{CH}_3\text{NC}$ abundance ratio should be the same whatever is the considered region (carbon rich or silicate rich) of the ISM.

References

- [1] Holger S.P. Müller et al. *Molecules in Space*. www.astro.uni-koeln.de/cdms/molecules, 2015.
- [2] A. McKellar. “Evidence for the Molecular Origin of Some Hitherto Unidentified Interstellar Lines”. In: *Publications of the Astronomical Society of the Pacific* 52 (1940), p. 187.
- [3] Walter S. Adams. “Some Results with the COUDÉ Spectrograph of the Mount Wilson Observatory.” en. In: *The Astrophysical Journal* 93 (Jan. 1941), p. 11.
- [4] K. B. Jefferts, A. A. Penzias, and R. W. Wilson. “Observation of the CN Radical in the Orion Nebula and W51”. en. In: *The Astrophysical Journal* 161 (Aug. 1970), p. L87.
- [5] Lewis E. Snyder and David Buhl. “Interstellar Isocyanic Acid”. en. In: *The Astrophysical Journal* 177 (Nov. 1972), p. 619.
- [6] P. M. Solomon et al. “Detection of Millimeter Emission Lines from Interstellar Methyl Cyanide”. en. In: *The Astrophysical Journal* 168 (Sept. 1971), p. L107.
- [7] B. E. Turner. “Detection of Interstellar Cyanoacetylene”. en. In: *The Astrophysical Journal* 163 (Jan. 1971), p. L35.
- [8] B. Zuckerman et al. “Observations of cs, HCN, U89.2, and U90.7 in NGC 2264”. en. In: *The Astrophysical Journal* 173 (May 1972), p. L125.
- [9] J. Cernicharo et al. “Tentative detection of CH₃NC towards SGR B2”. In: *Astronomy and Astrophysics* 189 (1988), p. L1.
- [10] P. Gratier et al. “The IRAM-30 m line survey of the Horsehead PDR: III. High abundance of complex (iso-)nitrile molecules in UV-illuminated gas”. In: *Astronomy & Astrophysics* 557 (Sept. 2013), A101.
- [11] W. M. Irvine and F. P. Schloerb. “Cyanide and isocyanide abundances in the cold, dark cloud TMC-1”. en. In: *The Astrophysical Journal* 282 (July 1984), p. 516.
- [12] P. Schilke et al. “A study of HCN, HNC and their isotopomers in OMC-1. I - Abundances and chemistry”. In: *Astronomy and Astrophysics* 256 (1992), pp. 595–612.
- [13] P. P. Tennekes et al. “HCN and HNC mapping of the protostellar core Chamaeleon-MMS1”. In: *Astronomy & Astrophysics* 456.3 (2006), p. 7.
- [14] A. Fuente et al. “Observational study of reactive ions and radicals in PDRs”. In: *Astronomy & Astrophysics* 406.3 (2003), p. 15.
- [15] Anthony J. Remijan et al. “Interstellar Isomers: The Importance of Bonding Energy Differences”. en. In: *The Astrophysical Journal* 632.1 (Oct. 2005), p. 333.
- [16] M. Lattalais et al. “Interstellar Complex Organic Molecules and the Minimum Energy Principle”. en. In: *The Astrophysical Journal Letters* 696.2 (May 2009), p. L133.

- [17] M. Lattalais et al. “A new weapon for the interstellar complex organic molecule hunt: the minimum energy principle”. In: *Astronomy and Astrophysics* 519 (Sept. 2010), A30.
- [18] M. Lattalais et al. “About the detectability of glycine in the interstellar medium”. In: *Astronomy & Astrophysics* 532 (Aug. 2011), A39.
- [19] Edgar Mendoza et al. “Molecules with a peptide link in protostellar shocks: a comprehensive study of L1157”. en. In: *Monthly Notices of the Royal Astronomical Society* 445.1 (Nov. 2014), pp. 151–161.
- [20] A. López-Sepulcre et al. “Shedding light on the formation of the pre-biotic molecule formamide with ASAI”. en. In: *Monthly Notices of the Royal Astronomical Society* 449.3 (May 2015), pp. 2438–2458.
- [21] J. Mayo Greenberg. “Radical formation, chemical processing, and explosion of interstellar grains”. en. In: *Astrophysics and Space Science* 39.1 (Jan. 1976), pp. 9–18.
- [22] Daniel S. Greenberg. “Dog Food, People Food and Other Matters”. In: *New England Journal of Medicine* 295.26 (1976), pp. 1487–1488.
- [23] A. Leger and J. L. Puget. “Identification of the ‘unidentified’ IR emission features of interstellar dust?”. In: *Astronomy and Astrophysics* 137 (1984), pp. L5–L8.
- [24] L. J. Allamandola, A. G. G. M. Tielens, and J. R. Barker. “Polycyclic aromatic hydrocarbons and the unidentified infrared emission bands - Auto exhaust along the Milky Way”. en. In: *The Astrophysical Journal* 290 (Mar. 1985), p. L25.
- [25] F. J. Molster et al. “Low-temperature crystallization of silicate dust in circumstellar disks”. en. In: *Nature* 401.6753 (1999), pp. 563–565.
- [26] W. A. Schutte et al. “Weak ice absorption features at 7.24 and 7.41 μm in the spectrum of the obscured young stellar object W 33A”. In: *Astronomy and Astrophysics* 343 (1999), pp. 966–976.
- [27] E. L. Gibb et al. “Interstellar Ice: The Infrared Space Observatory Legacy”. en. In: *The Astrophysical Journal Supplement Series* 151.1 (Mar. 2004), p. 35.
- [28] Naoki Watanabe and Akira Kouchi. “Ice surface reactions: A key to chemical evolution in space”. In: *Progress in Surface Science* 83.10–12 (2008), pp. 439–489.
- [29] A.C. Adwin Boogert, Perry A. Gerakines, and Douglas C.B. Whittet. “Observations of the Icy Universe”. In: *Annual Review of Astronomy and Astrophysics* 53.1 (2015), null.
- [30] P. J. Linstrom and W. G. Mallard, eds. *NIST Chemistry WebBook, NIST Standard Reference Database Number 69*. Gaithersburg MD, 20899: National Institute of Standards and Technology, June 2005.
- [31] F. W. Parker, A. H. Nielsen, and W. H. Fletcher. “The infrared absorption spectrum of methyl cyanide vapor”. In: *Journal of Molecular Spectroscopy* 1.1–4 (1957), pp. 107–123.

- [32] Jason E. Schaff and Jeffrey T. Roberts. “Interaction of Acetonitrile with the Surfaces of Amorphous and Crystalline Ice”. In: *Langmuir* 15.21 (1999), pp. 7232–7237.
- [33] K. Murphy et al. “Adsorption, decomposition and isomerization of methyl isocyanide and acetonitrile on Pd(111)”. In: *Surface Science* 467.1–3 (2000), pp. 1–9.
- [34] Robin J. Speedy et al. “The evaporation rate, free energy, and entropy of amorphous water at 150 K”. In: *The Journal of Chemical Physics* 105.1 (July 1996), pp. 240–244.
- [35] M. Bertin et al. “Adsorption of Organic Isomers on Water Ice Surfaces: A Study of Acetic Acid and Methyl Formate”. In: *The Journal of Physical Chemistry C* 115.26 (2011), pp. 12920–12928.
- [36] P. Modica and M. E. Palumbo. “Formation of methyl formate after cosmic ion irradiation of icy grain mantles”. In: *Astronomy and Astrophysics* 519 (Sept. 2010), A22.
- [37] R. Alan May, R. Scott Smith, and Bruce D. Kay. “Probing the interaction of amorphous solid water on a hydrophobic surface: dewetting and crystallization kinetics of ASW on carbon tetrachloride”. en. In: *Physical Chemistry Chemical Physics* 13.44 (Nov. 2011), pp. 19848–19855.
- [38] Patrick Ayotte et al. “Effect of porosity on the adsorption, desorption, trapping, and release of volatile gases by amorphous solid water”. en. In: *Journal of Geophysical Research: Planets* 106.E12 (2001), pp. 33387–33392.
- [39] R. Scott Smith et al. “The Molecular Volcano: Abrupt $\text{CC}_{10}\text{H}_{16}$ Desorption Driven by the Crystallization of Amorphous Solid Water”. In: *Physical Review Letters* 79.5 (1997), pp. 909–912.
- [40] Helen J. Fraser et al. “Thermal desorption of water ice in the interstellar medium”. en. In: *Monthly Notices of the Royal Astronomical Society* 327.4 (Nov. 2001), pp. 1165–1172.
- [41] B. E. Warren. “X-Ray Diffraction Study of Carbon Black”. In: *The Journal of Chemical Physics* 2.9 (Sept. 1934), pp. 551–555.
- [42] R. Papoular et al. “On the nature of interstellar carbonaceous dust”. In: *Planetary and Space Science. Dust, Molecules and Backgrounds: from Laboratory to Space* 43.10–11 (1995), pp. 1287–1291.
- [43] L. Colangeli et al. “Extinction signatures of amorphous carbon grains from the vacuum UV to the far-IR”. In: *Planetary and Space Science. Dust, Molecules and Backgrounds: from Laboratory to Space* 43.10–11 (1995), pp. 1263–1269.
- [44] F. Pauzat and Y. Ellinger. “The 3.2–3.5 μm region revisited – II. A theoretical study of the effects of hydrogenation on some model PAHs”. en. In: *Monthly Notices of the Royal Astronomical Society* 324.2 (2001), pp. 355–366.
- [45] Charles A. Poteet et al. “A Spitzer Infrared Spectrograph Detection of Crystalline Silicates in a Protostellar Envelope”. en. In: *The Astrophysical Journal Letters* 733.2 (June 2011), p. L32.

- [46] A. Juhász et al. “Dust Evolution in Protoplanetary Disks Around Herbig Ae/Be Stars—the Spitzer View”. en. In: *The Astrophysical Journal* 721.1 (Sept. 2010), p. 431.
- [47] B. A. Sargent et al. “Silica in Protoplanetary Disks”. en. In: *The Astrophysical Journal* 690.2 (Jan. 2009), p. 1193.
- [48] T. P. M. Goumans et al. “Structure and stability of the (001) alpha-quartz surface”. eng. In: *Physical chemistry chemical physics: PCCP* 9.17 (May 2007), pp. 2146–2152.
- [49] Jiao He and Gianfranco Vidali. “Experiments of Water Formation on Warm Silicates”. en. In: *The Astrophysical Journal* 788.1 (June 2014), p. 50.
- [50] L. Levien, Ct Prewitt, and Dj Weidner. “Structure and Elastic Properties of Quartz at Pressure”. English. In: *American Mineralogist* 65.9-10 (1980). WOS:A1980KR07600008, pp. 920–930.
- [51] Karin I. Öberg et al. “The Spitzer Ice Legacy: Ice Evolution from Cores to Protostars”. en. In: *The Astrophysical Journal* 740.2 (Oct. 2011), p. 109.
- [52] A. C. A. Boogert et al. “Ice and Dust in the Quiescent Medium of Isolated Dense Cores”. en. In: *The Astrophysical Journal* 729.2 (Mar. 2011), p. 92.
- [53] P. Jenniskens et al. “High-Density Amorphous Ice, the Frost on Interstellar Grains”. en. In: *The Astrophysical Journal* 455 (Jan. 1995), p. 389.
- [54] David C. Jewitt and Jane Luu. “Crystalline water ice on the Kuiper belt object (50000) Quaoar”. en. In: *Nature* 432.7018 (2004), pp. 731–733.
- [55] Sergio Molinari et al. “Detection of the 62 Micron Crystalline H₂O Ice Feature in Emission toward HH 7 with the Infrared Space Observatory Long-Wavelength Spectrometer”. en. In: *The Astrophysical Journal Letters* 521.1 (Aug. 1999), p. L71.
- [56] Silvia Casassa and Cesare Pisani. “Interaction of HOCl with a chlorinated ice surface to produce molecular chlorine: An ab-initio study”. In: *The Journal of Chemical Physics* 116.22 (June 2002), pp. 9856–9864.
- [57] Jer-Lai Kuo and Sherwin J. Singer. “Graph invariants for periodic systems: Towards predicting physical properties from the hydrogen bond topology of ice”. In: *Physical Review E* 67.1 (2003), p. 016114.
- [58] Tomas K. Hirsch and Lars Ojamäe. “Quantum-Chemical and Force-Field Investigations of Ice Ih: Computation of Proton-Ordered Structures and Prediction of Their Lattice Energies”. In: *The Journal of Physical Chemistry B* 108.40 (2004), pp. 15856–15864.
- [59] S. Casassa et al. “Proton ordered cubic and hexagonal periodic models of ordinary ice”. In: *Chemical Physics Letters* 409.1–3 (2005), pp. 110–117.
- [60] Giovanni Bussolin et al. “Ab initio study of HCl and HF interaction with crystalline ice. I. Physical adsorption”. In: *The Journal of Chemical Physics* 108.22 (June 1998), pp. 9516–9528.

Chapter 6

Ionization and trapping of sodium in cometary ices

Contrary to the other subjects presented in this thesis, this one is an all-theoretical study. No experimental measurement has been performed for the adsorption energies and the other observables necessary to interpret the process exposed here.

6.1 Study context

Conditions in the proto-solar nebula have left their mark in the composition of cometary volatiles, thought to be some of the most pristine material in the solar system. Cometary compositions represent the end point of processing that began in the parent molecular cloud core and continued through the collapse of that core to form the proto-sun and the solar nebula, and finally during the evolution of the solar nebula itself as the cometary bodies were accreting. Disentangling the effects of the various epochs on the final composition of a comet is complicated.

Rosetta's observations are eagerly awaited to provide new insights into the chemical processes that resulted in the formation of cometary volatiles and consequently into the conditions that were present in the solar nebula at their time of formation. Any study likely to prepare for the interpretation of the huge collection of data to come is welcome. It is within this context that we propose an entirely theoretical study of a most peculiar component observed in the tail of some comets as Hale Bopp: neutral atomic sodium.

The presence of sodium D line emission has been confirmed in a large number of comets since it was first reported more than a century ago [1]. This neutral sodium gas tail is totally different from the previously known ion and dust tails, and its associated source is still unclear.

To solve the enigma, we propose to follow the chemical journey of sodium, starting from the ion Na^+ washed out of the refractory material of the core during the hydration phase, until the final transformation into a neutral atom when released from the sublimating crystalline cometary ice. The environmental conditions and the evolution of the atom and its charge, while progressing from the kernel to the surface into the successive layers of ice, are presented in the following paper (6.2).

To perform the calculations needed, quantum chemistry methods have been used as periodic DFT to determine the structures and energies of the systems (substrate-adsorbate) and ELF topological analysis to quantify the localization of the charge.

6.2 Paper

Y. Ellinger et al. “Neutral Na in Cometary Tails as a Remnant of Early Aqueous Alteration”. en. In: *The Astrophysical Journal Letters* 801.2 (Mar. 2015), p. L30

NEUTRAL Na IN COMETARY TAILS AS A REMNANT OF EARLY AQUEOUS ALTERATION

Y. ELLINGER¹, F. PAUZAT¹, O. MOUSIS², A. GUILBERT-LEPOUTRE³, F. LEBLANC⁴, M. ALI-DIB³, M. DORONIN^{1,5}, E. ZICLER¹, AND
A. DORESSOINDIRAM⁶

¹Laboratoire de Chimie Théorique, Sorbonne Universités, UPMC Univ. Paris 06, CNRS UMR 7616, F-75252 Paris CEDEX 05, France

²Laboratoire d'Astrophysique de Marseille (LAM), Aix Marseille Université, CNRS, UMR 7326, F-13388 Marseille, France

³Observatoire des Sciences de l'Univers de Besançon, Université de Franche-Comté, Institut UTINAM, CNRS/INSU, UMR 6213, F-35030 Besançon CEDEX, France

⁴LATMOS/IPSL, Sorbonne Universités, UPMC Univ. Paris 06, CNRS UMR 8190, F-75252 Paris CEDEX 05, France

⁵Laboratoire de Physique Moléculaire pour l'Atmosphère et l'Astrophysique (LERMA/LPMAA), Sorbonne Universités, UPMC Univ. Paris 06, CNRS UMR 7092, F-75252 Paris CEDEX 05, France

⁶LESIA—Observatoire de Paris, Sorbonne Universités, UPMC Univ. Paris 06, Univ. Paris-Diderot, CNRS UMR 8109, F-92190 Meudon, France
Received 2014 November 6; accepted 2015 February 6; published 2015 March 12

ABSTRACT

Observations of comet C/1995O1 Hale-Bopp during the spring of 1997 led to the discovery of a neutral sodium tail whose origin is still not clearly understood. Here, we propose an interpretation for the origin of this sodium tail, which is based upon chemical grounds. Starting from Na⁺ trapped chemically during the condensation of refractory material in the protosolar nebula to its incorporation in the building blocks of comets and its transfer from refractory to volatile phases in the nucleus due to aqueous alteration, we follow the chemical path of sodium until its transformation into a neutral atom when released from the sublimating cometary ice. We propose that two Na reservoirs should coexist in a comet: one coming from the refractory dust, the other one from the icy matrix. Their relative importance would depend on the extent of the zone where liquid water formed within the nucleus and the time during which water remained liquid, thus favoring the Na⁺ exchange between rocks and ice. These two key parameters would in turn strongly depend on the thermal history of the comet (amounts of radiogenic nuclides, orbital history, etc.). If our model is correct, the detection of Na originating from water ice would be a testimonial of the past aqueous alteration of the comet or its parent body.

Key words: astrochemistry – comets: general – Kuiper Belt: general – Oort Cloud – protoplanetary disks

1. INTRODUCTION

The presence of sodium D-line emission has been confirmed in a large number of comets close to perihelion for over more than a century (Bredichin 1882; Lemon & Bobrovnikoff 1926; Levin 1964; Oppenheimer 1980; Leblanc et al. 2008; Cochran et al. 2013). Observations of comet C/1995O1 Hale-Bopp during the spring of 1997 led to the discovery of a new tail connected with the sodium D-line emission. This neutral sodium gas tail is entirely different from the previously known ion and dust tails, and its associated source is unclear. It has been proposed that the third type of tail is shaped by radiation pressure due to resonant scattering of sodium atoms (Cremoneese et al. 1997). How the observed Na atoms are released from the nucleus and/or from the dust is debated. The evolution of the Na release rate with respect to heliocentric distance suggests a release dominated by thermal desorption (Watanabe et al. 2003; Furusho et al. 2005) rather than by energetic processes like photo-desorption, solar wind sputtering, or cometary ion sputtering (Leblanc et al. 2008).

Here, a completely different scenario built upon chemical grounds is proposed for discussion. Starting from Na⁺ trapped chemically during the condensation of refractory material in the protosolar nebula to its incorporation in the building blocks of comets and its post-formation evolution in the cometary matrix, we follow the chemical path of sodium until its transformation into a neutral atom when released from the sublimating cometary ice. In this Letter, we address these critical points in chronological order in the subsequent sections. We first report the results of thermochemical equilibrium calculations that show that Na is mainly trapped in rocks in the protosolar nebula. Due to radiogenic heating, the parent bodies of comets,

initially made from a mixture of rocks and ices, have undergone some melting in their interiors, implying that liquid water interacted with rocks. This washing led to a transfer of Na from the rocks to the aqueous phase in the form of Na⁺ ions. Once liquid water froze, Na was trapped in stable cages made from water molecules, as demonstrated by quantum calculations. In the end, Na was released as a neutral atom when the ice vaporized due to heating. In other words, having Na in cometary tails could be a testimonial of the past presence of liquid water during the thermal history of comets or the thermal history of their parent bodies.

2. FORMATION OF Na-RICH REFRACTORY MATERIAL IN THE NEBULA

The solid/gaseous composition of the disk is obtained using the HSC Chemistry software developed by Outotec Research,⁷ which is based on the Gibbs energy minimization technique (White et al. 1958). This method takes as an input the initial composition of the system and then calculates the resulting most stable species (having the minimal Gibbs energy) on a pressure–temperature grid. This method necessitates a database of a large number of species for accuracy, hence our commercial package choice since the present version contains more than 28,000 chemical compounds. As an input in our calculations, we have used a gaseous mixture of a protosolar composition (Asplund et al. 2009) with Na/H₂ = 3.81 × 10⁻⁶ in the initial gas phase. The software was run to get the abundances of the most abundant Na-bearing species in the protosolar nebula at $P = 10^{-4}$ bar, a typical disk's pressure, and

⁷ <http://outotec.com/en/Products-services/HSC-Chemistry>

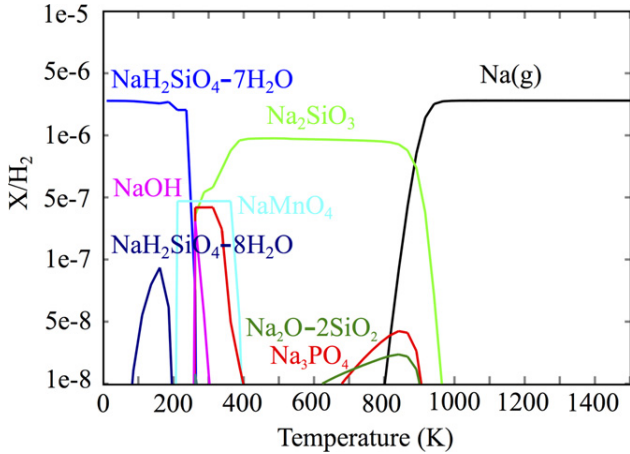


Figure 1. Equilibrium abundances relatives to H_2 of Na-bearing compounds forming over a wide range of temperatures at a constant total gas pressure of 10^{-4} bar in the protosolar nebula. Sodium is in gaseous form at temperatures higher than ~ 900 K. At lower temperatures, Na is incorporated in the solid refractory phase.

temperatures in the 10–1500 K range, which are valid for a wide range of heliocentric distances (from ~ 1 to 30 AU). Figure 1 shows that Na is in gaseous form at temperatures higher than ~ 900 K. Interestingly, it is unclear whether or not Na was ionized or neutral at high temperatures in the protosolar nebula. Indeed, if the ionization of the disk’s H_2 from EUV and X-rays was efficient (Glassgold et al. 2000), then the probability of Na^+ meeting an electron would be high. At lower temperatures, Na becomes essentially incorporated in the solid refractory phase. Our calculations then support the idea that the sodium observed in comets was originally acquired by their refractory material at its condensation epoch in the protosolar nebula.

3. ICE MELTING IN COMETS

Comets and their parent bodies accreted from a mixture of volatile ices and rocky material. The refractory material includes radioactive isotopes, whose decay provides an important source of heat in comet nuclei, possibly significantly altering their initial structure and composition. As of today, the effects of early processing of comet material remain mostly unknown. Comet nuclei appear very primitive in nature: for instance, they contain volatiles like CO, which require that they suffered from an extremely limited thermal processing after their formation. Given their very short lifetime, the effectiveness of nuclides such as ^{26}Al or ^{60}Fe in heating a comet interior strongly depends on the nucleus formation timescale. Recent formation theories (Johansen et al. 2007; Johansen & Klahr 2011) arguing for very short formation timescales are therefore compatible with a possible significant heating of comet material. This is supported by the detection of minerals formed by aqueous alteration in meteorites and, most strikingly, by the identification of brine inclusions in crystals like those found in the Monahans chondrite, providing a sample of the liquid presumably responsible for this aqueous alteration in planetesimals (Zolensky et al. 1999). Hints of aqueous alteration were also found in the dust samples from comet 81P/Wild 2 brought by the Stardust mission (Brownlee 2014).

Despite the large uncertainty in our knowledge of comet early thermal processing, we can investigate the possible outcome of radiogenic heating for a realistic range of initial parameters. Heating due to the radioactive decay of short-lived nuclides such as ^{26}Al or ^{60}Fe can be described by

$$Q_{\text{rad}} = \rho_d X_{\text{rad}} H_{\text{rad}} \frac{1}{\tau_{\text{rad}}} \exp\left(\frac{-t}{\tau_{\text{rad}}}\right), \quad (1)$$

with ρ_d , the dust bulk density; X_{rad} , the initial mass fraction of the nuclide in the dust; H_{rad} , the heat released by this nuclide per unit mass upon decay; τ_{rad} , its decay time; and t , the time. The decay product of short-lived radionuclide ^{26}Al , ^{26}Mg , can be found in Ca–Al rich inclusions (CAIs), which are believed to be the first solids to condensate in the solar system. A compilation of ^{26}Mg abundance measurements for various meteorites shows that the majority of chondrites have a canonical ratio $^{26}Al/^{27}Al = 5 \times 10^{-5}$ (MacPherson et al. 1995). The distribution of ^{26}Al has been inferred to be uniform, at least for the inner solar system (Jacobsen et al. 2008). However, CAIs with low ($\ll 5 \times 10^{-6}$) ratios have been reported (Kunihiro et al. 2004; Liu et al. 2009). The existence of such inclusions with no excess of ^{26}Mg is perceived as a reason to invoke a non-uniform distribution of ^{26}Al within the solar system (Makide et al. 2011, 2013), but given the current debate, we consider that ^{26}Al was uniformly distributed across the solar system as a first approximation, with a canonical value at the time of CAI formation.

In order to assess the effect of radiogenic heating on the early history of comet parent bodies, we need to solve the heat conduction equation:

$$\rho c \frac{\partial T}{\partial t} + \text{div} \left(-\kappa \overrightarrow{\text{grad}} T \right) = Q_{\text{rad}}, \quad (2)$$

where T is the temperature distribution to be determined, ρ is the nucleus bulk density, c is the material heat capacity, κ is its effective thermal conductivity, and Q_{rad} is the radiogenic heat source described in Equation (1). Figure 2 presents the evolution of the internal temperature for a comet parent body with a radius of 30 km, computed with the thermal evolution model of Guilbert-Lepoutre et al. (2011) and assuming that the icy matrix is initially made of amorphous ice and crystalline ice, for formation times ranging from 0 to 3 Myr after CAI formation. A typical mass fraction of 50% is assumed for the ice ($\sim 70\%$ in volume fraction) in the nucleus (Huebner et al. 2006). For other thermophysical parameters, we assumed typical values as found in the literature (Huebner et al. 2006), for example, a density of 700 kg m^{-3} , a porosity of $\sim 80\%$, and an initial thermal inertia lower than $10 \text{ J K}^{-1} \text{ m}^{-2} \text{ s}^{-1/2}$. Both amorphous and crystalline cases lead to similar conclusions: the results show that liquid water is produced in many situations, in particular, during the early evolution of comets. Whatever the initial state of the water-ice matrix, our calculations show that liquid water may be produced in the core of comet parent bodies in many situations, especially if comets formed quickly after CAI formation (in typically less than 0.3 Myr). Although still debatable, the potential effect of ^{26}Al decay on the thermal history of comets has been known for decades. Interestingly, any intermediate case in which the icy matrix would be composed of a mixture of crystalline and amorphous water ice would have a temperature evolution

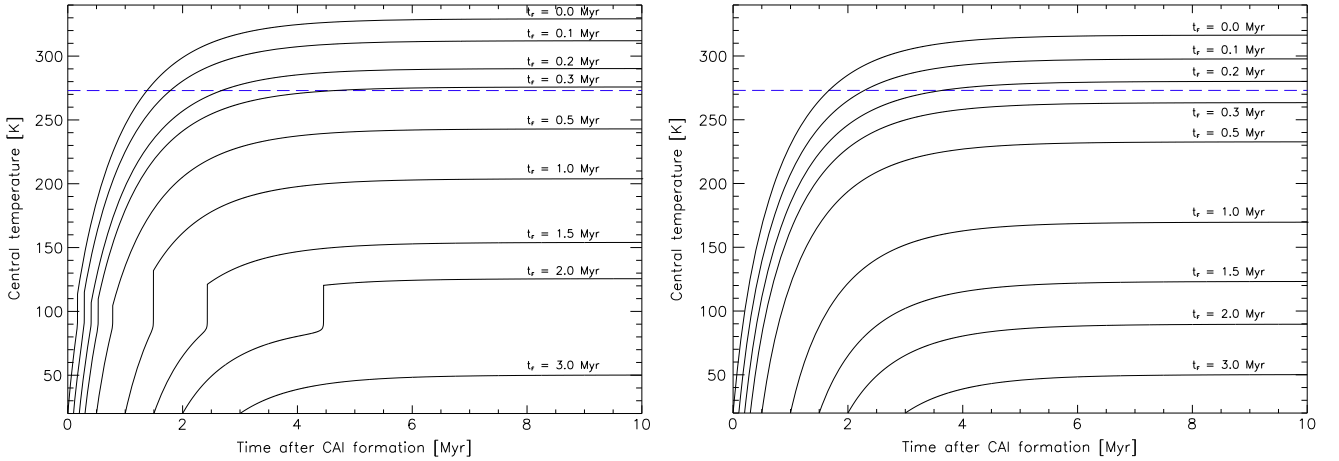


Figure 2. Evolution of the central temperature of a 30 km radius comet parent body, as a function of time after CAI formation, under the influence of heating by the decay of radioactive nuclides ^{26}Al and ^{60}Fe . The icy matrix is initially considered amorphous (left panel) or crystalline (right panel). The phase transition between amorphous and crystalline water ice considered here is exothermic (see Huebner et al. 2006 for a review). Each solid line shows the temperature evolution after a specific formation time after CAI formation, ranging from 0 (top curve) to 3 Myr (bottom curve). The dashed line highlights the melting temperature of water ice.

Table 1
Electronic Distribution within the Na–H₂O Complex

Basins	Population (e^-)
Core (O)	2.12
Core (Na)	10.02
Val (OH)	1.68
Val (OH)	1.68
Val (lpO)	2.30
Val (lpO)	2.37
Val (Na)	0.77

ranging between the two extreme cases and induce ice melting at similar conditions.

The effects of ^{26}Al decay on the thermal history of comets has been known for decades. Irvine et al. (1980) and Wallis (1980) showed that the heat produced by ^{26}Al decay could melt water ice. Prialnik et al. (1987) studied the implications of this intense heating with regard to the time formation of comets. They found that the heat released upon radioactive decay could potentially result in the melting of cores for objects larger than 6 km. Characteristics such as porosity, thermal conductivity, composition, or size can strongly influence the outcome of early radiogenic heating. For example, a smaller amount of dust in the ice/dust mixture would result in lower internal temperatures since fewer amounts of radionuclides would be available to heat the objects. This would decrease the chances for liquid water to be produced in the core of comet parent bodies. The influence of each of these unknown parameters has already been addressed in the literature. For instance, Haruyama et al. (1993) showed that thermal histories are also very sensitive to the material thermal conductivity. Indeed, Prialnik & Podolak (1995) demonstrated that depending on an object’s size, thermal conductivity, porosity, and initial composition, the early thermal evolution under the influence of ^{26}Al decay could lead to distinct outcomes, ranging from pristine structure being thoroughly preserved to extensive melting of ice in comet cores, sometimes extending all the way up to the surface. We mention that, although debatable, the occurrence of liquid water in comets or comet parent bodies would be strengthened by accounting for some accretional

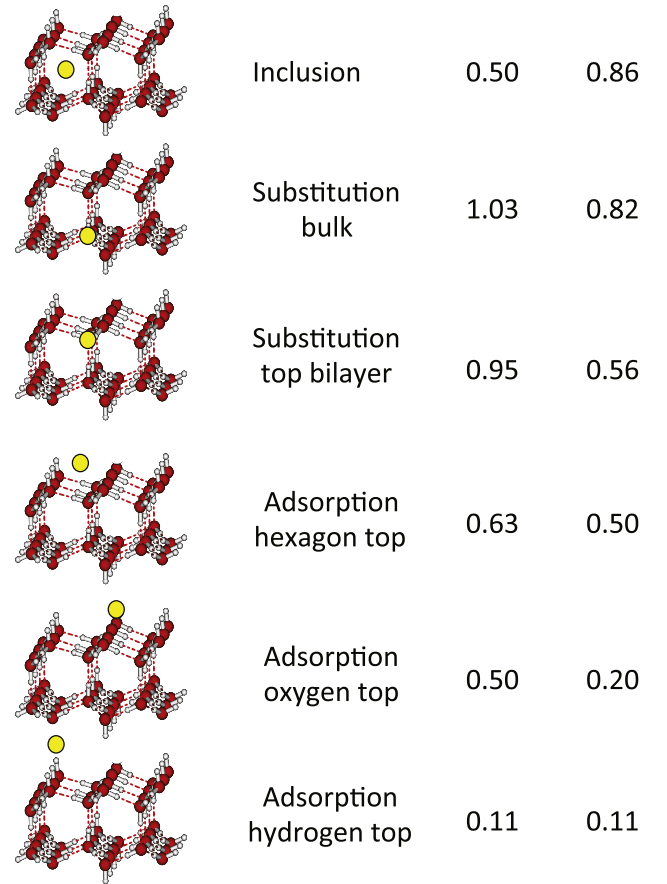


Figure 3. Typical structures of Na–H₂O_{ice} arrangements. Column 3 gives the stability in eV and column 4 reports the net charge of Na according to position. Na, O, and H atoms are colored in yellow, red, and gray, respectively.

heating, processing comet material concurrently with radiogenic heating during the lifetime of short-lived nuclides.

These two processes have been combined into a single model (Merk & Prialnik 2006), showing that the early occurrence of liquid water in 2–32 km radius bodies may be a very common phenomenon. For example, the authors find

that for a given set of realistic initial parameters, all accreting objects with a final radius above 4 km could produce liquid water cores, extending from 10% to $\sim 90\%$ of the overall interior and lasting for up to 5 Myr.

4. CHEMICAL MODEL

Neutral sodium cannot survive in liquid water and becomes ionized Na^+ with the formation of hydroxyl OH^- and release of molecular hydrogen. This statement, which could be located in any college chemistry textbook for several decades now, has only really been explained in depth in the last 15 years. Using Car–Parinello molecular dynamics (Mundy et al. 2000; Mercuri et al. 2001), as well as static density functional theory in a cluster approach (Ferro & Allouche 2003), it was shown that it is the Na_2 dimer that is at the origin of this exothermic reaction, not atomic Na.

Taking the relative abundance ratio $\text{Na}/\text{H}_2\text{O}$ of $\sim 5 \cdot 10^{-6}$ from comet Hale-Bopp (Cremonese et al. 2002), the probability of forming Na_2 in the cometary environment is extremely weak. Hence, sodium can only be present in the form of isolated atoms surrounded by layers of H_2O molecules. A sampling of the representative structures of sodium in apolar solid water ice has been obtained using a strategy based on periodic density functional theory that has proved appropriate for modeling bulk and surface ice structures (Casassa & Pisani 2002; Calatayud et al. 2003; Casassa et al. 2005).

Practically, we used the Vienna ab initio simulation package (Kresse & Hafner 1994a, 1994b). It is a code specifically designed for the study of solid state electronic structures in a periodic formalism. It makes use of a plane-wave expansion of the basis set coupled to projector augmented wave ultrasoft pseudo-potentials for the atomic cores. The integration grid was adapted to provide an equivalent treatment for all the unit cells considered with an optimized 500 eV energy cutoff. As in previous work on the adsorption of organic molecules (Lattalais et al. 2011), the generalized gradient approximation was employed in the form of the Perdew and Wang exchange-correlation functional (PW 91; Perdew et al. 1992). The contribution of long-range interactions due to the spatial extension of the sodium 3s orbital was considered by employing the Grimme correction scheme (Grimme 2004, 2006; Grimme et al. 2010). The technical details concerning the optimization schemes, the construction of the molecular slabs, and the definition of the unit cell can be found in the aforementioned specialized papers.

How the electronic charge of the sodium atom varies according to its position in the ice has been addressed by means of a topological analysis (Silvi & Savin 1994) of the electron localization function. The physical space is partitioned into well-defined volumes, each of which correspond to a clear chemical situation, as represented by the Lewis structural formula in terms of core and valence (bonds and lone pair) electrons. The chemically significant electronic populations are obtained by numerical integration of the electronic density over the corresponding volumes. In practice, the topological analysis was performed by means of the TOPMOD package (Llusar et al. 1999) and its recent extension to periodic systems (Kozłowski & Pilmé 2011).

Using the same level of functionality as for crystalline ice, we first studied the elemental brick of the Na in ice puzzle, i.e., $\text{Na}-\text{H}_2\text{O}$. We found a stable pyramidal structure of Cs symmetry in which both the unpaired electron and the $\text{Na}-\text{O}$

linkage are situated in the bisector plane of the water molecule, meaning a $^2A'$ spectroscopic ground state with a binding energy of ~ 0.3 eV. It should be pointed out that such energy is of the same order for the $\text{H}_2\text{O}-\text{H}_2\text{O}$ dimer, which lets anticipate a possible replacement of H_2O by Na in the crystal structure.

The important finding shown by the topological analysis in Table 1 is that Na retains 79% of its unpaired electron, which amount to a net charge of q_{Na} of +0.21 electron, far from a fully ionic structure. The path of Na from its inclusion in the bulk of the crystal to the surface where it desorbs is displayed top to bottom in Figure 3, together with the stability and ionicity of each typical situation.

In the top structure, Na is encapsulated in a hole inside the crystal (slightly distorted to accommodate the presence of Na). In this position, it is stabilized by ~ 0.5 eV, i.e., by a little less than the cohesion energy of the ice, with $q_{\text{Na}} = +0.86$ electron.

In the substitution structures, Na is taking the place of an H_2O molecule. It interacts strongly with its three closest neighbors. In this structure, Na is stabilized by ~ 1 eV when deep in the crystal, a little less when reaching the top bilayer. At the same time, Na loses part of its ionic character (+0.82 to +0.56 electron).

In the three bottom structures, Na is adsorbed on the surface of the ice. When on top of the center of a surface hexagon, it is attached by ~ 0.63 eV, i.e., by a bonding energy practically identical to that of ~ 0.61 eV with which a single H_2O molecule is retained on the ice. When on top of a surface oxygen, the adsorption energy decreases to ~ 0.5 eV. The position on top of an OH dangling bond, which is the last that can possibly be occupied in the Na escape process, is stabilized by only ~ 0.1 eV. This evolution corresponds to an increase of the distance of Na to the mean surface plane from 1.90 to 4.31 Å. The ionicity of Na falls to +0.11 electron, which means that the sodium atom has recovered $\sim 91\%$ of its 11 electrons in the last step before desorption as a neutral species.

5. DISCUSSION

The aforementioned developments allowed us to propose the following scenario: Na has been essentially trapped in rocks during their condensation in the protosolar nebula. Comets (or their parent bodies), which are made from a mixture of ices and rocks, underwent some thermal heating due to radiogenic decay at early epochs after their formation. This enabled the formation of liquid water in the nuclei, washing the Na^+ ions out of the refractory material. The fraction of sodium transferred from rocks to liquid water has been investigated in a few geophysical studies. Equilibrium calculations performed by Zhanshi (2001) at 120 °C, namely, the lowest temperature we found in the literature so far, show that the mole fraction of Na^+ in liquid water increases from $\sim 10^{-3}$ to 10^{-2} with the water-to-rock ratio decreasing from 10^6 to 10 . Though studies performed in the 0 °C–100 °C range would be more compatible with our nucleus model, extrapolating to an ice-to-rock ratio of 1 as in our model (see Section 2), we find that $\text{Na}^+/\text{H}_2\text{O}$ mole fractions higher than 10^{-2} are plausible in the liquid phase of the nucleus. Once transferred to liquid water, the ionized sodium atoms acquired electrons from the forming ice. In this process, sodium atoms cannot remain in a vacuum within the crystal cells that are not in a stable position and migrate either to take the place of an H_2O molecule or diffuse to the surface. As the layers of ice vaporize, Na lies closer to the surface finally becoming an adsorbed atom and

acquiring a quasi-neutral structure in that position. In conclusion, it is a neutral Na that is ejected from the surface layers with H₂O.

Our scenario is consistent with the fact that Na can also be derived from refractory dust. In fact, two Na reservoirs should coexist in a comet. The *Rosetta* spacecraft should have the ability to verify our scenario. Two mass spectrometers, namely, Cometary Secondary Ion Mass Analyser (COSIMA; Le Roy et al. 2012) and Rosetta Orbiter Spectrometer for Ion and Neutral Analysis (ROSINA; Balsiger et al. 2007), are on board the *Rosetta* spacecraft and should investigate the composition of the material expelled from the nucleus of 67P/Churyumov–Gerasimenko from 2014 August to the end of 2015. COSIMA and ROSINA are dedicated to the analysis of dust ejected from the nucleus and the determination of the comet’s atmosphere/ionosphere compositions, respectively. The COSIMA detection of Na in dust would in principle support the likely existence of its refractory reservoir, unless this atom has been adsorbed on grains when volatiles were expelled throughout the crust. On the other hand, the ROSINA detection of Na in the coma and the highlighting of a correlation between its production rate and the one of H₂O during the *Rosetta* flyby would validate (1) the existence of a volatile reservoir and (2) the fact that 67P/Churyumov–Gerasimenko or its parent body underwent some aqueous alteration in the past.

O.M. acknowledges support from CNES. This work has been carried out thanks to the support of the A*MIDEX project (No. ANR-11-IDEX-0001-02) funded by “Investissements d’Avenir” French Government programs, managed by the French National Research Agency (ANR). A.G.-L. acknowledges support from the European Space Agency Fellowship program. This research was also supported by CNRS program PCMI (Physique et Chimie du Milieu Interstellaire) and a PhD grant from MICHEM Labex to M.D.

REFERENCES

- Asplund, M., Grevesse, N., Sauval, A. J., & Scott, P. 2009, *ARA&A*, **47**, 481
 Balsiger, H., Altwegg, K., Bochsler, P., et al. 2007, *SSRv*, **128**, 745
 Bredichin, T. 1882, *AN*, **102**, 207
 Brownlee, D. 2014, *AREPS*, **42**, 179
 Calatayud, M., Courmier, D., & Minot, C. 2003, *CPL*, **369**, 287
 Casassa, S., Calatayud, M., Doll, K., Minot, C., & Pisani, C. 2005, *CPL*, **409**, 110
 Casassa, S., & Pisani, C. 2002, *JChPh*, **116**, 9856
 Cochran, A. L., Wooden, D. H., McKay, A. J., et al. 2013, AAS/Division for Planetary Sciences Meeting Abstracts, **45**, #502.05
 Cremonese, G., Boehnhardt, H., Crovisier, J., et al. 1997, *ApJL*, **490**, L199
 Cremonese, G., Huebner, W. F., Rauer, H. J., & Boice, D. C. 2002, *AdSpR*, **29**, 1187
 Ferro, Y., & Allouche, A. 2003, *JChPh*, **118**, 10461
 Furusho, R., Kawakita, H., Fujii, M., & Watanabe, J.-I. 2005, *ApJ*, **618**, 543
 Glassgold, A. E., Feigelson, E. D., & Montmerle, T. 2000, in *Protostars and Planets IV*, ed. V. Mannings, A. P. Boss, & S. S. Russell (Tuscon, AZ: Univ. of Arizona Press), 429
 Grimme, S. 2004, *JCoCh*, **25**, 1463
 Grimme, S. 2006, *JCoCh*, **27**, 1787
 Grimme, S., Antony, J., Ehrlich, S., & Krieg, H. 2010, *JChPh*, **132**, 154104
 Guilbert-Lepoutre, A., Lasue, J., Federico, C., et al. 2011, *A&A*, **529**, A71
 Haruyama, J., Yamamoto, T., Mizutani, H., & Greenberg, J. M. 1993, *JGR*, **98**, 15079
 Huebner, W. F., Benkhoff, J., Capria, M.-T., et al. 2006, in *Heat and Gas Diffusion in Comet Nuclei*, ed. W. F. Huebner et al. (Noordwijk: ESA Publications Division), 31
 Irvine, W. M., Leschine, S. B., & Schloerb, F. P. 1980, *Natur*, **283**, 748
 Jacobsen, B., Yin, Q.-Z., Moynier, F., et al. 2008, *E&PSL*, **272**, 353
 Johansen, A., & Klahr, H. 2011, *EM&P*, **108**, 39
 Johansen, A., Oishi, J. S., Mac Low, M.-M., et al. 2007, *Natur*, **448**, 1022
 Kozłowski, D., & Pilmé, J. 2011, *JCoCh*, **32**, 3207
 Kresse, G., & Hafner, J. 1994a, *PhRvB*, **49**, 14251
 Kresse, G., & Hafner, J. 1994b, *JPCM*, **6**, 8245
 Kunihiro, T., Rubin, A. E., McKeegan, K. D., & Wasson, J. T. 2004, *GeCoA*, **68**, 2947
 Le Roy, L., Briani, G., Briois, C., et al. 2012, *P&SS*, **65**, 83
 Lattalais, M., Bertin, M., Mokrane, H., et al. 2011, *A&A*, **532**, A12
 Leblanc, F., Fulle, M., López Ariste, A., et al. 2008, *A&A*, **482**, 293
 Lemon, H. B., & Bobrovnikoff, N. T. 1926, *Natur*, **117**, 623
 Levin, B. J. 1964, *Icar*, **3**, 497
 Liu, M.-C., McKeegan, K. D., Goswami, J. N., et al. 2009, *GeCoA*, **73**, 5051
 Llusar, R., Beltran, A., Andrès, J., & Silvi, B. 1999, *JCoCh*, **20**, 1517
 MacPherson, G. J., Davis, A. M., & Zinner, E. K. 1995, *Metic*, **30**, 365
 Makide, K., Nagashima, K., Krot, A. N., et al. 2011, *ApJ*, **733**, L31
 Makide, K., Nagashima, K., Krot, A. N., et al. 2013, *GeCoA*, **110**, 190
 Mercuri, F., Mundy, C. J., & Parrinello, M. 2001, *JPCA*, **105**, 8423
 Merk, R., & Prialnik, D. 2006, *Icar*, **183**, 283
 Mundy, C. J., Hutter, J., & Parrinello, M. 2000, *JChS*, **122**, 4837
 Oppenheimer, M. 1980, *ApJ*, **240**, 923
 Perdew, J. P., Chevary, J. A., Vosko, S. H., et al. 1992, *PhRvB*, **46**, 6671
 Prialnik, D., Bar-Nun, A., & Podolak, M. 1987, *ApJ*, **319**, 993
 Prialnik, D., & Podolak, M. 1995, *Icar*, **117**, 420
 Silvi, B., & Savin, A. 1994, *Natur*, **371**, 683
 Wallis, M. K. 1980, *Natur*, **284**, 431
 Watanabe, J.-I., Kawakita, H., Furusho, R., & Fujii, M. 2003, *ApJL*, **585**, L159
 White, W. B., Johnson, S. M., & Dantzig, G. B. 1958, *JChPh*, **28**, 751
 Zhanshi, Z. 2001, *Geothermal Training in Iceland*, Vol. 17 (Reykjavik: Reykjavik University), 405
 Zolensky, M. E., Bodnar, R. J., Gibson, E. K., Jr., et al. 1999, *Sci*, **285**, 1377

6.3 Conclusion

The all-chemical scenario proposed here has been discussed, opening the possibility of a second reservoir for Na atoms, independently of the first one considered till now, i.e. the refractory dust assumed to be present in the ice. The existence of this second reservoir depends strongly of the thermal history of the comet. Consequently, if our scenario is valid and if Na originating from water ice is detected, then we face there a testimonial of the past aqueous alteration of the comet or its parent body. This point is certainly the most important consequence of such a scenario for the understanding of the formation and evolution of the bodies of the primitive nebula.

A very close scenario could be eventually applied to other bodies of our solar system. For example, sodium and potassium have been detected in the exosphere of Europe, satellite of Jupiter, which is assumed to hide an internal ocean under an icy crust of several tenths of kilometers [3]. Those two volatile elements could originate in the icy mantle of Europe and not, as previously proposed, in the strong volcanism of its neighbor Io [4–7]. Considering that, at an early stage of its history, Europe had a global ocean with direct contact on its rocky kernel, a situation which allowed the transfer of sodium and potassium ions to water and then to ices when Europe began to freeze. Later on, convection movements [8] could have brought to the surface the elements trapped in the ices and ejected them by some sputtering mechanism, explaining thereby their current observation in the atmosphere of Europe. Calculations analogous to those realized for the case of Na and comets, have to be performed in order to assert such an hypothesis.

References

- [1] Th. Bredichin. “Sur la queue du I. type de la comète de 1882 II.” en. In: *Astronomische Nachrichten* 106.12 (1884), pp. 177–180.
- [2] Y. Ellinger et al. “Neutral Na in Cometary Tails as a Remnant of Early Aqueous Alteration”. en. In: *The Astrophysical Journal Letters* 801.2 (Mar. 2015), p. L30.
- [3] Kevin P. Hand et al. “Clathrate Hydrates of Oxidants in the Ice Shell of Europa”. In: *Astrobiology* 6.3 (2006), pp. 463–482.
- [4] F. Cipriani et al. “Sodium recycling at Europa: what do we learn from the sodium cloud variability?” en. In: *Geophysical Research Letters* 35.19 (2008), p. L19201.
- [5] F. Leblanc, R. E. Johnson, and M. E. Brown. “Europa’s Sodium Atmosphere: An Ocean Source?” In: *Icarus* 159.1 (2002), pp. 132–144.
- [6] F. Leblanc et al. “Origins of Europa Na cloud and torus”. In: *Icarus. Jovian Magnetospheric Environment Science* 178.2 (2005), pp. 367–385.
- [7] R. E. Johnson et al. “Energy Distributions for Desorption of Sodium and Potassium from Ice: The Na/K Ratio at Europa”. In: *Icarus* 156.1 (2002), pp. 136–142.
- [8] R. T. Pappalardo et al. “Geological evidence for solid-state convection in Europa’s ice shell”. en. In: *Nature* 391.6665 (1998), pp. 365–368.

Chapter 7

Conclusion and Perspectives

One of the main aims of this thesis was to propose and use an original strategy to determine the adsorption energies through a joint theoretical-experimental approach. The adsorption energy is an intrinsic parameter that measures the strength of interactions between an adsorbate and a surface. Because it represents the energy to overcome for an adsorbed species to be liberated into gas phase, it is at the cornerstone of the quantification of any solid-to-gas exchange process. In the astrophysical context it takes a special importance since constant exchange between the gas phase and interstellar dust grain surfaces (bare or covered with water-rich ices) is expected to occur, impacting strongly the gaseous molecules abundance ratios detected via radio-astronomy.

A better understanding of the origin of these molecules has motivated the development of astrochemical codes of increasing complexity, which take into account solid-state and gas phase chemical networks and the adsorption-desorption processes. As a consequence, these codes require an increasing amount of quantitative and relevant data, including the adsorption energies, for a collection of molecules and substrates. Determining such data reliably and quickly is a challenge this thesis takes up.

In this work, experimental determination of adsorption energies at low surface coverage (less than a monolayer) is performed by means of the Temperature Programmed Desorption (TPD) method. The technique itself is in principle relatively easy, but it implies a very good control of the experimental conditions which are in practice difficult to achieve. Among them: the very low pressure (ultrahigh vacuum (UHV) conditions), the cryogenic temperature ($T \sim 10-100$ K), the absolute temperature measurement, its stability and control with a linear heating rate, the quantification of the condensed molecules in term of monolayers and the reproducibility of the deposition method, the linearity of the detector and evaluation of the signal pollution by desorption from cold parts of the setup other than the sample surface. During this thesis, a large part of the experimental work was dedicated to a re-optimization of the already existing UHV setup SPICES to fulfil all of these conditions. A special effort was made on:

- hardware development and optimization for the control and stability of the sample temperature,
- development of the ice deposition protocol providing the deposited ice thickness (multilayer) or the surface coverage fraction (sub-monolayer) reproducibility of the order of a few percent,

- method of absolute surface coverage calibration by tracking the change of desorption kinetics order,
- evaluation of the parasite desorption signal from cold parts of the cryostat by a systematic 'witness' monitoring of the desorption with the sample surface facing the opposite direction of the detector.

It has to be emphasized that a new acquisition software was developed during the thesis, which allows for controlling, at the same time, the mass spectrometer, temperature and pressure reading and the sample heating system. This new software represents a significant improvement for time gain, precision and reproducibility in the conduction of desorption experiments.

The extraction of adsorption energies from TPD experiments is also an issue that was addressed during this work. In particular, the desorption process depends on three unknown parameters that are: adsorption energy, kinetic order and a pre-exponential factor. Many different methods can be found in the literature to evaluate these parameters. Some researchers set them as free parameters in the desorption curve fitting, and some other use arbitrary values of the pre-factor, which in the end makes difficult the inter-comparison of adsorption energies obtained by different groups. Since many couples (adsorption energy / pre-factor) can result in appropriate experimental curve fitting, we have developed a method which allows quasi-independent determination of these two quantities. Our method, that relies on a first order kinetic approximation for submonolayer desorption and on an adsorption energy distribution taking into account different adsorption sites and geometries, has been used for all the presented systems. It has been benchmarked with the already known case of methanol adsorption on graphite, and it has proven to be efficient in extracting dependable adsorption energy values from a limited set of desorption curves, together with bringing hints on adsorption parameters and quality of the substrates.

The computational chemistry strategy to determine the adsorption energies is based on quantum chemistry calculations using periodic density functional theory (DFT) approach. The interactions between physisorbed atoms or molecules and the surface, though weak, can be computed with DFT by using a correction – namely the Grimme correction – to take into account the dispersion forces. The main challenge to overcome for a proper evaluation of the adsorption comes from the size of the system to get an accurate description of the surface. Using an approach where the solid is modelled as a cluster of finite number of atoms would require dealing with very big systems, for which both the computing time and the convergence of the calculation represent important issues. Instead, the choice that has been made is to model the surface using a periodic system, in which a finite unit cell, including the crystalline structure of the surface and bulk, the above-standing vacuum and the adsorbate, is periodically translated along the three axis. Once the different parameters determining the unit cell (dimension of the plane cell, the slab thickness and the vacuum) have been optimized, it allows for easily modelling an infinite solid-vacuum interface. Geometries of the adsorbate positioned on the surface, together with the topmost layers of the surface, are optimized in order to reach the real minimum of the interaction potential well, and thus the adsorption energies. Using this powerful method, several adsorption sites, each associated with its own adsorption energy, can be distinguished on the surface models.

For each of them, not only the value of the adsorption energy, but the adsorption geometry can be accessed, which gives a valuable information on the parameters that drive the adsorption strength (role, number and nature of hydrogen bonds, involved chemical functions of the molecule, involved surface sites and role of defects).

These two methods, experimental and theoretical, were used in parallel for all the systems that are presented in this thesis. The strength of this dual approach comes from the systematic comparison between the experimental values and the calculations outputs. Indeed, the two methods are complementary on many aspects. The experiments bring adsorption energies together with another parameter, the pre-exponential factor, which is also of importance for quantifying desorption flux from a surface at a given temperature. In addition, the experimental approach enables to study desorption from amorphous substrates, such as compact amorphous water ices, for which a proper periodic theoretical description is difficult because of the lack of long-range ordering in physical system. However, the experiments can only access the average values over a large amount of different adsorption sites and geometries. It is impossible to probe them separately. Finally, lateral interactions between adsorbates and the presence of defects on the substrates cannot be avoided in experiments, and begin to play an important role when low coverage of adsorbates is considered. In the contrary, the computational approach brings a detailed description of the adsorption, separating different adsorption sites, providing geometries, and highlighting the weight of the chemical function in the adsorption energies. Lateral interactions between adsorbates can be evaluated by varying the size of the unit cell in the periodic description, and model defects can be generated in the surfaces to explain singular behaviour observed experimentally. Finally, theory can give the access to the adsorption energies of molecules adsorbed on water surfaces, where adsorption energies are larger than the water ice cohesive energy, and thus unreachable experimentally by desorption methods.

The first case that has been studied concerns the adsorption of noble gas atoms on the water ice. This study has been realized in the context of the abnormal and still unexplained under-abundance of noble gas in the gaseous giant planets and their satellites as compared to solar system abundances. Among the different hypotheses proposed, the question of the efficiency of trapping these atoms at the surface or inside the water-rich icy mantles of grains during the early stages of planets formation has to be considered. For this purpose, argon, krypton and xenon adsorption and trapping on water ices have been experimentally and theoretically addressed. TPD experiments have been realized on crystalline and compact amorphous water ices. For the three atoms, no clear difference in adsorption energies were identified between the two allotropic forms of the ice, beside a very weak high temperature desorption feature associated to a diffusion in the subsurface of amorphous water ice. Mean adsorption energies of 75 ± 10 meV, 130 ± 20 meV and 170 ± 20 meV have been derived for Ar, Kr and Xe adsorption on crystalline water ice respectively. DFT calculations have evidenced the existence of various preferential adsorption sites of rare gas atoms on crystalline water ice, which are identical for Ar, Kr and Xe despite their important size difference. The corresponding computed adsorption energies vary between 66 and 120 meV for Ar, 100 and 150 meV for Kr and 100 and 190 meV for Xe, in general good agreement with what has been experimentally found. The trapping of the noble gas atoms in the ice matrix has also been evaluated experimentally and theoretically. Theoretically,

rare gas atoms were inserted in the water ice subsurface by both, substitution and intercalation. In both cases, after relaxation of the system, the insertion of the atoms has revealed to be energetically unfavourable by several hundreds of meV. However, if the defect in the water ice bulk is sufficiently big (several molecules missing), the Ar can be stabilized and trapped into the water matrix. This opens the way to a very interesting possibilities of trapping rare gas atoms into icy bulk. To support this, experimental studies need to be performed in detail on the trapping efficiency of the water ice. Very preliminary experiments have been realized during this thesis, that tend to show that amorphous water ice can retain efficiently rare gas atoms inside the bulk up to the ice desorption temperatures. If this is confirmed, then the trapping of Ar into “holes” defects of the water ice could be an alternative to the trapping of rare gas by clathrate-like structures, whose presence in the interstellar medium is still under debate.

The second case presented in this work deals with the adsorption of two isomers, acetonitrile CH_3CN and methyl isocyanide CH_3NC , which has been investigated for different astrophysically-relevant surfaces. Adsorption on graphite and quartz has been studied to mimic the adsorption of these species onto the surface of bare interstellar dust grains, while water ice surfaces have been considered to represent the adsorption on the icy mantles of the grains. The acetonitrile and isoacetonitrile are commonly detected in many regions of the interstellar medium. On the contrary of the simplest nitrile and isonitrile HCN and HNC, the abundance ratio of $\text{CH}_3\text{CN}/\text{CH}_3\text{NC}$ is observed to be about about 50 independently of the detection region. If the adsorption/desorption from grains plays an important role in their gas phase abundances, then differential desorption should be equivalent for the two isomers in these different regions, and therefore the same behaviour is expected to be observed in the case of different grain surfaces, bare or recovered with ice. In this thesis, we have measured, using our experimental-theoretical approach, the adsorption energies of acetonitrile and isoacetonitrile on quartz- $\alpha(0001)$, graphite and water ice surfaces. The case of adsorption on the graphite surface leads to different results: theoretical values on perfect graphene planes were found systematically weaker than the experimental values. This can be understood by the preponderant role of the defects of the experimental graphite surface, whose stabilization power on the adsorbate has been evidenced theoretically by model defects. For the adsorption on water ices and quartz surfaces, both theoretical and experimental approaches lead to very similar values for the adsorption energies. The studies show a tighter bonding of the acetonitrile isomer as compared to the isoacetonitrile, that we associate with a stronger ability of the CH_3CN molecule to be involved in hydrogen bonding with the surface OH groups. In general, for each surface (bare grain equivalent or ice mantle), CH_3CN is more bonded to the substrate than CH_3NC , which is consistent with a differential desorption process that we expect equivalent in different regions of the ISM.

The third case has been treated only within the computational approach. Concerning an unusual aspect of the composition of the coma of some comets (presence of a only neutral sodium coma), this subject, motivated by the data abundance to come with the Rosetta mission, required to study the behaviour of sodium atoms, in particular from the point of view of the charge, all along their journey through the cometary ices to the surface. This implies to model not only adsorbed species on ices

but also inserted species into the ices. From the calculations giving the interaction Na-ice and the charge of Na as a function of the position into the ice (diminishing from 0.9 in the core to 0.1 at the surface), the presence of an additional (and may be major) reservoir of neutral sodium has been deduced. Two interesting consequences are following: first, such an origin of the neutral Na tail observed in some comets could be seen as a proof for an early aqueous alteration phase of this kind of comets; second, this scenario and the computational treatment used here could be applied to other icy planets (or satellites) atmospheres, for example Europe, to elucidate some unusual characteristic observed but unexplained.

As we see all along this thesis and the examples quoted, the strategy which consists in combining two methods issued from totally different backgrounds, is efficient and general. Its application to systems of very different sizes with equivalent precision proves its versatility. The coincidence of the values obtained through the two channels helps to be confident of the reliability of the numbers and therefore of the interpretation of the phenomena considered. Many more astrophysical molecules (or atoms) should be studied in the months to come, in particular larger species of astrobiological interest which are expected to form preferentially on the grains surfaces and for which the data constituted by the energy adsorptions are of utmost importance to model formation and survival. All these data, crucial for astrochemical models, are to be collected in databases as KIDA (Kinetic Database for Astrochemistry), in order to be incorporated systematically in the astrochemical reactivity codes taking care of the gas-solid exchanges. It is obvious that the pressure for such data is currently very strong and that too many couples molecule-surface have to be treated in a too short amount of time; a wise and promising solution would be to use this dual strategy whose experimental versus computational confrontation asserts confidence in its reliability, to get quick predictive insight in the future. A systematic study of the main chemical functions (ketone, nitrile, ester), and of the carbon-chain size, is currently under progress.

Appendices

Appendix A

PID zones table

PID parameter values as a function of sample holder temperature, calibrated for SPICES cryostat assembly:

T (K)	P	I	D
0..20	500	200	100
20..30	450	175	100
30..35	400	140	100
35..40	200	120	100
40..45	130	90	100
45..50	110	75	100
50..60	90	60	100
60..80	70	45	100
80..110	50	35	100
110..400	45	30	100

Appendix B

TPD model function

```

1  function [p,theta]=modelTPDmc(T,fitpar)
2  %function [p,theta]=modelTPDmc(T,fitpar)
3  %Model first order TPD curve as a sum of sites
4  % with coverages fitpar.thetas,
5  %fitpar should have following attributes:
6  %energies Ei=E0+i*dE,
7  %prefactor v,
8  %heating rate rate
9  %ml monolayer integral
10
11  % Returns:
12  % p - desorption rates array
13  % theta - coverages array
14
15  E0=fitpar.E0;
16  dE=fitpar.dE;
17  v=fitpar.v;
18  rate=fitpar.rate;
19  scale=fitpar.scale;
20  monolay=fitpar.ml;
21  thetas=fitpar.thetas;
22
23  k = 1.38e-23*6.24e18; % (J K^-1)*(eV/J) = eV K^-1 = 8.6e-5 eV K^-1
24
25  numpts=length(thetas);
26  E=linspace(E0,E0+dE*(numpts-1),numpts);
27  #Pre-calculate parameters
28  odepar.ek1=E/k; odepar.nuoa=v/rate;
29
30  if (rows(thetas)!=rows(T))
31      thetas=thetas';
32  endif;
33
34  of=@(x,t) odemlde(x,t,odepar); #Solve the ODE
35  theta=lsode(of,thetas,T);
36
37  #Derive desorption rates from coverage values
38  numT=length(T);
39  p=zeros(numT,1);
40  for i=1:numT
41      %For each temperature point find desorption flow
42      % as a sum of flows defined by remaining coverages
43      p(i)=(-sum(odemlde(theta(i,:),T(i),odepar)));

```

```
44  endfor
45
46  %Switch from 1/K to 1/sec.
47  p=p*rate*monolay*scale;
48
49  endfunction;
50
51  %ODE for zero and first order desorption
52  function dthetadT = odemlde(thetas,T,param)
53      nuovera=param.nuoa;
54      Eoverk=param.ek1;
55      dthetadT = (thetas>eps)'.*(-nuovera).*min(thetas,1)'.*exp(-Eoverk./(T+eps));
56  endfunction;
```

Appendix C

VASP parameters

In the following table, VASP calculation parameters explicitly specified in the INCAR file are indicated.

Option	Value	Description
GGA	PE	Perdew-Burke-Ernzerhof GGA functional
LCHARG	.FALSE.	Omit saving the charge density to conserve disk space and reduce memory consumption.
LELF	.TRUE.	Set to true to produce the ELF output file.
NSW	1; 600	Maximum number of geometry optimization steps. Set to 1 to disable the geometry optimization.
ISIF	2	Calculate forces, stress tensor and relax ions. Use 3 or 6 for the cell geometry optimization. Refer to VASP documentation for more details.
IBRION	2	Relax ions to the ground state using a conjugate-gradient algorithm.
VOSKOWN	1	Use the Vosko-Wilk-Nusair interpolation for the correlation part of the exchange correlation functional. Recommended for GGA functionals.
LDIPOL	.FALSE.	Do not use dipole correction.
NPAR	4	The number of bands that are treated in parallel, determines the parallelization efficiency. Set to approx. square of the number of CPU cores used.
PREC	Accurate	Perform high-precision calculation to obtain correct energies.
ENCUT	400	Explicitly set the maximum plane wave energy cut-off to 400 eV.
LREAL	A	Use real-space projection for non-local part of the pseudopotentials. Recommended for big systems with more than 20 atoms.
LVDW	.TRUE.	Enable the DFT-D2 dispersion correction by Grimme.
EDIFFG	-0.015	Minimum force per atom criteria to interrupt the geometry optimization loop. $0.015\text{eV}\text{\AA}^{-1}$ is a reasonable value.

Table .1 – VASP INCAR parameters used in this work to perform calculations.

Acronyms

- ASE** Atomic Simulation Environment. 53
- DFT** Density Functional Theory. 6, 49–51
- DSD** doser-surface distance. 28
- ELF** Electron Localization Function. 63
- FTIR** Fourier-Transform Infrared. 16
- GGA** Generalized Gradient Approximation. 51, 52
- HOPG** highly-oriented pyrolithic graphite. 16, 40, 45
- ISM** interstellar medium. 7, 8, 15, 99
- LDA** Local Density Approximation. 51
- MCT** Mercury Cadmium Telluride. 16
- MEP** Minimum Energy Principle. 99
- OFHC** oxygen-free high thermal conductivity. 17, 20
- PAH** Polycyclic Aromatic Hydrocarbons. 52
- PID** Proportional-Integral-Derivative. 19, 20
- QMS** quadrupole mass spectrometer. i, 16, 21, 24, 28, 31, 32, 35
- RAIRS** Reflection-Absorption Infrared Spectroscopy. 74
- RGAs** residual gas analysis. 25
- SEM** secondary electron multiplier. 23, 24, 31
- TPD** Temperature Programmed Desorption. 15, 32, 78, 94, 131

UHV ultrahigh vacuum. 15, 26, 131

VASP Vienna Ab initio Simulation Package. 6, 52

VSEPR Valence shell electron pair repulsion. 63, 64

Sujet : Adsorption on Interstellar Analog Surfaces: from Atoms to Organic Molecules

Résumé : Les interactions gaz-grains jouent un rôle important dans la chimie des milieux interstellaires et protoplanétaires. Le paramètre-clé qui gouverne les échanges entre la surface des grains et la phase gazeuse est l'énergie d'adsorption E_a . Ce travail a pour but de développer une approche jointe expérimentale et théorique afin de déterminer les énergies d'adsorption pour des atomes et molécules d'intérêt astrophysique sur des substrats-modèles des surfaces des grains de poussière interstellaires.

Expérimentalement, la méthode employée est la désorption programmée en température (TPD). Le travail a contribué en l'établissement d'une méthode de traitement des courbes de désorption, basée sur une distribution d'énergie d'adsorption et utilisant un set limité de données à plusieurs rampes de chauffage, pour déterminer le couple de paramètres de l'équation de Polanyi-Wigner que sont l'énergie d'adsorption et le préfacteur.

D'un point de vue de la chimie théorique, les énergies d'adsorption sont déterminées en utilisant la théorie de la fonctionnelle de la densité (DFT) implémentée dans le module "Vienna Ab initio Simulation Package" (VASP). Cette méthode permet également d'accéder aux géométries d'adsorption, ainsi qu'aux différents sites sur la surface.

La méthode expérimentale a été validée par une comparaison avec un système connu : l'adsorption du méthanol CH_3OH sur le graphite. L'adsorption des gaz rares Ar/Kr/Xe sur les glaces d'eau a été étudiée comme un cas d'intérêt pour la planétologie. L'adsorption de l'acétonitrile (CH_3CN) et de son isomère l'isoacétonitrile (CH_3NC) sur les surfaces de graphite, de quartz et de glaces d'eau a également été étudiée, puisque ces deux molécules sont détectées dans le milieu interstellaire. Les énergies d'adsorption trouvées dans le cadre de ce travail seront intégrées dans la base des données KIDA.

Mots clés : Désorption Adsorption DFT

Subject : Adsorption on Interstellar Analog Surfaces: from Atoms to Organic Molecules

Résumé : Gas-grain interaction plays an important role in the chemistry of the cold interstellar medium and protoplanetary disks. A key parameter for modeling the exchange between grain surfaces and gas phase is adsorption energy, E_a . This work aims to develop a reliable and systematic experimental/theoretical approach to determine the adsorption energies of relevant atoms and molecules on models of interstellar grain surfaces.

Employed experimental technique is the Temperature Programmed Desorption. Developed experimental protocol and data treatment technique based on distribution of adsorption energies and use of a set of heating rates enable to determine the coupled parameters of Polanyi-Wigner equation: adsorption energy E_a and prefactor ν .

Computational chemistry approach, Density Functional Theory (DFT) as implemented in Vienna Ab initio Simulation Package (VASP) is used to get the insight on the behaviour of the surface-adsorbate systems at the atomic level. This approach allows as well to determine adsorption energies. A presence of multiple adsorption sites with different adsorption energies is predicted.

Methanol (CH_3OH) adsorption on graphite is used as a known example to validate the technique. Ar/Kr/Xe adsorption on water ice is studied as a case relevant for planetology. Acetonitrile (CH_3CN) and methyl isocyanide (CH_3NC) adsorption on water ice, quartz and graphite is investigated since those two molecules are both detected in the interstellar medium.

Adsorption energies determined in this work will be included in KIDA database.

Keywords : TPD, DFT, Adsorption